Université Lille I - Sciences et Technologies
Laboratoire de Mécanique de Lille (UMR CNRS 8107)
Ecole Doctorale SPI Lille Nord-de-France
Année 2013 - N° d'ordre : 41172

THESE

Pour obtenir le grade de
Docteur de l'Université Lille I - Sciences et Technologies
Discipline : Génie Civil
Présentée par
Chi YAO

Modélisation numérique du couplage hydromécanique dans le massif rocheux fracturé

Soutenue publiquement le 15 juillet 2013 devant le jury composé de
M. D HOXHA, Professeur, Université d'Orléans, Rapporteur
M. H ZHOU, Professeur, IRSM, Académie des Sciences de Chine, Rapporteur
M. JB COLLIAT, Professeur, Université Lille I, Membre
M. F DUFOUR, Professeur, INP Grenoble, Membre
M. QZ ZHU, Maître de conférences, Université Paris Est , Membre
M. JF SHAO, Professeur, Université Lille I, Directeur de these

Résumé

L'étude des effets du couplage hydromécanique est primordiale dans de nombreux projets d'ingénierie de mécanique des roches, tels que le stockage géologique des déchets radioactifs, la construction de grandes pentes élevées et des cavités souterraines pour centrales hydroélectriques. En raison de la présence de multiples surfaces de discontinuité, les propriétés hydrauliques et mécaniques des massifs rocheux sont difficiles à caractériser. Des expériences sur le site sont soit coûteuses, soit impossibles; les expériences en laboratoires sont limités tant pour le chemin de chargement appliqué que pour la taille des échantillons testés. La modélisation numérique fournit une voie intéressante et complémentaire aux expériences en laboratoire et in situ pour la caractérisation des comportements hydromécaniques des massifs rocheux.

Dans cette thèse, nous proposons une modélisation unifiée du couplage hydromécanique des massifs rocheux fracturés en se basant sur la caractérisation de réseaux de fractures discrètes (DFN). En particulier, nous proposons une extension de la méthode dite de ressorts de corps rigides (RBSM). Les principales contributions de ce travail portent sur les points suivants:

(1) Un modèle de comportement mésoscopique, basé sur la méthode RBSM, est développé pour décrire la fissuration de la roche. Ce modèle permet de prendre en compte la distribution de fractures préexistantes, l'initiation, la propagation et la coalescence de nouvelles fissures. La roche intacte est représentée par un certain nombre de blocs rigides, répartis aléatoirement et reliés par des ressorts. La déformation macroscopique du massif est due à la déformation locale des interfaces entre blocs.

(2) Nous avons ensuite proposé un modèle à double porosité pour modéliser le transfert hydraulique dans le massif à partir de la distribution de fractures discrètes. En combinaison avec le modèle RBSM, la variation de la perméabilité lors de la fissuration du massif est étudiée.

(3) La formulation d'inégalité variationnelle pour le problème d'écoulement avec surface libre est étendue aux réseaux de fractures en 2D et 3D. Cette formulation permet d'aborder les problèmes de surfaces libres dans les massifs fracturés même des topologies et des frontières complexes.

(4) Le comportement hydromécanique des massifs avec une grande densité de fracyures est étudié. Un modèle de comportement est proposé pour décrire les relations non linéaires entre la contrainte normale et la déformation normale, entre le glissement tangentiel et la dilatation normale. Les réponses hydromécaniques sous de différentes conditions de chargement sont étudiées..

Mots clés: Massif rocheux, couplage hydromecanique, fracture, rupture, permeabilite, RBSM, transfert

Numerical modeling of hydromechanical coupling in fractured rock mass

Abstract

The characterization of hydromechanical coupling effects is very important in many rock engineering problems, such as geological repository of nuclear wastes, construction of high and steep rock slopes and underground hydropower houses. However, due to the presence of multiple discontinuities, it is generally difficult to characterize hydraulic and mechanical properties of rock masses. In situ experiments are generally expensive or sometimes impossible to realize. Laboratory investigations are limited to simple loading paths and small size samples. Numerical simulations provide an efficient and complementary way to the in-situ and laboratory investigations. In this thesis, we have proposed a unified approach, based on the improved rigid body spring method (RBSM), for modeling the hydromechanical coupling in both intact and fractured rocks. The main contributions of the thesis are summarized as follows.

(1) A mesoscopic model, based on the improved RBSM, is developed. This model is able to account for the initial distribution of preexisting fractures, the whole process of initiation, propagation and coalescence of new cracks. The intact rock is represented by a number of randomly distributed rigid blocks, connected by springs. The macroscopic deformation is due to the local deformation of interfaces between blocks.

(2) A dual porosity model for seepage flow in rock mass is proposed, based on the discrete fracture network model. Combined with the improved rigid body spring method, the permeability variation during rock fracturing is investigated.

(3) The Variational Inequality (VI) formulation for seepage problem with free surface is extended to fracture networks both in 2D and 3D conditions. This formulation is in particular suitable to solve free surface problems in fracture networks even with very complex topology and boundaries.

(4) For rock masses with high density of fractures, the deformability and conductivity of the intact rock matrix can be neglected. A non-linear constitutive model is introduced for fractures, taking into account the non-linear relationships between normal stress and deformation, between tangential shear slip and normal dilation. The governing mechanisms of hydromechanical coupling under different stress conditions are detected.

Key words: rock mass, hydro-mechanical coupling, fracture, failure, permeability, RBSM, transport

Acknowledgement

The study presented in this thesis has been carried out in the last five years since September, 2008 in the framework of scientific cooperation between Laboratoire de Mécanique de Lille and Wuhan University. During this period of time, a lot of people at the Key Laboratory of Rock Mechanics in Hydraulic Structural Engineering of Ministry of Education, Wuhan University and the ER 4 of the Laboratoire de Mécanique de Lille have contributed to this work with their kind assistance, advices and support. If you are among these people, please accept my sincere and utmost gratitude.

I would like to express my most sincere gratitude to my main supervisor, Professor Chuangbing Zhou at the School of Water Resources and Hydropower Engineering of Wuhan University, and Professor Jianfu Shao at Laboratoire de Mécanique de Lille, and to my secondary supervisor, Professor Qinghui Jiang at the School of Civil Engineering of Wuhan University, for their continuous support, patience, motivation and enthusiasm throughout the duration of my research.

China Scholarship Council is greatly acknowledged for providing me the living stipend in France and the round off air tickets from China to France.

I am deeply grateful to Professor Yifeng Chen, Dianqing Li and Associate Professor Guan Rong at the School of Water Resources and Hydropower Engineering of Wuhan University for their kind help and fruitful discussions with them. Professor Lanru Jing at the Royal Institute of Technology (KTH), in Sweden and Professor Huihai Liu at Lawrence Berkeley National Laboratory are also gratefully acknowledged for bringing me new insights during their visit to Wuhan University.

I consider it a great honor to work with my great colleagues during the last five years. They are doctor Wei Wei, doctor Qi Zufang, Mr Wang Xiaojiang, Mr Hu Ran, Mr Zhang Qin, Mr Tang Xiaosong, Mr Xiang Guangwen, Miss Xin Liping, Miss Liu Xianhua, Miss Lu Ruili, Mr Ye Zuyang, Mr Wang Bin, Mr Shang Kaiwei, Mr Qin Honghao, Miss Fu Mengmeng, Miss Chen Haixia, Miss Yang Rui, Miss Chen Na, Mr Xi Zhirui, Mr Liu Gang, Mr Xie Tao, Mr Hua Weibing, Mr Li Yao at Wuhan University, doctor Hu Dawei, doctor Wanqing Shen, doctor Yang He, doctor Jin Caifeng, Mr Li Mingyao, Mr Wu Qier, Mr Liu Zaobao, Mr Zhang Yu, Mr Zheng Lifeng at the Laboratoire de Mécanique de Lille. Doctor Zhang Zhenhua at University of Three Georges, doctor Xie Ni at China University of Geosciences, Wuhan, doctor Yun Jia at Lille 1, doctor Hanbing Bian at LML, are also gratefully acknowledged for their kind help during my study.

I wish to thank my parents. Without their support, love and trust the thesis would have not been possible. Last but not least, I am indebted to my beloved wife, Zhang Li. Without her, nothing of this work would make any sense.

Table of Content

List of Tables

List of Figures

Chapter 1 General Introduction

1.1 Background and Objective of the Thesis

Rock mass is a kind of composite material comprising of intact rock matrix and discontinuities. These discontinuities include fractures, fissures, joints, faults, bedding planes and other types of weak surfaces or interfaces. The combination of rock matrix and discontinuities has a significant effect on the characteristics of rock mass, such as strength, deformability, and permeability. Due to the presence of discontinuities, rock masses often exhibit highly anisotropic, inhomogeneous and multi scale behaviors [1].

Since it is inherently difficult to conduct full scale tests on rock masses, experiments in laboratories cannot thoroughly describe the complex behaviors of rock masses [2]. The estimation of properties of rock masses still much relies on empirical classification rules or systems based on practical experience and observations [2]-[6]. Though widely applied in practice, the rock mass classification systems remain limited in considering typical behaviors of rock mass such as strength anisotropy, scale effects and strain softening induced by pre-existing joint fabrics (i.e. joint orientation, joint density, and joint persistence). Furthermore, the complex topology and combination of constituents makes it very difficult even impossible to find a rigorous mathematical model for rock masses. Consequently, numerical simulation has become inevitable and plays an increasingly important role in the design and safety assessment of rock engineering projects.

To adequately capture the complex properties of fractured rock masses, a numerical method must have the capability to take into account the effects of joint fabrics, either explicitly or implicitly. And for a reliable solution, it is essential to consider coupling effects of thermal, hydraulic, mechanical and chemical processes (THMC) in many rock engineering projects, especially when influences on civil safety is concerned, such as in radioactive waste disposal projects [7]. For simplicity, only Hydro-Mechanical coupling (HM) instead of the whole coupling process of THMC is considered in this thesis.

HM coupling can be roughly grouped into two groups: direct coupling and indirect coupling[8]. The focus of this study is on indirect HM coupling, with special attention paid to the stress effects on the flow field and permeability, which is most relevant to fractured rock mass. The permeability of intact rock can increase by several orders of magnitude with the growth of micro cracks in preferential orientation under deviatoric stress. The flow in

pre-existing fractures is also influenced by stress since the fracture aperture is changeable under the effects of tension, compression and dilation.

The main aim of this thesis is to establish a unified numerical platform to simulate the hydro-mechanical coupling in rock masses, in which behaviors of both intact rock matrix and discontinuities are considered. In this platform, the presence of pre-existing discontinuities, and the whole process of crack initiation, propagation and coalescence are explicitly modeled.

1.2 Methodology

The modeling comprises of two physical processes: mechanical and hydraulic. The mechanical process is simulated by an improved rigid body spring method (RBSM) and the hydraulic process is simulated by the discrete fracture network model (DFN). Two different cases are considered separately: (1) coarsely fractured or intact rock: in the rock mass, there are only a few or no pre-existing discontinuities, and effects of the intact rock behavior such as damage and fracturing on HM coupling cannot be neglected; (2) densely fractured rock mass: in the rock mass, there exists many fractures intersecting with each other, and the hydro-mechanical behavior are mainly controlled by the assemblage of blocks and fracture networks. Illustration in Figure 1.1 are representations of these two kinds of rock masses. For the first case, the intact rock is represented by a mesh based on Voronoi Diagram, while for the second case the fractured rock is represented by an assemblage of blocks detected by the block search technique.

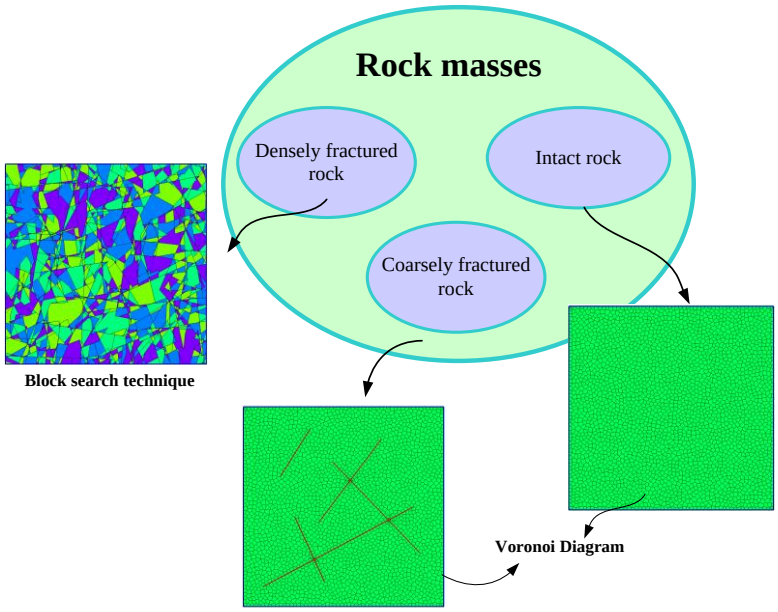

Figure 1.1 Representations of different kinds of rock masses

1.2.1 The Improved RBSM

The rigid body spring method is a limit analysis method first proposed by Kawai[9]. This method explicitly considers fractures and adopts an implicit solution procedure, enjoying both advantages of finite element method and discrete element method. Since fracturing process and weak discontinuities can be easily simulated, it has been extended to analyze stability problems encountered in the practice of engineering in such as rock slopes and deep excavations [10], [11], [12]. Afterwards, Bolander applied this method to study brittle fracture in homogeneous and isotropic materials [13], and Nagai used this method to simulate the failure process of mortar and concrete [14][15]. Afterwards, this method is used to simulate the behaviors of concrete under various conditions, such as chloride diffusion [16], frost damage [17] and high-stress creep and low-cycle fatigue loading [18]. The key idea of this method is that the rock material can be approximated by an assemblage of cemented polygonal blocks. The blocks are assumed rigid with similar size with a uniform yet random distribution. This assumption is reasonable since it is basically in line with experiment observations such as that shown in Figure 1.2 the micrograph of a Carrara marble reported by Pieri [19]. In both Bolander's and Nagai's work, uniformly distributed Voronoi diagram is employed as the basic mesh. The blocks interact with each other through their common interface such that deformation is represented by which of the block interface or by relative displacements between neighboring blocks. Inter-block forces are obtained in light of the relative displacements between blocks and the properties of interfaces. Tensile and shear cracks along interfaces take place once the tensile or shear strength of the interface is reached.

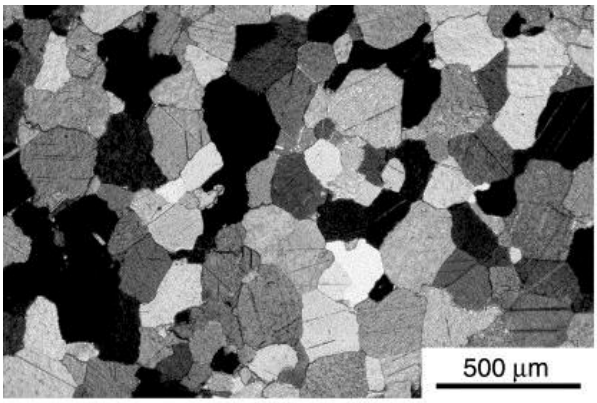

Figure 1.2 Micrographs of a Carrara marble (After Pieri[19])

In this study, the RBSM is improved to investigate the progressive failure of rock matrix and the deformation of fracture networks. For the former, the relationship between

macro and micro deformation parameters is established and a relatively simple fracturing criterion is proposed. For the latter, a constitutive model of fractures is introduced concerning nonlinear normal stress-deformation relationship, sliding and dilation effects.

1.2.2 The Discrete Fracture Network Model

The basic motivation for the use of the discrete fracture network lies in the fact that the flow of groundwater is mainly through a connected network of discrete fractures in many geological formations encountered in practice, such as the disposal of radioactive waste [20]. In the discrete fracture network model, a lot of flow and transport phenomena is quantified which cannot be properly captured by continuum models [21][22]. A major advantage of discrete fracture models is that it can explicitly consider the contribution of individual fractures to flow and transport. Permeability heterogeneity and spatial characteristics of fracture network is simulated directly in an easy manner. Consequently, discrete fracture models have favored popularity in both theoretical and practical studies, despite their computational limitations for large scale problems [23]-[33]. For 2D and 3D fracture networks, due to the demanding computational cost, it is generally assumed that a fracture is formed by a pair of smooth, parallel plates and the flow in fractures obeys the Cubic Law.

In this study, the discrete fracture network model is used in two different cases: (1) coarsely fractured or intact rock: the DFN model is extended to compute the conductivity of the dual system of rock matrix and fractures; (2) densely fractured rock mass: the DFN model is used to simulate hydro-mechanical coupling and free surface problems in fracture networks.

1.3 The main contents of the thesis

In this thesis, the improved rigid body spring method and discrete fracture network model are used to investigate hydro-mechanical coupling in both intact rock matrix and fracture network. In the first three chapters, i.e. chapter 1, 2 and 3, coupling in coarsely fractured and intact rock is considered. While in the rest of chapters, i.e. 4, 5 and 6, coupling in densely fractured rock masses is studied. The difference between these two kind of rock mass lies in whether or not to consider deformation and conductivity of intact rock. Some necessary modifications and improvements are made for different situations. The main contents of the thesis are organized into 6 chapters as shown in Figure 1.3 below.

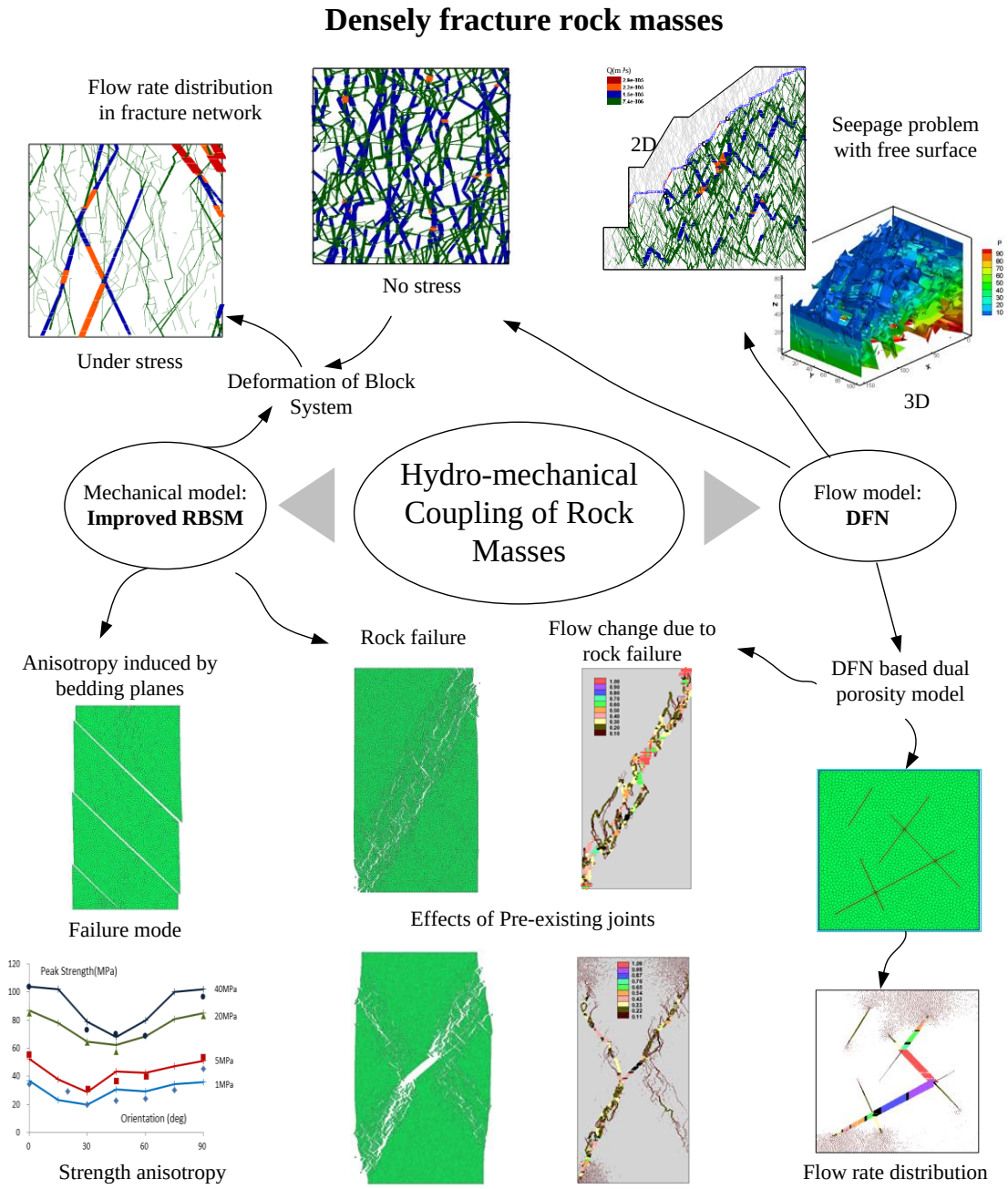

Figure 1.3 The main contents and basic structure of the thesis

In Chapter 1, rock failure process is simulated using an improved rigid body spring model (RBSM). A procedure based on point saturation theory is proposed to generate uniformly distributed random Voronoi cell, which is employed as the basic mesh for the improved RBSM. The midpoint contact model of original RBSM is modified into distributed interface contact model. A simple failure criterion combining Mohr-Coulomb criterion with tension strength is employed to account for fracture evolution. It is found

from a series of numerical tests that mesh size and mesh arrangement have little effects on the relationship between macro-level and meso-level elastic parameters. A fitting formula is developed for determination of relationship between macro and micro elastic parameters. Numerical studies against Vienne rock tests under various confining pressures show that a good agreement is obtained between experiments and numerical results from the proposed model.

In chapter 2, the improved rigid body spring model proposed in chapter 1 is extended to simulate the behaviors of sedimentary rocks. The main focus is on anisotropy of strength with regards to the orientation of bedding planes to loading direction. Effects of the deformation and failure properties of bedding planes on the macro strength are systematically analyzed. A two-step micro parameter calibration procedure is implemented against experiment results reported in the literature. With the calibrated micro parameters, a reasonable agreement is obtained between numerical results and experimental results under different confining pressures.

In chapter 3, permeability variation in the whole process of rock failure is studied based on the combination of the improved RBSM and DFN model. A DFN based dual porosity model is developed based on the mesh of uniformly Voronoi Diagram. The validity of this model is demonstrated by a simple case in the literature. Effects of some geometrical parameters of the pre-existing joints on the effective conductivity of the rock mass are investigated, including orientation, aperture, length, intersection relation of multi pre-existing joints. The improved RBSM is used to model the rock failure process. Numerical tests have been conducted on intact rock specimen and the pre-cracked rock under biaxial compression with different confining pressures. Typical failure modes and increase of conductivity by about 5 orders of magnitude are observed after peak strength. The significant increase in conductivity is observed in the softening and residual phase, during which the global rock failure takes place and the percolation threshold is attained.

In chapter 4, the partial differential equations (PDEs) defined on the whole fracture network domain are formulated for free-surface seepage flow problems by an extension of Darcy's law. A variational inequality (VI) formulation is then presented, and the proof of the equivalence between the PDE and VI formulations is given. Since the boundary conditions involving the flux components in the PDE formulation become the natural conditions in the VI formulation, the difficulty of choosing the trial functions for numerical solutions is significantly reduced and the locations of seepage points can be easily determined. On the basis of the discrete VI, the corresponding numerical procedure for

unconfined seepage analysis of discrete fracture network has been developed. The results from three typical examples demonstrate the validity and capability of the procedure for unconfined seepage problems involving complicated fracture networks.

In chapter 5, the VI formulation proposed in chapter 4 is extended to three dimensional (3D) seepage problems with free surface in fracture networks. The finite element algorithm is formulated. Space block search technology is used to determine a connected three-dimensional fracture network in polygonal shapes, i.e. seepage paths. With triangulation on these polygons, finite element mesh for 3D fracture network seepage is obtained. By contrast with an example in the homogeneous rectangular Dam, validity of the algorithm is verified. Analysis of an unconfined seepage problem in a complex fracture network shows that the proposed algorithm is very applicable to complex three-dimensional problems, and succeeds in describing some interesting phenomenon usually encountered in practice, such as "preferential flow".

In chapter 6, a numerical model for simulation of hydro-mechanical coupling and solute transport in densely fractured rock mass is developed. To realistically reflect changes in fracture aperture under complex stress conditions, a non-linear fracture constitutive model is introduced into Rigid Body Spring model, taking into account the non-linear normal stress and deformation relationship, tangential shear slip and dilation effects. Based on this method and combining a discrete fracture network model, an implicit hydro-mechanical coupling model is established. Since fractures are explicitly considered, evolution of fracture networks during coupling process can be accurately simulated. A particle tracking method is used to simulate solute transport in fracture network after converge of coupling process is obtained. Corresponding program is developed in accordance with the proposed model. An example from Decovalex project is analyzed to study the impact of different stress conditions on flow and solute transport. Key mechanisms controlling the coupling process is studied, and it’s found that under low stress ration and high stress ratio conditions, coupling process are mainly controlled by normal stress displacement relation and dilation effects respectively. Through comparing with other's work, the validity of the proposed model is demonstrated. The necessity is discussed of considering hydro-mechanical coupling effect under high water head condition.

Reference:

[1] Harrison, John P., and John A. Hudson. Engineering rock mechanics-an introduction to the principles. Elsevier Science, 2000.

[2] Z. T. Bieniawski, “Determining rock mass deformability: experience from case histories”, International Journal of Rock Mechanics and Mining Sciences & Geomechanics Abstracts, vol 15, no 5, pp 237–247, 1978.

[3] Y.-C. Liu and C.-S. Chen, “A new approach for application of rock mass classification on rock slope stability assessment”, Engineering Geology, vol 89, no 1–2, pp 129–143, 2007.

[4] E. Hoek and M. S. Diederichs, “Empirical estimation of rock mass modulus”, International Journal of Rock Mechanics and Mining Sciences, vol 43, no 2, pp 203–215, 2006.

[5] N. Barton, R. Lien, and J. Lunde, “Engineering classification of rock masses for the design of tunnel support”, Rock Mechanics, vol 6, no 4, pp 189–236, Dec 1974.

[6] E. Hoek and E. T. Brown, “Practical estimates of rock mass strength”, International Journal of Rock Mechanics and Mining Sciences, vol 34, no 8, pp 1165–1186, 1997.

[7] L. Jing and O. Stephansson, Fundamentals of Discrete Element Methods for Rock Engineering: Theory and Applications: Theory and Applications. Elsevier, 2007.

[8] J. Rutqvist and O. Stephansson, “The role of hydromechanical coupling in fractured rock engineering”, Hydrogeology Journal, vol 11, no 1, pp 7–40, Feb 2003.

[9] T. Kawai, “New discrete models and their application to seismic response analysis of structures”, Nuclear Engineering and Design, vol 48, no 1, pp 207–229, 1978.

[10] T. Belytschko, M. Plesha, and C. H. Dowding, “A computer method for stability analysis of caverns in jointed rock”, International Journal for Numerical and Analytical Methods in Geomechanics, vol 8, no 5, pp 473–492, 1984.

[11] Wang, Baolin, and Vinod K. Garga. "A numerical method for modelling large displacements of jointed rocks. I. Fundamentals." Canadian Geotechnical Journal 30.1 (1993): 96-108.

[12] Garga, Vinod K., and Baolin Wang. "A numerical method for modelling large displacements of jointed rocks. II. Modelling of rock bolts and groundwater and applications." Canadian Geotechnical Journal 30.1 (1993): 109-123.

[13] J. E. Bolander Jr. and S. Saito, “Fracture analyses using spring networks with random geometry”, Engineering Fracture Mechanics, vol 61, no 5–6, pp 569–591, 1998.

[14] K. Nagai, Y. Sato, and T. Ueda, “Mesoscopic Simulation of Failure of Mortar and Concrete by 2D RBSM”, Journal of Advanced Concrete Technology, vol 2, no 3, pp 359–374, 2004.

[15] K. Nagai, Y. Sato, and T. Ueda, “Mesoscopic Simulation of Failure of Mortar and Concrete by 3D RBSM”, Journal of Advanced Concrete Technology, vol 3, no 3, pp 385–402, 2005.

[16] L. Wang and T. Ueda, “Mesoscale Modelling of the Chloride Diffusion in Cracks and Cracked Concrete”, Journal of Advanced Concrete Technology, vol 9, no 3, pp 241–249, 2011.

[17] T. Ueda, M. Hasan, K. Nagai, Y. Sato, and L. Wang, “Mesoscale Simulation of Influence of Frost Damage on Mechanical Properties of Concrete”, Journal of Materials in Civil Engineering, vol 21, no 6, pp 244–252, 2009.

[18] K. Matsumoto, Y. Sato, T. Ueda, and L. Wang, “Mesoscopic Analysis of Mortar under High-Stress Creep and Low-Cycle Fatigue Loading”, Journal of Advanced Concrete Technology, vol 6, no 2, pp 337–352, 2008.

[19] M. Pieri, L. Burlini, K. Kunze, I. Stretton, and D. L. Olgaard, “Rheological and micro-structural evolution of Carrara marble with high shear strain: results from high temperature torsion experiments”, Journal of Structural Geology, vol 23, no 9, pp 1393–1413, 2001.

[20] W. Herbert, “Modelling approaches for discrete fracture network flow analysis”, in Developments in Geotechnical Engineering, vol Volume 79, L. J. and C.-F. T. Ove Stephansson, Ed Elsevier, 1996, pp 213–229.

[21] B. Berkowitz, “Characterizing flow and transport in fractured geological media: A review”, Advances in Water Resources, vol 25, no 8–12, pp 861–884, 2002.

[22] Sahimi, Muhammad. Flow and transport in porous media and fractured rock. Wiley-VCH, 2012.

[23] Dershowitz, William S., Paul R. La Pointe, and Thomas W. Doe. "Advances in dicrete fracture network modeling." Proceedings of the US EPA/NGWA Fractured Rock Conference, Portland. 2004.

[24] B. Berkowitz, “Analysis of fracture network connectivity using percolation theory”, Mathematical Geology, vol 27, no 4, pp 467–483, 1995.

[25] Balberg, B. Berkowitz, and G. E. Drachsler, “Application of a percolation model to flow in fractured hard rocks”, J. Geophys. Res., vol 96, no B6, pp 10015–10,021, 1991.

[26] J. Erhel, J.-R. de Dreuzy, and B. Poirriez, “Flow Simulation in Three-Dimensional

Discrete Fracture Networks", SIAM Journal on Scientific Computing, vol 31, no 4, pp 2688–2705, Jan 2009.

[27] M. Wang, P. H. S. W. Kulatilake, B. B. Panda, and M. L. Rucker, "Groundwater resources evaluation case study via discrete fracture flow modeling", Engineering Geology, vol 62, no 4, pp 267–291, 2001.

[28] V. V. Mourzenko, J.-F. Thovert, and P. M. Adler, "Macroscopic permeability of three-dimensional fracture networks with power-law size distribution", Phys. Rev. E, vol 69, no 6, p 066307, 2004

[29] V. V. Mourzenko, J.-F. Thovert, and P. M. Adler, "Percolation of three-dimensional fracture networks with power-law size distribution", Phys. Rev. E, vol 72, no 3, p 036103, 2005.

[30] M. Khamforoush, K. Shams, J.-F. Thovert, and P. M. Adler, "Permeability and percolation of anisotropic three-dimensional fracture networks", Phys. Rev. E, vol 77, no 5, p 056307, 2008.

[31] Pouya and O. Fouché, "Permeability of 3D discontinuity networks: New tensors from boundary-conditioned homogenisation", Advances in Water Resources, vol 32, no 3, pp 303–314, 2009.

[32] N. Koudina, R. Gonzalez Garcia, J.-F. Thovert, and P. M. Adler, "Permeability of three-dimensional fracture networks", Phys. Rev. E, vol 57, no 4, pp 4466–4479, 1998.

[33] V. V. Mourzenko, I. I. Bogdanov, J.-F. Thovert, and P. M. Adler, "Three-dimensional numerical simulation of single-phase transient compressible flows and well-tests in fractured formations", Mathematics and Computers in Simulation, vol 81, no 10, pp 2270–2281, 2011.

Chapter 2 A Mesoscopic Model for Simulation of Rock Failure

2.1 Introduction

Rock can be represented as a heterogeneous material comprised of cemented grains. Due to the difficulties for classical continuum methods in modeling discontinuity and heterogeneity, discrete element methods have witnessed great growth in investigating the complex mechanical properties of geo-materials and have been systematically applied in geotechnics [1]. Discrete element methods, in which the geo-material is represented as an assemblage of independent elements bonded together by cohesive forces or cementation effects, have been quite successful in simulating heterogeneity as well as damage localization and fracture [2].

The bonded particle model, proposed by Potyondy and Cundall [3], is based on the distinct element method and can reproduce many features of rock behavior, including elasticity, fracturing, acoustic emission, damage accumulation producing material anisotropy, hysteresis, dilation, post-peak softening, etc., qualitatively and quantitatively. This method represents the main stream in this area. However, it is shown that particle size has an influence on numerical results. Different packing assemblies of particles can also affect macro properties [4] [5]. That's why each packing specimen which is randomly generated must be calibrated by using specific algorithms. These indicate that discrete element methods modeling geo-material have a common problem of "mesh dependency".

The main aim of this study is to develop a discrete based model to simulate behaviors of geo materials while minimizing the effects of mesh size and arrangement on simulation results such as macro elastic parameters and strength.

The rigid block spring method, first proposed by Kawai [6],is a very suitable method for static and small deformation problems in rock mechanics and has been used to model behaviors of concrete and concrete structures [7],[8]. To more accurately simulate stress distribution along interface between blocks, Zhang [9], Qian [10] and Zhuo [11] developed this method and used it for limit analysis of rock slopes and other engineering structures.

The basic element for this method is polygon. Bolander and Saito [12] used RBSM for fracture analysis of concrete with uniform Voronoi diagram as basic mesh. They found that using this type of mesh has a great advantage in ensuring elastic uniformity and maximizing the degree of isotropy with respect to potential crack direction. Voronoi diagram has also been used

for dense packing simulation based on distinct element method [13].

In this study, the rock specimen is modeled as an assemblage of polygonal discrete elements and an Improved RBSM, which is based on the work of Zhuo [11] and Qian [10], is employed as the numerical tool to simulate responses of discrete element system to different loading conditions. Uniformly and randomly generated Voronoi cells are used as basic elements. Effects of element size and mesh arrangement on relationship between macro elastic parameters and micro elastic parameters and on strength are systematically investigated.

2.2 Basic Theory of the Voronoi based Improved Rigid Block Spring Method

2.2.1 Fundamental formula

In the Improved RBSM, rock is modeled as an assemblage of rigid blocks interconnected along their boundaries. Each block has two translational and one rotational degrees of freedom defined at its centroid. Two neighboring blocks share a common boundary. The interface between two neighboring blocks can be represented by normal springs and tangential springs uniformly distributed along the boundary, which can be read in figure 2.1. However, not like what is shown in Figure 2.1(a), springs have zero size. The normal and tangential springs are assigned stiffness k_n and k_s. This is similar to the Goodman Element [14], having the advantage of simulating distributed stress along the interface. The basic difference of this method from the original RBSM is that, in the original RBSM there are only three springs positioned at the mid-point of the interface, a normal spring, a tangential spring and a rotational spring, which is shown in Figure 2.1 (b). Since the distributed springs have the capacity to resist moment, the rotational spring is eliminated in the modified RBSM.

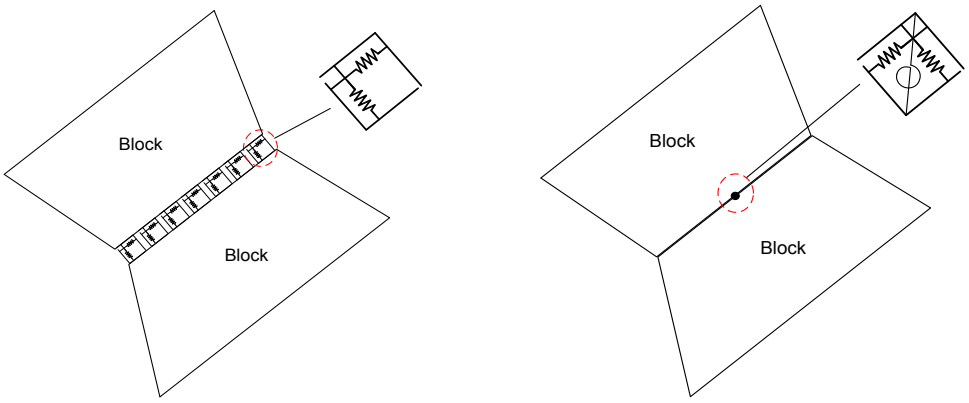

(a) Model for the Improved RBSM (b) Model for the original RBSM

Figure 2.1 Illustration of contact models for modified and original RBSM

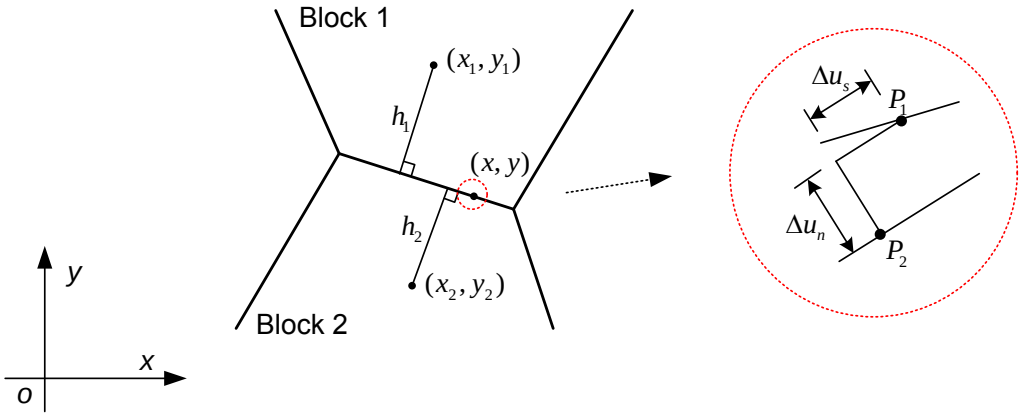

Figure 2.2 Local displacement for point on the contact interface

The global equations for the Improved RBSM can be derived from Virtual Work Theorem, which is simply given below. Suppose that two arbitrary blocks block 1 and block 2, the centroid of which are (x_1, y_1) and (x_2, y_2) respectively, are next to each other, and point P_1 on block 1and point P_2 on block 2 coincide in the same point (x, y) along the boundary between the two blocks, as can be seen in Figure 2.2 Assuming rotations are small, the relative displacements between point P_1 and point P_2, $\{\triangle u\}$, can be expressed by the displacements of centroids of the two blocks $\{U\}_{12}$ as,

$$\{\Delta u\} = [B][N]\{U\}_{12} \tag{2-1}$$

Where, $\{\Delta u\} = \{\Delta u_n \quad \Delta u_s\}^T$, Δu_n and Δu_s are respectively the relative normal and tangential displacements between point P_1 and point P_2.

$$[B] = \begin{bmatrix} l & m \\ -m & l \end{bmatrix},$$

$\{l, m\}$ is the unit normal vector of the interface.

$$[N] = \begin{bmatrix} -1 & 0 & y_{10} & 1 & 0 & -y_{20} \\ 0 & -1 & -x_{10} & 0 & 1 & x_{20} \end{bmatrix}$$

$x_{10} = x - x_1$, $y_{10} = y - y_1$, $x_{20} = x - x_2$, $y_{20} = y - y_2$

$\{U\}_{12} = \{U_{1x} \quad U_{1y} \quad U_{1\theta} \quad U_{2x} \quad U_{2y} \quad U_{2\theta}\}^T$, $U_{1x} \quad U_{1y} \quad U_{1\theta}$ are respectively the translational displacement in x direction, translational displacement in y direction, rotational displacement of the centroid of block 1, while $U_{2x} \quad U_{2y} \quad U_{2\theta}$ are displacement components of the centroid of block 2.

Then, the stress induced by relative displacements between point P_1 and point P_2 can be expressed by $\{\Delta u\}$ as

$$\{\sigma\} = [D]\{\Delta u\} \tag{2-2}$$

Where, $\{\sigma\}=\{\sigma_n, \sigma_s\}^T$, σ_n, σ_s are normal stress and tangential stress, respectively.

$[D] = \begin{bmatrix} k_n & 0 \\ 0 & k_s \end{bmatrix}$, k_n is the stiffness of normal spring and k_s is the stiffness of tangential spring.

Applying virtual work theorem, for any block in the block system, the relationship below stands

$$\sum_e \left(\int_{l_0^e} \{\delta(\Delta u)\}^T \{\sigma\} dl + \int_{l_\sigma^e} \{\delta u\}^T \{p\} dl + \iint_{s^e} \{\delta u\}^T \{f\} ds \right) = 0 \tag{2-3}$$

Where l_0^e, l_σ^e, s^e stand for interface between blocks, force boundary and domain of blocks, respectively; $\{p\}, \{f\}, \{\delta u\}, \{\delta(\Delta u)\}$ are respectively external pressure, body force, virtual displacement, and virtual relative displacement.

In this study, the gravity of blocks is ignored, so equation (2-3) is simplified to

$$\sum_e \int_{l_0^e} \{\delta(\Delta u)\}^T \{\sigma\} dl = -\sum_e \int_{l_\sigma^e} \{\delta u\}^T \{p\} dl \tag{2-4}$$

Together with above relations, the global equilibrium equation for the whole block system can be obtained,

$$[K]\{U\} = \{F\} \tag{2-5}$$

The global stiffness matrix $[K]$ is obtained through a process similar to finite element method. For more details on algorithms for boundary conditions, readers can refer to Shi [15] and Wang[16].

2.2.2 Mesh generation

The method described above can be used for any polygon-based mesh arrangement. For the sake of automatic mesh generation and many other important advantages, rock specimens are considered as rectangular domains divided by uniformly and randomly distributed Voronoi cells, which are also called as “mesh” here. Mesh generation procedure consists of two main steps [12],[17], which is detailed below and shown in Figure 2.3.

The first step is to randomly generate a set of uniformly distributed points in the domain. If the minimum distance between any two points is set to be $d_{\min}$, in a rectangular domain $a \times b$, the maximum number of points n can be calculated by

$$n \approx 0.68ab / d_{\min}{}^2 \tag{2-6}$$

With the maximum number of points and the minimum distance between two arbitrary points, a uniformly distributed set of points can be obtained through an iterative random process using Monte Carlo method. The calculation expense is very great when the number of points generation is large since each pair of points should be checked whether their distance exceed the minimum distance $d_{\min}$. To make this process effective, a grid search algorithm is used [18].

The second step is to generate Voronoi diagram with the points obtained in the first step. Voronoi diagram is a special kind of decomposition of a given space determined by a set of sites in the space. In its simplest case with Euclidean plane, each site P_k is simply a point, and its corresponding Voronoi cell R_k consisting of all points whose distance to P_k, denoted as $d(x, P_k)$, is not greater than their distance to any other site P_j, denoted as $d(x, P_j)$, which can be more formally defined as

$$R_k = \{x \in X \mid d(x, P_k) \le d(x, P_j), \text{ for all } j \ne k\} \tag{2-7}$$

A Voronoi diagram is uniquely determined by the set of sites specified. As a result, an appropriate Voronoi diagram can be obtained through just adjusting the number and the distribution of sites. With points get in the first step, a uniformly and randomly distributed set of Voronoi cells can be obtained. There are plenty of effective algorithms for Voronoi diagram generation in literatures. In this study, an open code originated from Steven Fortune[19] and then developed by Shane O'Sullivan is employed.

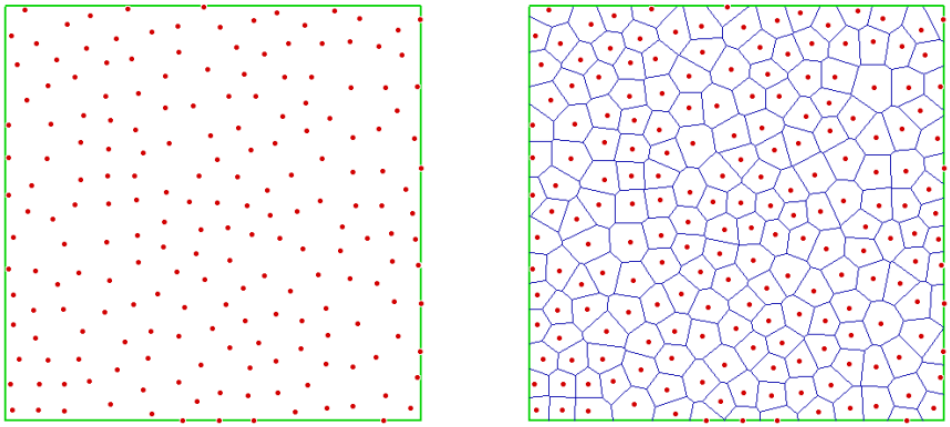

(a) step 1: points generation (b) step 2: Voronoi diagram

Figure 2.3 Illustration of mesh generation

2.2.3 Fracture Criterion

In the Vononoi based Improved RBSM, the basic element—Vononoi Cell is undeformable and unbreakable, all internal energy is restored in the element interface. Assuming that damage is induced by energy dissipation in tension and shearing, a simple fracture criterion is introduced at the interface contact level.

For Mode I fracturing, tension strength T is set for all interface contacts and a brittle response is assumed. Once the tension stress σ_n of a point on a contact interface is over the tension strength T, a tension failure case is spotted and the interaction stresses σ_n and σ_s are simply set to be zero. For Mode II fracturing, a Mohr-Column type criterion is employed as a shear strength law. This criterion is defined by a frictional angle ϕ, cohesive strength C and a critical normal stress σ_{cr}. The maximum shear stress can be calculated by

$$|\sigma_{s\max}| = -\sigma_n \cdot \tan\phi + C, \quad \sigma_n \geq \sigma_{cr} \tag{2-8.1}$$

$$|\sigma_{s\max}| = -\sigma_{cr} \cdot \tan\phi + C, \quad \sigma_n < \sigma_{cr} \tag{2-8.2}$$

In the case of a shear failure, the interaction stress σ_n and σ_s are reduced from a cohesive frictional relationship to a sliding frictional relationship. The fracture criterion law is illustrated in Figure 2.4. To make things much simpler, T is chosen as $0.3C$. Thus the fracture criterion has only three parameters.

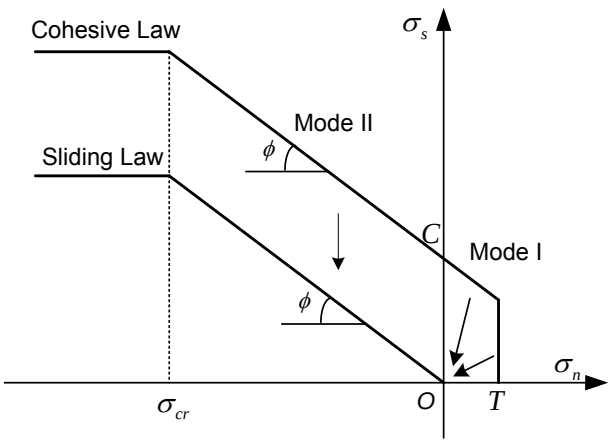

Figure 2.4 Fracture criterion which combines the Mohr-Column law and a tension strength law

A four point Gauss-Chebyshev integration formula is used for the Integration of equation (2.3) and (2.4). The modified Newton-Raphson method is adopted for the nonlinear iterative calculation. For simulation of post peak behaviors, loading is controlled by displacement. A code named VoronoiRBSM is programmed with Visual C++ based on the proposed method. Displacement step is chosen as 1×10^{-7}m for every compression test

and 1×10^{-8}m for every tension test in this study. The convergence in every displacement step is judged by the overall unbalance force. If the convergence condition is not met, a maximum iterative number of 400 for each step is set.

2.3 Relationships between micro and macro elastic parameters

Marco-scopic elastic parameters are Young's modulus E and poison ratio υ, and micro elastic parameters includes normal stiffness k_n and tangential stiffness k_s.

To investigate the relationship between macro and micro elastic parameters, and the effects of element size and element arrangements on this relationship, a series of numerical experiments are conducted.

The micro elastic parameters for an interface are simply calculated through equations below,

$$k_n = \frac{E_0}{h_1 + h_2} \tag{2-9.1}$$

$$k_s = r \cdot k_n \tag{2-9.2}$$

Where, E_0 is a predetermined modulus, which has the same order of magnitude with the macro E; r is the ratio between k_s and k_n; h_1 and h_2 denote the distances from the centroids of two neighboring elements to their connecting interface, respectively, which is illustrated in Figure 2.2.

Four groups of numerical specimens are generated through mesh generation procedure described above. The rectangular domain is 0.05m×0.1m. Each group has 10 different randomly generated specimens and specimens in the same group have a same number of elements, which are 1000, 5000, 10000, 50000, respectively. Typical specimens for each group are illustrated in Figure 2.5.

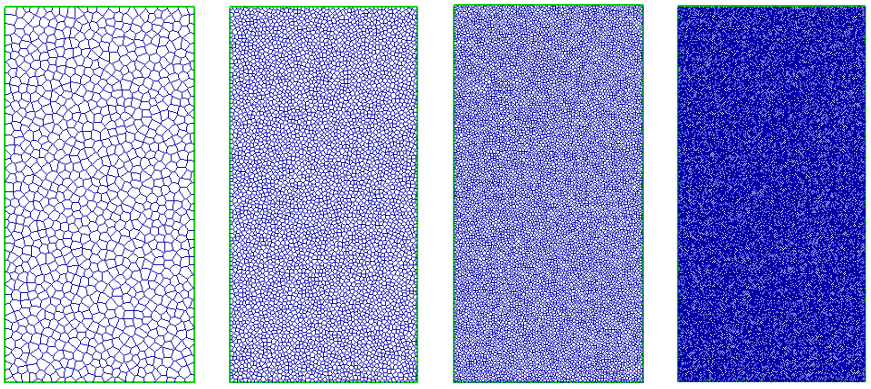

(a) n=1000 (b) n=5000 (c) n=10000 (d) n=50000

Figure 2.5 Typical model for specimens with different number of elements

Uniaxial experiment is conducted on each specimen under elastic conditions with no failure accounted. Loading is controlled by displacement, denoted by *d*. Loading condition is illustrated in fig 2.10. E_0 is chosen as 30GPa, *r* is chosen between 0.1 and 0.96, with a step gap of 0.05.

Young's modulus *E* is calculated by

$$E = \frac{P}{\varepsilon_1} \tag{2-10}$$

Where, *P* is the average pressure imposed on the upper or lower boundary; ε_1 is the axial strain obtained by $\varepsilon_1 = d/b$, *b* is the height of the specimen.

Poison ratio is calculated by

$$v = \frac{\varepsilon_3}{\varepsilon_1} \tag{2-11}$$

Where ε_3 is the lateral strain, calculated by $\varepsilon_3 = (d_r - d_l)/a$, d_l, d_r are the average displacement of left boundary and right boundary respectively, *a* denotes the width of the specimen.

Relationships between *v* and *r* for each specimen and each group are shown in Figure 2.6. From this graph, it can be seen that when the number of elements is 1000, there is a little variance among ten curves of each specimen in this group, while with the number increases, the variance decreases and ten curves almost coincide with each other especially when the number reaches 10000 and 50000. This indicates that when the number of elements is large enough (i.e. ＞5000), changing mesh arrangement has little impact on the relationship between *v* and *r*. By putting the average curve of each group together, Figure 2. 7 is obtained. It can be observed from this graph that curves for each group almost coincide with each other, showing that no obvious influence on the relationship between *v* and *r* is induced by variance of element size.

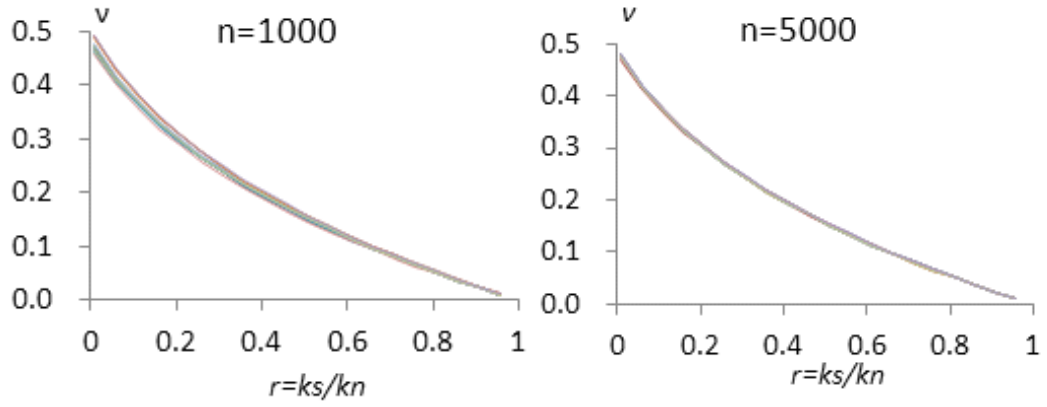

(a) n=1000 (b) n=5000

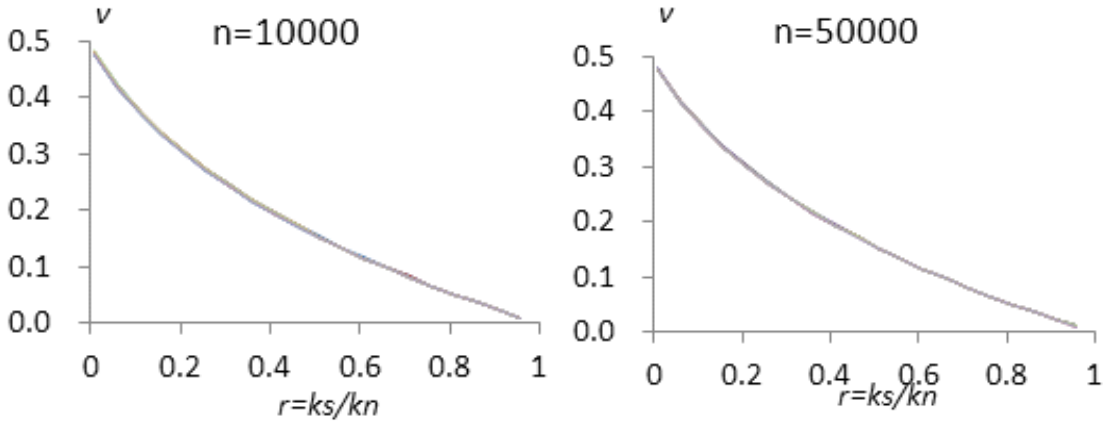

(c) n=10000 (d) n=50000

Figure 2.6 Relationship between *v* and *r* for every specimen respectively in six groups

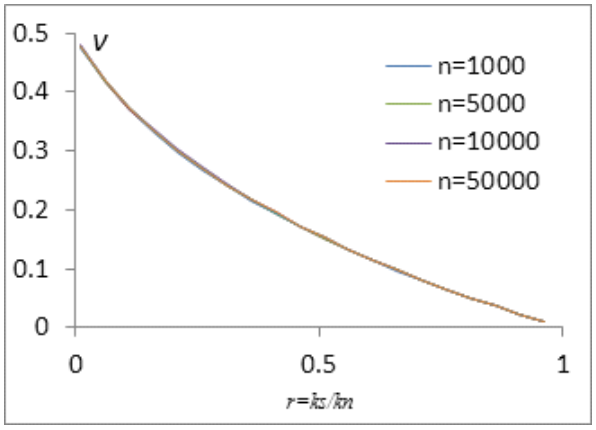

Figure 2.7 Relationships between *v* and *r* of average results from six groups

Relationships between E/E_0 and r for each specimen and each group are shown in Figure 2.8. From this figure, it can be seen that when the number of elements is 1000, there is a little variance among ten curves of each specimen in this group, while with the number increases, the variance decreases and ten curves almost coincide with each other especially when the number reaches 10000 and 50000. This indicates that when the number of elements is large enough (5000), changing mesh arrangement has little impact on the relationship between E/E_0 and r. By putting the average curve of each group together, Figure 2.9 is obtained. It can be observed from this graph that curve gets lower with the number of elements increases, and the three curves for n=10000, 20000 and 50000 almost coincide with each other, showing that element size can affect the relationship between E/E_0 and r when the number of elements is not large enough, but when the number is larger than some specified value (10000 for example), no obvious influence on the relationship between E/E_0 and r induced by variance of element size can be observed.

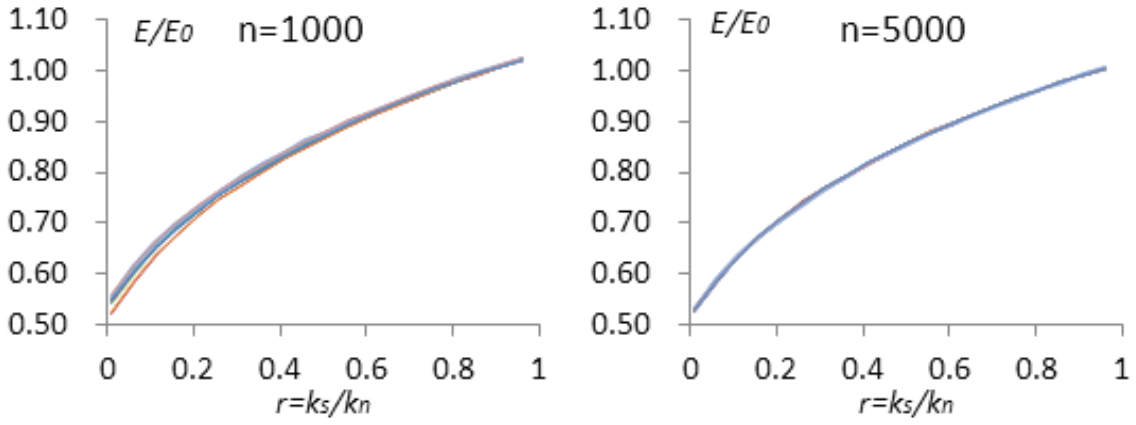

(a) n=1000

（b）n=5000

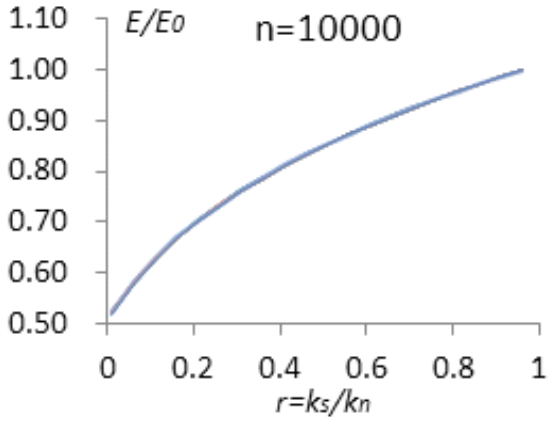

(c) n=10000

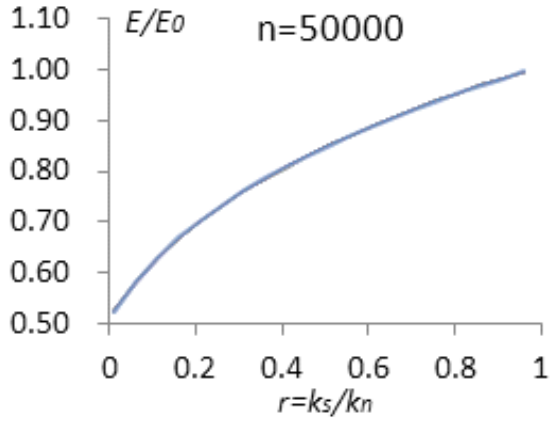

(d) n=50000

Figure 2.8 Relationship between E / E_0 and r for every specimen respectively in six groups

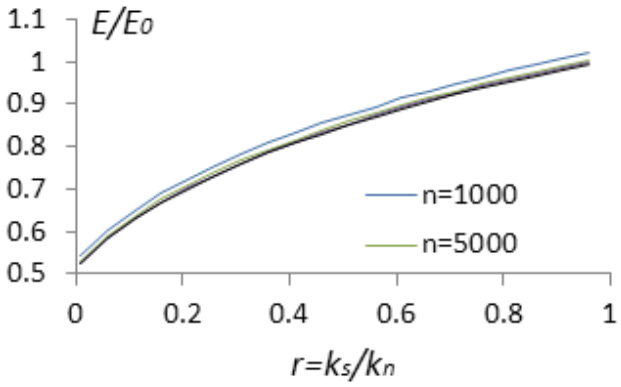

Figure 2.9 Relationships between E/E_0 and r of average results from six groups

From results of numerical experiments discussed above, it can be seen that when the number of elements is large enough, element size and element arrangement have little influence on the relationship between micro and macro elastic parameters. Based on this fact, two fitting formulas are drawn from the average results of group 6, the number of elements for each specimen in which is 50000:

$$r = k_s / k_n = 4.025\nu^4 - 6.087\nu^3 + 6.022\ \nu^2 - 3.966\nu + 1 \quad (2\text{-}12.1)$$

$$E / E_0 = -0.6291r^4 + 1.617r^3 - 1.678r^2 + 1.174r + 0.5162 \quad (2\text{-}12.2)$$

It is very convenient to determine micro elastic parameters k_n and k_s with macro elastic parameters E and ν by simply substituting equation (2-12) into equation (2-9).

2.4 Comparison with experiment data

A numerical specimen with 10000 elements is adopted for simulation. Input parameters listed in Table 2.1 are employed for simulation of Vienne rock. E and ν are directly adapted after experiment data while $\tan\phi$, C and σ_{cr} are determined through an error and try calibration algorithm with the uniaxial compression experiment.

Table 2.1 Input parameters for simulation of biaxial experiments on Vienne rock

E	ν	$\tan\phi$	C	T	σ_{cr}
72GPa	0.22	0.95	57MPa	17.1MPa	100MPa

Boundary conditions are shown in Figure 2. 10 for both biaxial compression and uniaxial tension tests. Simulation of fracture evolution during the uniaxial compression test is illustrated in Figure 2.11 and failure pattern in tension is illustrated in Figure 2.12.

Figure 2.13 gives the stress strain curve of the tension test simulation and the tension strength is 11.10MPa, which is 1/12.4 of the compression strength. Comparison between simulation and experiment on biaxial tests is shown in Figure 2.14. Figure 2.14(a) is comparison on uniaxial compression test, from which a residual strength of 70.4MPa is also given. Overall, simulation results fit well with experiment data. Comparison of stress state of yielding between experiment and simulation under different stress boundaries is shown in Figure 2.15, which also shows a great agreement.

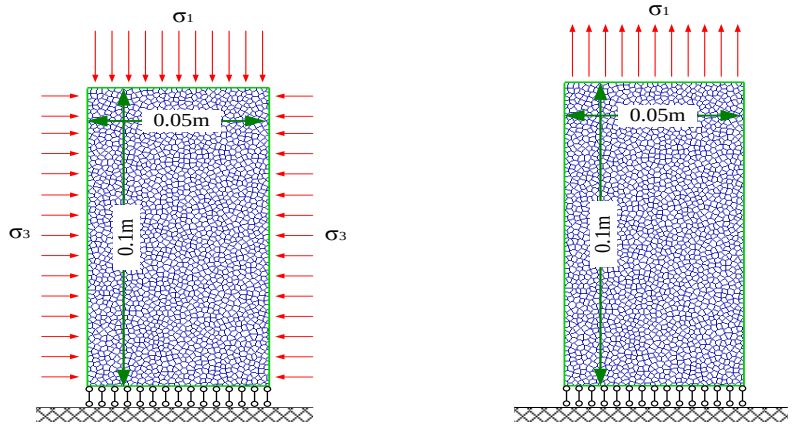

(a) boundary condition for compression tests (b) boundary condition for tension tests

Figure 2.10 Boundary conditions and geometry for tension and biaxial compression tests

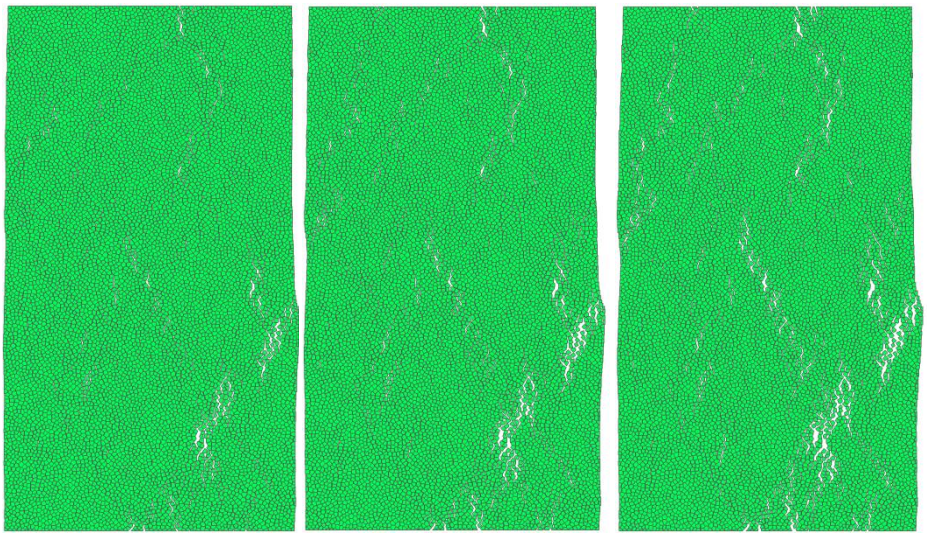

(a) Axial strain=2250 (b) Axial strain=2300 (c) Axial strain=2350

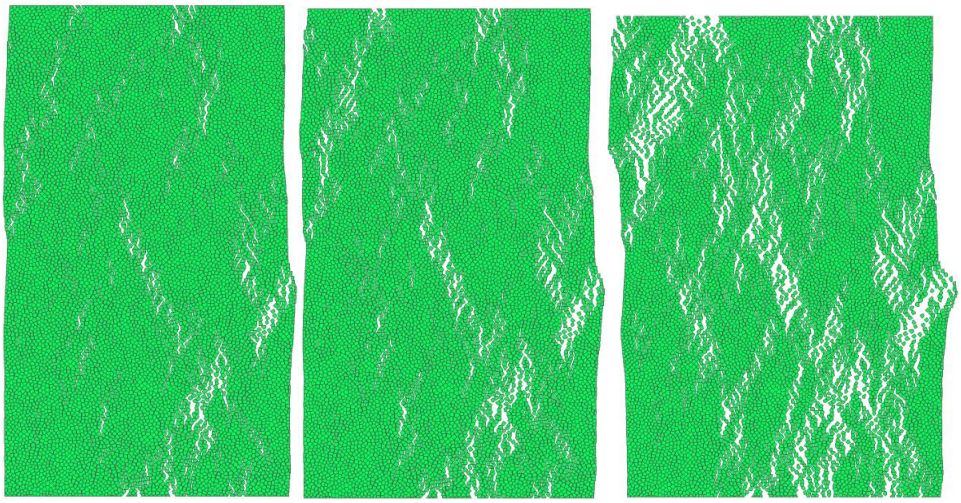

(d) Axial strain=2400 (e) Axial strain=2450 (f) Axial strain=2500

Figure 2.11 Illustration Fracture evolution during uniaxial compression test (Deformation in x direction* 50)

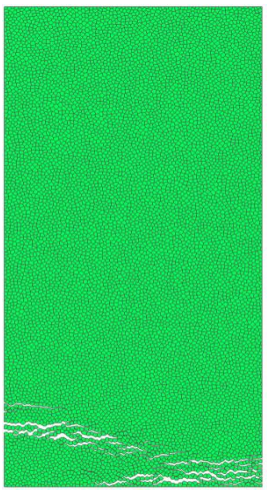

Figure 2.12 Failure pattern in tension (Axial strain=200, deformation in y direction*100)

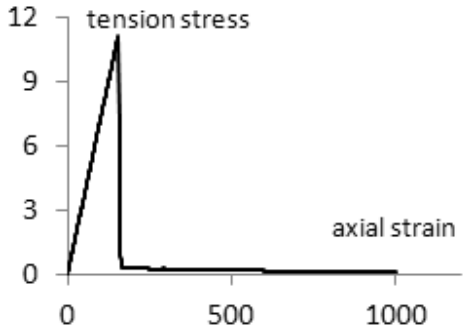

Figure 2.13 Stress strain curve for uniaxial tension simulation
(unit of strain: 1e-6，unit of stress: MPa)

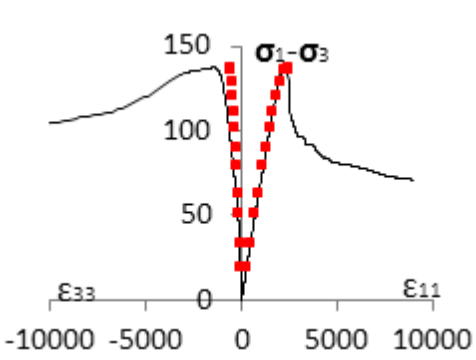

(a) σ_3=0MPa

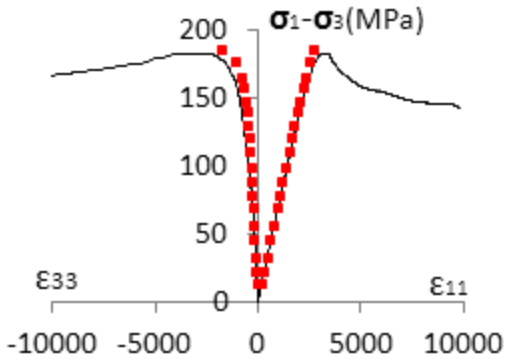

(b) σ_3=5MPa

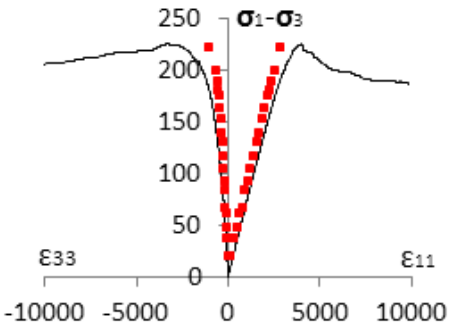

(c) σ_3=10MPa

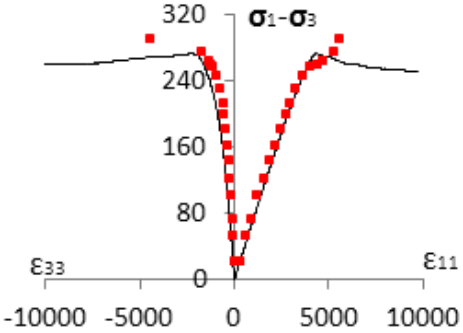

(d) σ_3=20MPa

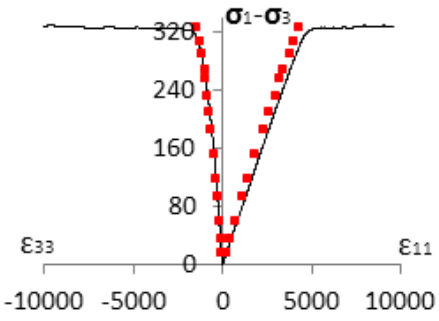

(e) σ_3=40MPa

Figure 2.14 Comparison between simulation and experiment on biaxial tests

(Unit of strain: 1e-6 Unit of stress: MPa)

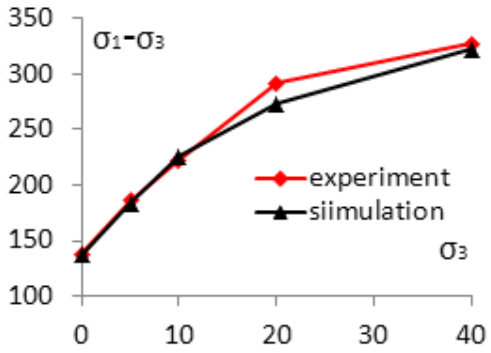

Figure 2.15 Comparison of peak strength between experiment and simulation under different stress boundaries

2.5 Discussion: Effects of element size and mesh arrangement on strength

To investigate effects of element size and mesh arrangement on strength under different confined pressure conditions, 3 groups of numerical experiments are conducted. Each group comprises of 10 randomly generated specimens. Every specimen has a same size of 0.05m × 0.1m. The input parameters for each specimen are same as well, which are listed in Table 2.2. But specimens in different group have different number of elements, which are 2000, 5000 and 10000 for group 1, group 2 and group 3, respectively. And, different specimens in the same group have different mesh arrangement since they are randomly generated. Three levels of confined pressure are chosen, which are 0MPa, 5MPa, and 10MPa.

Table 2.2 Input parameters for simulation of effects of mesh on strength

E	V	$\tan\phi$	C	T	σ_{cr}
30GPa	0.18	0.8	15MPa	4.5MPa	20MPa

Table 2.3 shows that variance on strength under different conditions of confined pressure induced by element size and mesh arrangement is very limited. With this fact, it can be stated that strength produced by Voronoi based Improved RBSM is independent of element size and mesh arrangement.

Table 2.3 Effects of mesh on strength under different confined pressure conditions

Confined Pressure	0 MPa		5 MPa		10 MPa	
Group	μ (MPa)	C_v (%)	μ (MPa)	C_v (%)	μ (MPa)	C_v (%)
1 (n=2000)	40,98	1,42	58,75	1,22	65,65	0,71
2 (n=5000)	40,37	0,57	58,53	0,74	65,74	0,63
3 (n=10000)	40,06	0,74	58,82	0,49	65,98	0,49

μ is the mean value of strength (σ_3–σ_1) of the ten specimens in each group.

C_v is the coefficient of variation, $C_v=\sigma/\mu$.

2.6 Conclusion

In this study, we proposed an improved Rigid block spring method based on uniformly distributed Voronoi diagram. A simple criterion which combines Mohr Column law and tension strength law is employed as the fracture criterion. It is found that there is an approximately fixed relationship between micro elastic parameters and macro elastic parameters. Based on this, two fitting formula are derived for determination of micro elastic parameters with macro elastic parameters. Comparison with experiments demonstrates that the proposed model can reproduce rock behaviors under tension and compression in both qualitatively and quantitative manner.

Reference

[1] L. Jing. A review of techniques, advances and outstandingissues in numerical modelling for rock mechanics and rock engineering. International Journal of Rock Mechanics and Mining Sciences. 40, 3, April 2003, Pages 283–353.

[2] Donze, F.V., V. Richefeu & S.-A. Magnier, Advances in Discrete Element Method applied to Soil, Rock and Concrete Mechanics, in: State of the art of geotechnical engineering, Electronic Journal of Geotechnical Engineering, p. 44, 2009

[3] D.O. Potyondy, P.A. Cundall. A bonded-particle model for rock. International Journal of Rock Mechanics & Mining Sciences 41 (2004): 1329–1364

[4] Yuannian Wang, Fulvio Tonon. Modeling Lac du Bonnet granite using a discrete element model. International Journal of Rock Mechanics & Mining Sciences 46 (2009) 1124–1135

[5] Sébastien Hentz, Laurent Daudeville, and Frédéric V. Donzé. Identification and Validation of a Discrete Element Model for Concrete. Journal of Engineering Mechanics. 130(6):709-720

[6] Tadahiko Kawai. New element models in discrete structural analysis. Journal of the Society of Naval Architects of Japan,141,187-193.

[7] J. E. Bolander Jr. *, Stefano Berton. Simulation of shrinkage induced cracking in cement composite overlays. Cement & Concrete Composites 26 (2004) 861–871

[8] Kohei Nagai, Yasuhiko Sato and Tamon Ueda. Mesoscopic Simulation of Failure of Motar and Concrete by 2D RBSM. Journal of Advanced Concrete Technology. 2004,2(3):359-374

[9] Zhang Xiong, Qian Lingxi. Rigid finite element and limit analysis. Acta Mechanica Sinica.9, 2 (1993):156-162

[10] Qian Lingxi, Zhang Xiong. Rigid finite element and its applications in engineering. Acta Mechanica Sinica. 11, 1 (1995): 44-50

[11] J.S.ZHUO, Q.ZHANG, N.ZHAO. Interface Stress Element Methods For Deformable Body With Discontinuous Media Such As Rock Mass. 8th ISRM Congress, September 25 - 29, 1995, Tokyo, Japan.

[12] J.E. Bolander, Jr, S. Saito. Fracture analysis using spring networks with random geometry. Engineering Fracture Mechanics. 61 (1998):569-591

[13] F. Camborde, C. Mariotti, F.V. Donze. Numerical study of rock and concrete behavior by discrete element modeling.Computers and Geotechnics 27 (2000): 225-247

[14] Goodman, R.E. (1976) Methods of geological engineering in discontinuous rocks, West Publishing Company, San Francisco, CA.

[15] Shi, G H. Discontinuous deformation analysis: a new numerical model for the statics and dynamics of deformable block structures. Engng ComputV9, N2, April 1992, P157–168

[16] Baolin Wang, Vinod K. Garga. A numerical method for modelling large displacements of jointed rocks. I. Fundamentals. Canadian Geotechnical Journal, 1993, 30(1): 96-108.

[17] Yip, M., Mohle, J. and Bolander, J. E. (2005), Automated Modeling of Three-Dimensional Structural Components Using Irregular Lattices. Computer-Aided Civil and Infrastructure Engineering, 20: 393-407. doi: 10.1111/j. 1467-8667. 2005. 00407.x

[18] Greengard, L., Rokhlin, V. (1987). A fast algorithm for particle simulations. Journal of Computational Physics, 73(2), 325–49.

[19] Steven Fortune (1987). A sweepline algorithm for Voronoi diagrams. Algorithmica. 2(1-4): 153-174

Chapter 3 Modeling behaviors of sedimentary rocks

3.1 Introduction

The sedimentary rocks are often encountered in foundations of civil structures. Characterization of Mechanical behaviors of the sedimentary rocks is of particular interest to the oil exploration industry and to mining engineering. The most common of this kind of rocks are shale, siltstone and clay stone. These rocks often exhibit strong inherent anisotropy and obvious directional dependence of deformation and other mechanical characteristics. This anisotropy is generally due to the presence of bedding planes which can be easily detected even by naked eyes.

Over the last few decades, extensive experimental studies were carried out to study the mechanical behaviors of sedimentary rocks [1, 2, 3, 4, 5, 6]. The main focus of these studies was strength anisotropy depending on the orientation of bedding planes with respect to the principal stress. The results show that the maximum axial compressive strength generally took place either at $0°$ or $90°$ (i.e. the bedding planes are parallel to or perpendicular to the direction the principal stress). And, the minimum strength typically occurred with an orientation within the range $30°\sim60°$, the corresponding failure mode of which was usually sliding along the weak planes.

In parallel with experimental studies, many scholars have developed several theoretical models and failure criteria to describe the mechanical behaviors of sedimentary rocks. Jaeger introduced an instructive analysis for the case where well-defined, parallel discontinuity is involved[7]. Based on this model, Duveau and Shao [8] provided a modification by replacing the Mohr–Coulomb criterion with a non-linear model to express the strength along discontinuity. Other scholars, such as McLamore and Gray [3], Hoek and Brown[9], Hill[10], Cazacu[11], Nova[12] and Tien [13] also proposed failure criteria , their models generally provide fairly accurate simulation of the experimental data. In general, those works are based on the formulation of the continuum mechanics, and very little work has been done for identification of the basic mechanism at the meso scale, perhaps due to the difficulty in explicitly modeling the microstructures.

The main aim of this chapter is to extend the improved rigid body spring model proposed in chapter 2 to simulate the behaviors of sedimentary rocks. The advantage of this method lies in that the microstructure of bedding plane is explicitly simulated. The main

focus is on anisotropy of strength with regards to the orientation of bedding planes to loading direction. Effects of the deformation and failure properties of bedding planes on the macro strength are systematically analyzed. The model presented here is applied to study the behaviors of Tournemire shale under different biaxial tests.

3.2 Fundamental theory of the modified rigid block spring method

Suppose that blocks are rigid, normal and tangential springs are uniformly distributed along interfaces between blocks, in which all internal energy is restored. There are three degrees of freedom for centroid of each block, i.e. displacement in x direction u_{cx}, displacement in y direction u_{cy}, and a rotation θ_c. Assuming only small rotation can take place, displacement of an arbitrary point on block $\{u\}$ can be expressed by $\{u_c\}$ as

$$\{u\} = [N]\{u_c\} \tag{3-1}$$

Where, $\{u\}^T=\{u_x\ u_y\}$ are displacements of this point; $\{u_c\}^T=\{u_{cx},\ u_{cy},\ \theta_c\}$ are degrees of freedom of the block;

$$[N] = \begin{Bmatrix} 1 & 0 & -(y-y_c) \\ 0 & 1 & (x-x_c) \end{Bmatrix} \tag{3-2}$$

Where, (x, y) is the global coordinate of this point and (x_c, y_c) is the global coordinate of the block centroid.

Then, relative displacements of one point on block interface $\{\triangle u\}$ can be expressed by displacements of the two neighboring blocks $\{u_c\}_1$ and $\{u_c\}_2$ as

$$\{\Delta u\} = [B]([N]_1\{u_c\}_1 - [N]_2\{u_c\}_2) = [B][N]_{12}\{u_c\}_{12} \tag{3-3}$$

Where，$\{\triangle u\}^T=\{\triangle u_n, \triangle u_s\}$，$\triangle u_n$，$\triangle u_s$ are relative displacements in normal and tangential direction;

$$[B] = \begin{bmatrix} l & m \\ -m & l \end{bmatrix} \tag{3-4}$$

Where, (l, m) is unit vector for the normal direction of the interface.

Once the relative displacements are obtained, stress can be calculated with the following equation,

$$\{\sigma\} = [D]\{\Delta u\} \tag{3-5}$$

In which，$\{\sigma\}^T=\{\sigma_n, \tau_s\}$，$\sigma_n$ and τ_s are normal and tangential stress;

$$[D] = \begin{bmatrix} k_n & 0 \\ 0 & k_s \end{bmatrix} \tag{3-6}$$

Where, k_n and k_s are respectively stiffness for the normal and tangential springs.

Based on the Virtual Work Theorem, the following equations stand [12]

$$\sum_e \left(\int_{l_0^e} \{\delta(\Delta u)\}^T \{\sigma\} dl + \int_{l_\sigma^e} \{\delta u\}^T \{p\} dl + \iint_{s^e} \{\delta u\}^T \{f\} ds \right) = 0 \tag{3-7}$$

Where, l_0^e、l_σ^e、s^e respectively denote interfaces, stress boundaries and block domains，$\{\delta u\}$is virtual displacement，$\{\sigma\}$, $\{\delta\triangle(u)\}$ are stress on interfaces and relative virtual displacement along interfaces，$\{p\}$ is loading stress，$\{f\}$ is body force. If body force is neglected, equation (3-7) is changed into

$$-\sum_e \int_{l_0^e} \{\delta(\Delta u)\}^T \{\sigma\} dl = \sum_e \int_{l_\sigma^e} \{\delta u\}^T \{p\} dl \tag{3-8}$$

Applying equation(3-1),(3-3),(3-5) into equation（3-8），the following equation can be obtained,

$$-\{\delta U\}^T \left(\sum_e \left(\int_{l_0^e} [N]_{12}^T [B]^T [D][B][N]_{12} dl \right) \right) \{U\} = \{\delta U\}^T \sum_e \left(\int_{l_\sigma^e} [N]^T [B]^T \{p\} dl \right) \tag{3-9}$$

Where, $\{\delta U\}$ is the global vector of virtual displacement of all blocks; $\{U\}$ is the global vector of displacement of all blocks. Eliminating $\{\delta U\}$， the global equilibrium equations is obtained,

$$[K]\{U\} = \{Q\} \tag{3-10}$$

Where，

$$[K] = -\left(\sum_e \left(\int_{l_0^e} [N]_{12}^T [B]^T [D][B][N]_{12} dl \right) \right);$$

$$\{Q\} = \sum_e \left(\int_{l_\sigma^e} [N]^T [B]^T \{p\} dl \right)$$

3.3 Constitutive law

A linear elastic relation is employed to describe the stress and displacement relation between two neighboring blocks for small deformation. The normal stress is calculated through local constitutive law shown in Figure 3.1 and is composed of two parts, the compressive and the tensile components. In this chapter, tension is defined as positive.

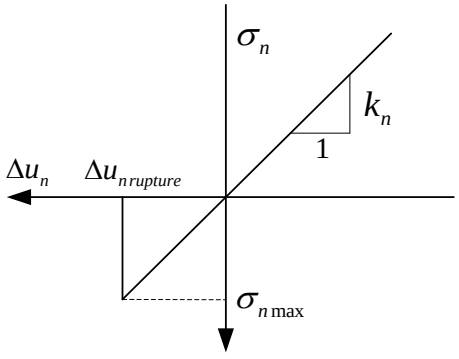

Figure 3.1 Normal stress-displacement relationship between two blocks

In compression, σ_n is given by

$$\sigma_n = k_n \Delta u_n \tag{3-11}$$

Where, Δu_n is the relative displacement between interacting blocks and k_n is the normal stiffness.

In tension, the normal stress is still computed with the same stiffness in compression. The maximum tensile stress $\sigma_{n\max}$ is equal to the tensile strength T, such that

$$\sigma_{n\max} = T \tag{3-12}$$

After the maximum tensile stress is reached, the normal stress is set to zero.

Due to the possible change in orientation during iteration, the shear stress is computed incrementally, defined as

$$\sigma_s = \{\sigma_s\}_{updated} + k_s \Delta u_s \tag{3-13}$$

Where, $\{\sigma_s\}_{\text{updated}}$ is the updated shear stress, k_s is the tangential stiffness, proportional to k_n and Δu_s is increment relative tangential displacement.

Uniformly distributed random Voronoi diagram is used as mesh to discretize the concerning domain of targeted rocks. With this kind of mesh, k_n and k_s can be determined by macro elastic parameters, i.e. elastic modulus E and poison ratio v, such that according to Chapter 2.

$$r = k_s / k_n = 4.025\nu^4 - 6.087\nu^3 + 6.022\ \nu^2 - 3.966\nu + 1 \tag{3-14}$$

$$E / E_0 = -0.6291r^4 + 1.617r^3 - 1.678r^2 + 1.174r + 0.5162 \tag{3-15}$$

$$k_n = \frac{E_0}{h_1 + h_2} \tag{3-16}$$

$$k_s = r \cdot k_n \tag{3-17}$$

Where, r and E_0 are intermediate variables, h_1 and h_2 denote the distances from the centroids of two neighboring blocks to their connecting interface.

To simulate the fracturing and damage process of geo materials, a modified Mohr-Coulomb model is adopted (Figure 3.2). The maximum allowable shear stress is computed by the normal stress σ_n, the cohesion C, the critical normal stress $\sigma_{n\ \text{critical}}$, the local frictional angle φ_1 and the local residual frictional angle φ_2. The critical normal stress $\sigma_{n\text{critical}}$ is defined to limit the frictional strengthening effects. Before rupture, the maximum shear stress is computed by

$$\sigma_{s\max} = \sigma_n \tan\varphi_1 + C, \sigma_n > \sigma_{n\,\text{critical}} \tag{3-18}$$

$$\sigma_{s\max} = \sigma_n \tan\varphi_1 + C, \sigma_n \le \sigma_{n\,\text{critical}} \tag{3-19}$$

Shear rupture takes place when $\sigma_s > \sigma_{s\max}$, then the interaction becomes purely frictional, with a maximum shear force defined by

$$\sigma_{s\max} = \sigma_n \tan\varphi_2 , \sigma_n > \sigma_{n\,\text{critical}} \tag{3-20}$$

$$\sigma_{s\max} = \sigma_n \tan\varphi_2 , \sigma_n \le \sigma_{n\,\text{critical}} \tag{3-21}$$

In the modified rigid body spring method, structural planes and virtual cracks are treated in the same manner, with an only difference in micro parameters.

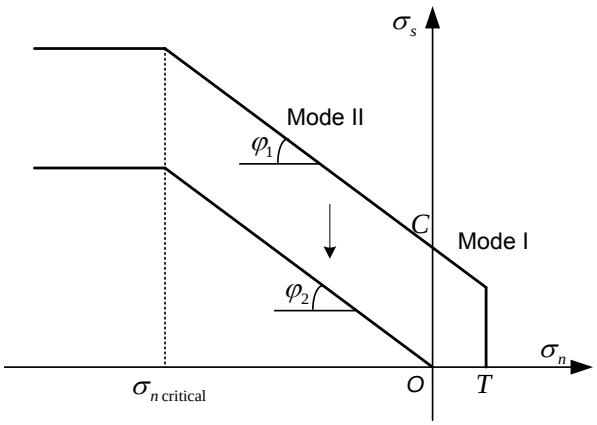

Figure 3.2 Fracturing criterion for the modified RBSM

3.4 Voronoi Diagram generation with embedded structures

It is taken two main steps to generate Voronoi diagram mesh: point insertion and tessellation. Each step is described in detail as follows.

3.4.1 Point insertion

To get a uniformly distributed Voronoi diagram, the process of point insertion is based on the concept of point saturation. Point saturation is achieved by maintaining distance between neighboring points under a minimum admissible distance $l_{\min}$. To explicitly model bedding planes, a multistep insertion procedure is adopted, and the whole process is illustrated in Figure 3.4. Here, we define a segment of boundaries or bedding planes as a Segment, and an interaction between a boundary and a bedding plane as a Vertex.

1）Insertion of points to define Vertexes (Figure 3.4(b)).

Suppose there is a Vertex V connected by four Segments, Figure 3.3. To define this Vertex, firstly, find out the minimum angle between two neighboring Segments, the value of which is assumed to be 2β. Then, draw auxiliary lines which have an angle of β with respect to each segment. After that, draw a circle with a radius of $0.5l_{\min}$around vertex *V*. Inserting points at intersections between the circle and all auxiliary lines around vertex *V* and vertex *V* is defined, as is illustrated in Figure 3.3.

2）Insertion of points to define Segments (fig.4(c)).

Pairs of points are symmetrically inserted to define each Segments. Distances between each neighboring points on the same side of pre-existing line are larger than l_{min}.

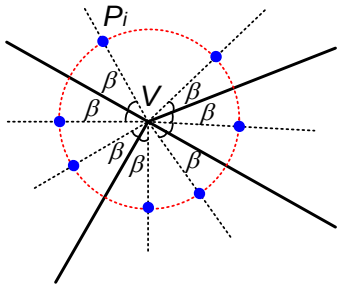

Figure 3.3 Points to define Vertex V

3）Insertion of points to the whole domain (fig.4(d)).

With the constraint of l_{min}, points are sequentially inserted to saturate the whole domain.

In step 2) and 3), points are inserted sequentially in a random manner. This process is very computational demanding when the total number of points is in great amount (like 100000) due to the constraint of l_{min}. To effectively reduce computational cost, a partitioned domain search is used.

3.4.2 Tessellation

There are various methods available for Voronoi tessellation with a set of points. In the present study, a sweep line algorithm proposed by Steven Fortune [14] is used. With points inserted in the previous step, Voronoi diagram is generated, as shown in Figure 3.4(e). After removing line segments outside the boundaries, the mesh we need for simulation is obtained (Figure 3.4 (f)).

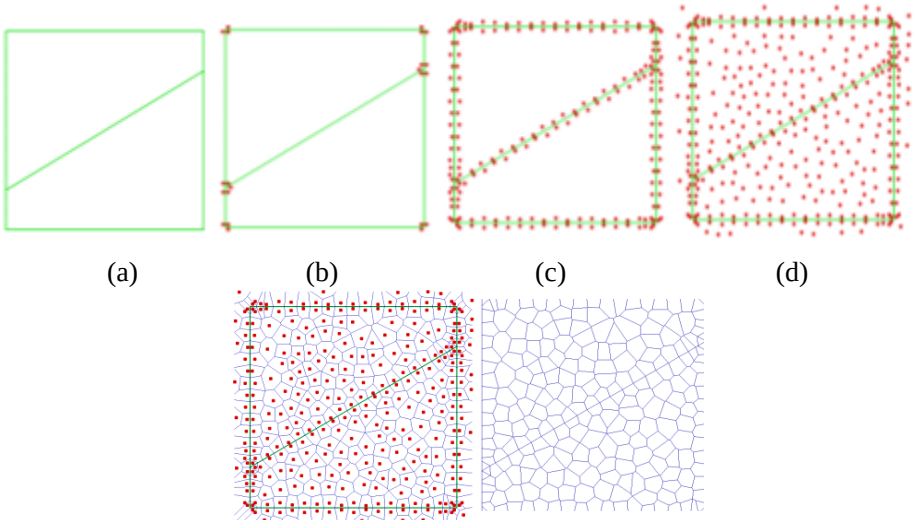

Figure 3.4 Mesh generation sequence

3.5 Effects of stiffness of bedding planes on macro elastic parameters

Firstly, a parameter α is proposed to represent the orientation of bedding planes with respect to loading direction. With the technique presented above, seven different numerical specimens are generated with different orientations of bedding plane, respectively 0，15，30，45，60，75 and 90 (Figure 3.5). The specimen size is 100mm×50mm, the spacing of bedding planes is 12.5mm and $l_{\min}$=0.8mm.

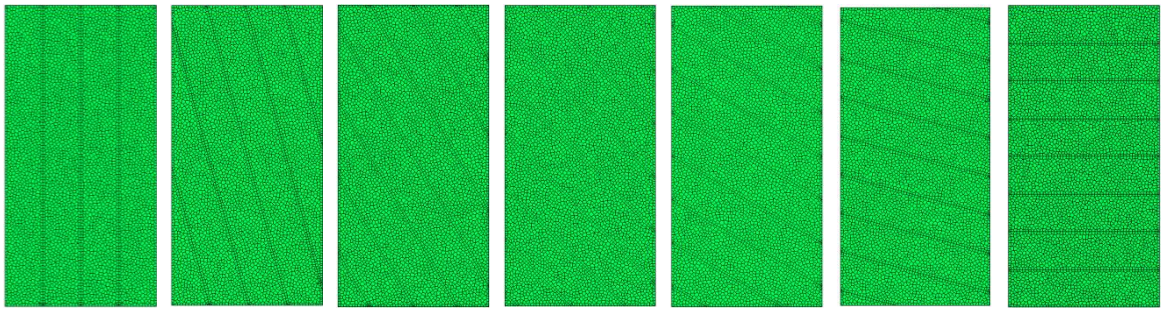

(1) $\alpha=0^\circ$ (2) $\alpha=15^\circ$ (3) $\alpha=30^\circ$ (4) $\alpha=45^\circ$ (5) $\alpha=60^\circ$ (6) $\alpha=75^\circ$ (7) $\alpha=90^\circ$

Figure 3.5 Numerical specimens for various orientations with respect to loading direction

Suppose that stiffnesses of bedding plane k_{np} and k_{sp} are proportional to stiffnesses of matrix k_n and k_s, such that

$$k_{np} = r \cdot k_n \tag{3-22}$$

$$k_{sp} = r \cdot k_s \tag{3-23}$$

In which, r is a ratio coefficient. Seven different values are applied for r, i.e. 0.001，0.01，0.1，1，10，100 and 1000. Elastic uniaxial compression simulations are conducted on the seven specimens with seven different r. Macro elastic modulus obtained for each specimen with different r are shown in Figure 3.6, and macro poison ratios obtained are shown in Figure 3.7.

From Figure 3.6, it can be seen that, r has almost no impact on the macro elastic modulus of the specimen with α=0° . But with the increase of α, change in r induces greater variance in the value of macro elastic modulus. Overall, increase of r results in increase of macro elastic modulus. However, there is a limit in increase of macro elastic modulus. When r reaches a specific value, no increase will be observed in macro elastic modulus with increase of r, as illustrated in Figure 3.6(a) that for r =100 and r =1000, lines almost coincide with each other.

From Figure 3.7, it can be seen that, r has almost no impact on the poison ratio of the specimen with α=0° . For specimens with α=15° , 30° , 45° ,and 60° , the increase of r results in the increase of poison ratio. For specimens with α=75° And 90° , however, the trend is

opposite, increase of *r* results in decrease of poison ratio. Similar to Figure 3.6, there exists a limit in change of poison ratio when *r* getting larger to a specific value. Almost no variance is observed for lines with *r* =10, *r* =100 and *r* =1000 shown in Figure 3.7(a).

Results above show that stiffness of bedding planes has obvious impacts on macro elastic parameters. Significance of such effects depends on the orientation of bedding planes with respect to the loading direction. Anisotropy of macro elastic parameters is observed for different value of *r*. It should be pointed out that, when *r*=1, that means stiffness of bedding planes are equal to which of matrix, there is still obvious anisotropy in both macro elastic modulus and poison ratio. In such case, anisotropy in macro elastic parameters is purely induced by bedding planes.

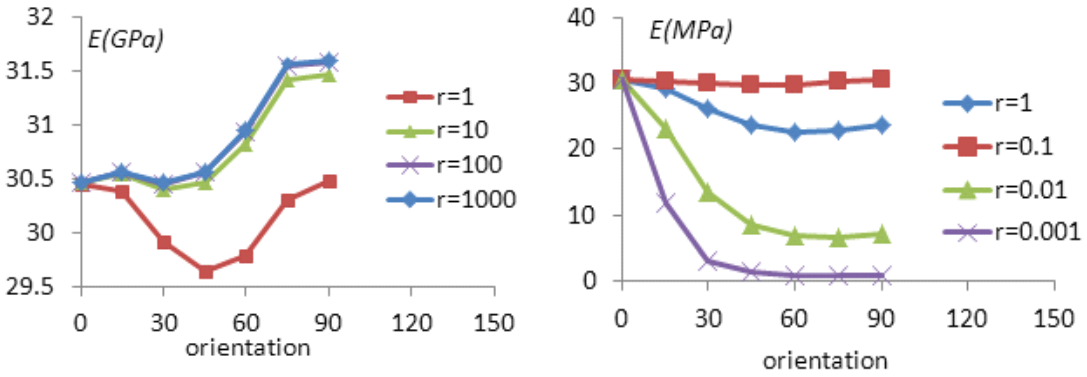

（a）*r*=1, 10 , 100, 1000　　(b) *r*= 0.001, 0.01, 0.1, 1

Figure 3.6　Macro elastic modulus obtained with different stiffness of structure plane

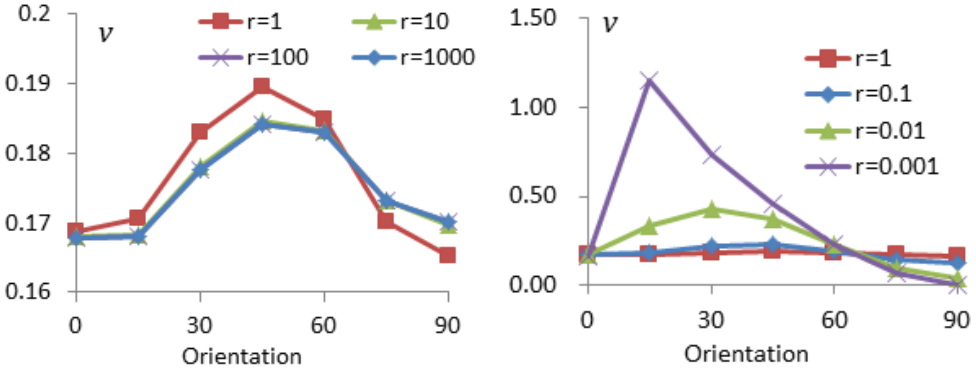

(a) *r*=1, 10 ,100, 1000　　(b) *r*=0.001, 0.01, 0.1, 1

Figure 3.7　Poisson ratio obtained with different stiffness of structure plane

3.6 Effects of fracturing coefficients of bedding planes on macro failure strength

3.6.1 Effects of cohesion

To investigate effects of cohesion of bedding planes on macro failure strength, a series of uniaxial compression experiments are conducted on specimens in Figure 3.5. Input parameters are listed in Table 3.1. C is cohesion of matrix, set as 14MPa. Four different cohesions of bedding planes C_f are used, respectively 1.0C, 0.75C, 0.5 C and 0.25C. Apart from cohesion C_f, other strength parameters of bedding plane are equal to which of matrix. Stiffnesses of bedding plane are set as a half of which of matrix. Results of this series of experiments are shown in Figure 3.8.

From Figure 3.8, it can be seen that for specimens with α=15° , 30° and 45° ,and 60° , decrease of C_f results in obvious drop of uniaxial compression strength; For α=0° , 75° and 90° , it seems that C_f has no influence on UCS; For α=60° , decrease of from 1.0C to 0.5C has no obvious impact on UCS, but when drops to 0.25 C, an abrupt fall in UCS is observed. It is also shown that anisotropy in UCS is increased with decrease of C_f. When C_f =1.0 C, there is still anisotropy in UCS, indicating that anisotropy in UCS can be purely induced by orientations of bedding planes with respect to compression direction.

Table 3.1 Input parameters for simulations to investigate effects of cohesion of bedding planes on uniaxial strength

	E	v	tan. φ_1 .	tan φ_2	C	T	$\sigma_{n\,\text{critical}}$
Matrix	30GPa	0.18	0.5	0.5	14MPa	4.2MPa	80MPa
Bedding plane	-	-	0.5	0.5	r×14MPa	4.2MPa	80MPa

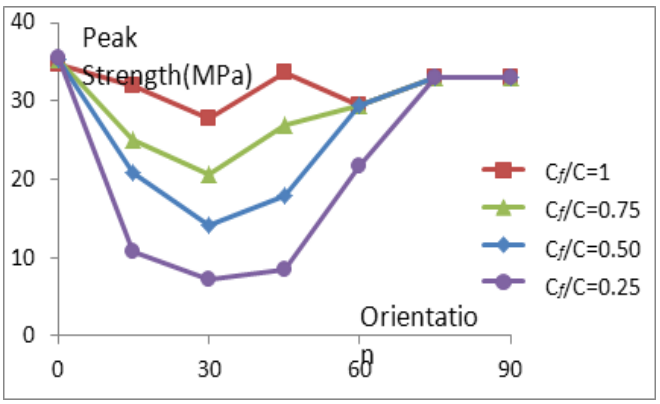

Figure 3.8 Influences of cohesion of bedding plane on uniaxial strength

3.6.2 Effects of internal frictional angle

To investigate effects of internal frictional angle of bedding planes on macro uniaxial compression strength, a series of uniaxial compression experiments are conducted on specimens in Figure 3.5. Input parameters are listed in Table 3.2. *f* is a parameter equals $\tan\varphi_1$ and $\tan\varphi_2$. Four different *f* for bedding planes are used, respectively 0.0, 0.2, 0.5 and 0.8. Cohesion of bedding planes *C* is set as 7Mpa, a half of 14MPa, cohesion of matrix. Stiffness of bedding plane is set as a half of which of matrix. Results of this series of experiments are shown in Figure 3.9.

Table 3.2 Input parameters for simulations to investigate effects of internal frictional angle of bedding planes on uniaxial strength

	E	*v*	$\tan\varphi_1$	$\tan\varphi_2$	*C*	*T*	$\sigma_{n\,\text{critical}}$
Matrix	30GPa	0.18	0.5	0.5	14MPa	4.2MPa	80MPa
Bedding plane	-	-	0.0, 0.2, 0.5, 0.8	$\tan\varphi_1$	7MPa	4.2MPa	80MPa

From Figure 3.9, it can be seen that for specimens with α=30° and 45°, decrease of *f* of bedding plane results in obvious drop of uniaxial compression strength; For α=0° and 90°, it seems that changing *f* has no influence on UCS; For, decrease of *f* from 0.8 to 0.5*C* has no obvious impact on UCS but obvious drops in UCS are observed when *f* drops to 0.2 and 0.0. For α=75°, decrease of *f* from 0.8 to 0.5 and 0.2 has no obvious impact on UCS but an obvious drop in UCS is observed when *f* drops to 0.2 and 0.0.

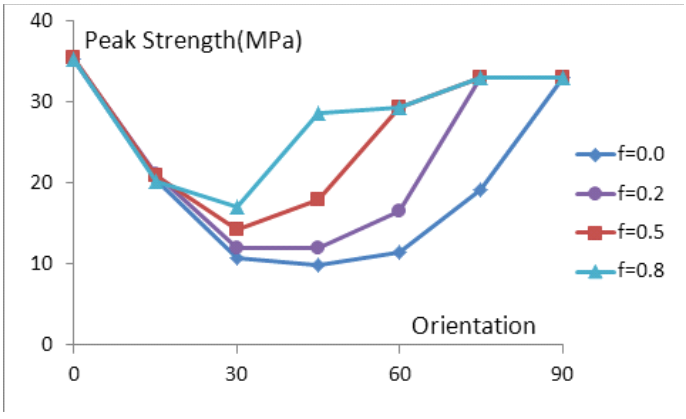

Figure 3.9 Influences of internal frictional angle of bedding plane on uniaxial strength

3.7 Effects of density of bedding planes

To investigate effects of the density of bedding planes, three different spacing's are adopted for arrangements of bedding planes, respectively 25mm, 12.5mm and 6.25mm. Here, these three arrangements are interpreted as coarse, medium and dense. With each spacing, 7 specimens are generated for different orientations, i.e. 0°, 15°, 30°, 45°, 60°, 75°, 90°. Shown in Figure 3.10 are uniaxial compressive strengths of all specimens calculated by the proposed model, with parameters listed in Table 3.1 and r=0.5. It can be noted that little variance of UCS for each orientation can be observed among different densities of bedding planes.

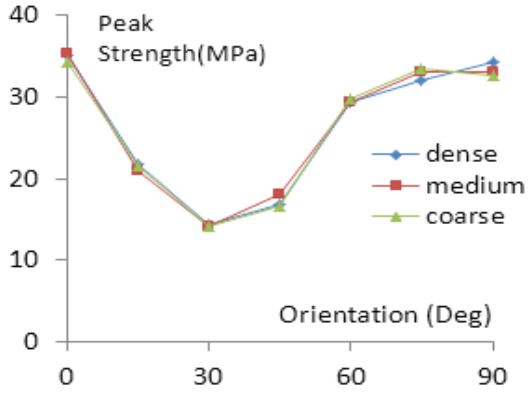

Figure 3.10 Comparison of UCS for different orientations with different density of bedding planes

3.8 Effects of mesh size on macro stress-strain curves

To investigate mesh effects on macro stress stain curve, five different meshes with different element size are generated for $\alpha = 45^\circ$, the total element number of which are respectively 2242, 5101, 5101, 10140, 20739 and 52297. Specimen size are all 100mm×50mm. Here, a parameter N is used to represent total number of elements. With parameters listed in Table 3.1 and making r be 0.5, simulations under uniaxial compressive condition are carried out.

Uniaxial strengths for all specimens analyzed by the proposed model are similar to each other, listed in Table 3.3. Stress-strain curves for each mesh are interpreted in Figure 3.11. It can be seen that each curve is similar to each other with a tolerable difference. Therefore, it can be noted that mesh size has little significance on macro stress-strain relationships.

Table 3.3 Peak strengths for specimens with different number of elements

N	2242	5101	10140	20739	52297
UCS (MPa)	17.49	17.98	17.79	17.57	17.96

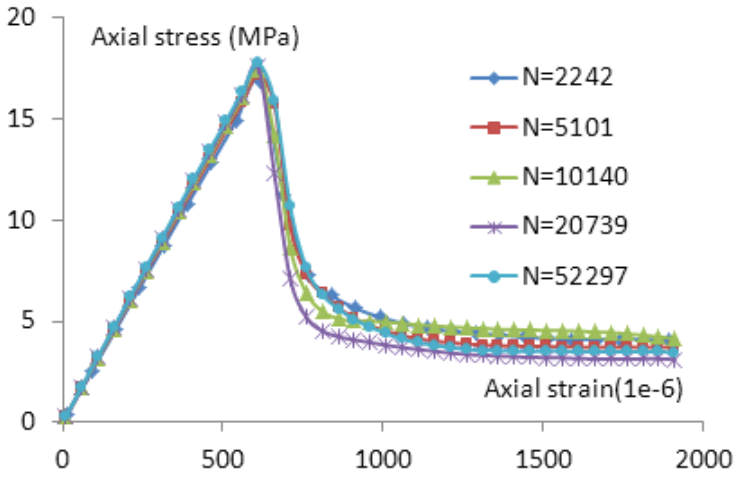

Figure 3.11 Comparison of stress strain curves among specimens with different element size

3.9 Comparison with rock experiments

In order to illustrate the performance of the proposed model and verify its capability to simulate behaviors of real rock, numerical simulation is conducted against experimental results on a shale taken from the Tournemire site in the Massif Central, France. Due to the existence of a set of bedding planes, the rock exhibits an inherent transverse isotropy. A comprehensive experiment has been done at Laboratoire de Mecanique de Lille, results of which have been reported by Niandou[5].

The calibration procedure for micro parameters of both rock matrix and bedding planes was carried out as follow:

Determination of matrix parameters in order to match the desired compression strength of $\alpha = 0^{\circ}$ under different confining pressures. Since parameters of bedding planes have negligible effects on compressive strength of α=0° , as illustrated by above analysis, when the match is achieved, matrix parameters is determined.

Determination of parameters of bedding planes in order to match the desired compression strength of α=30° under different confining pressures. When the match is achieved, a group of parameters for bedding planes is determined. In experiments, the minimum compression strength is often obtained at α=30° . Thus; these parameters can maintain the anisotropy degree in compressive strength in a reasonable extent.

The micro parameters determined by the calibration procedure are listed in Table 3.4 for both rock matrix and bedding planes. Comparison of peak strength for α=0° and α=30° between simulation and experiment under different confining pressures are respectively illustrated in Figure 3.12and Figure 3.13.

Table 3.4 Micro parameters for simulation of Tournemire shale

	$\tan\varphi_1$	$\tan\varphi_2$	C	T	$\sigma_{n\,\text{critical}}$
Matrix	0.6	0.1	15MPa	0.15MPa	60MPa
Bedding Plane	0.7	0.7	8MPa	0.08MPa	45MPa

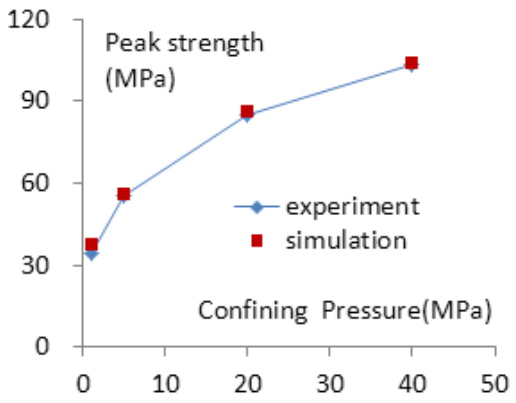

Figure 3.12 Simulation of Peak strength for against experiments under various confining pressures

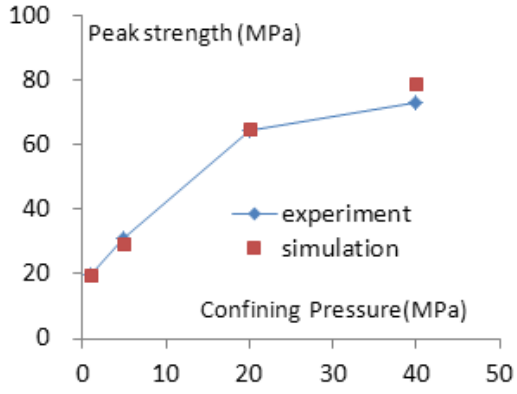

Figure 3.13 Simulation of Peak strength for against experiments under various confining pressures

3.9.1 Peak strength under various confining pressures

With these micro parameters, a comprehensive numerical investigation has been carried out considering confining pressures ranging from 1MPa and 40MPa in accordance with the experiment. Results are shown in Figure 3.14. In general, the maximum strength is obtained at α=0° . Strength for α=90° is almost the same as α=0° . With the increase of confining pressure, strength for all specimens increases, which is consistent with experimental evidence. The minimum strength occurs at α=30° under confining pressure 1MPa and 5MPa, at α=40° under 20MPa and 40Mpa. The transition of the minimum strength from α=30° To α=45° with the increase of confining pressure from 5MPa to 20MPa is also observed in the experiment. In general, simulation results are in a reasonable agreement with experimental data, demonstrating the validity of the proposed model in predicting strength of real anisotropic rocks.

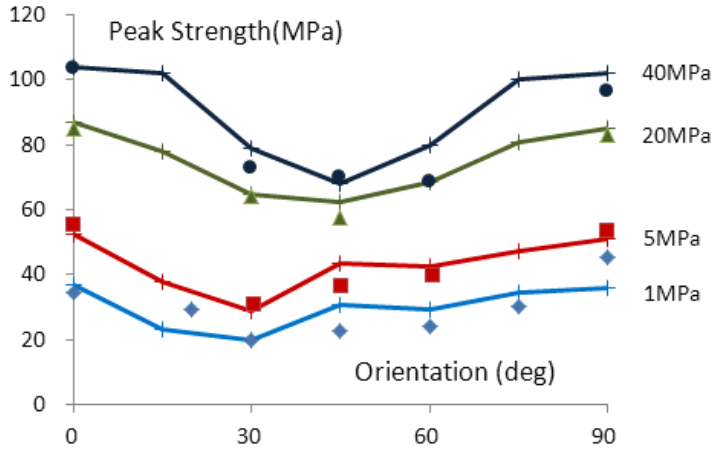

Figure 3.14 Comparison of peak strength of various orientations between simulation and experiments under different confining pressures (lines represent simulation results, dots represent experiment results (after Niandou[5]))

3.9.2 Failure mode

Failure mode is related to orientation and confining pressures. Here, we take α=15° and α=60° as representatives of low orientation and high orientation to illustrate their relationships.

Illustrated in Figure 3.15 are graphs of displacement vector for α=15° after peak strength under various confining pressures, respectively 1MPa, 20MPa and 40MPa. It is shown that, with increase of confining pressure, displacement field tends to be more homogenous and effects of bedding planes gets weaker and weaker. Figure 3.16 illustrates distribution of micro cracks for α=15° After peak strength. In 1MPa, failure is a result of a combination mechanism of tension and shear. With increase of confining pressure from 1MPa to 20MPa, micro cracks tends to be concentrated along bedding planes, failure is mainly caused by shear along these planes. When the confining pressure reaches 40MPa, a shear band with an angle of about 55° with respect to the orientation of bedding plane occurs as the main failure mechanism, totally different from which for 5MPa and 40Mpa. This transition can be used to explain the trend of change in peak strength for α=15° in Figure 3.14. When the confining pressure is low (1MPa), peak strength of α=15° is close to the peak strength of α=30°, which is the minimum strength. As confining pressure goes up, peak strength of α=15° gets closer and closer to the peak strength of α=0°, which is the maximum strength.

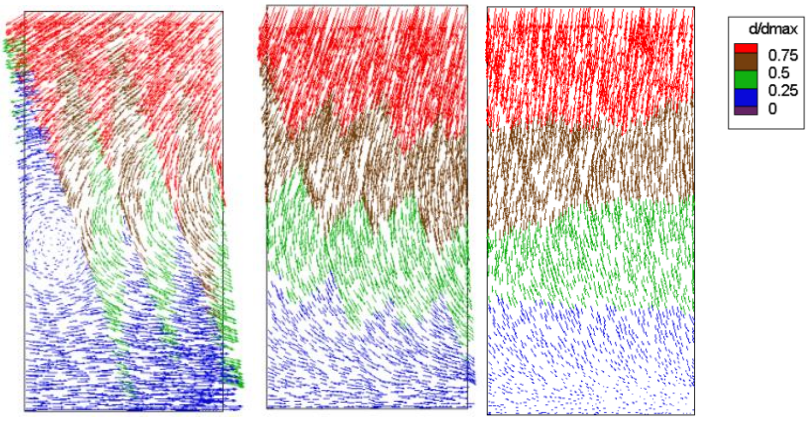

(a) 1MPa (b)20MPa (c)40MPa

Figure 3.15 Graph of displacement vector for α=15° after peak strength under various confining pressures

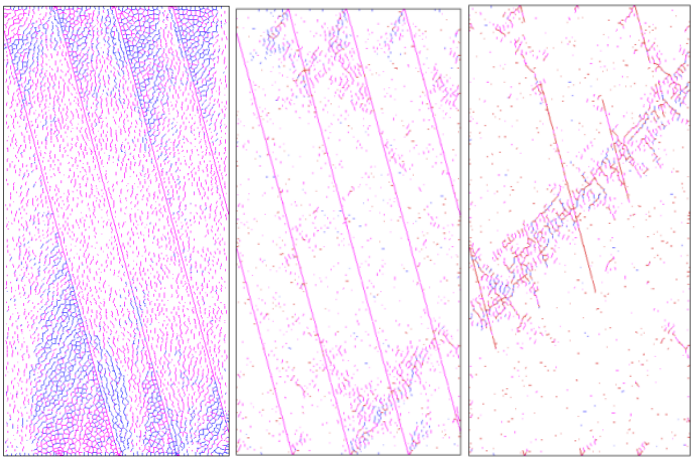

(a) 1MPa (b)20MPa (c)40MPa

Figure 3.16 Micro cracks distribution after peak strength for . α=15° . under different confining pressures (blue line represents tensile crack, purple line represents shear crack before $\sigma_{nctitical}$, red line represents shear crack after$\sigma_{nctitical}$)

Illustrated in Figure 3.17, Figure 3.18 and Figure 3.19 are respectively graphs of displacement vector, deformed specimen and micro cracks distribution for α=60° after peak strength under various confining pressures, respectively 1MPa and 20MPa. It can be seen in these figures that there is also an obvious transition in main failure mechanism with increase of confining pressure. When confining pressure is equal to 1 MPa, the failure is controlled by coalescence of tensile cracks. And when confining pressure is equal to 20Mpa, the main failure mechanism turns to be shear along the bedding planes. This transition can also be used to explain the trend of change in peak strength for α=60° in Figure 3.14. With increase of confining pressure, peak strength for α=60° gets much closer to the minimum peak strength.

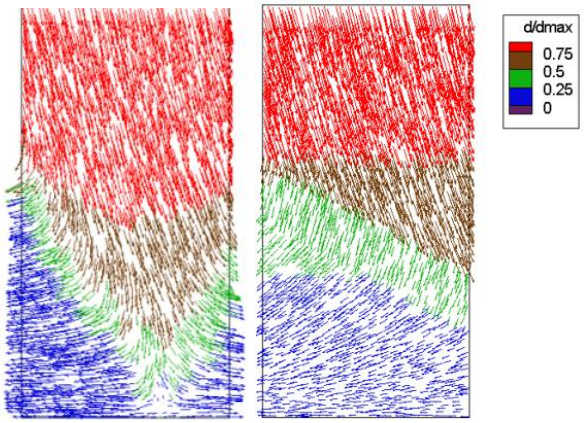

(a) 1MPa (b)20MPa

Figure 3.17 Graph of displacement vector for α=60° after peak strength under confining pressures 1MPa and 20MPa

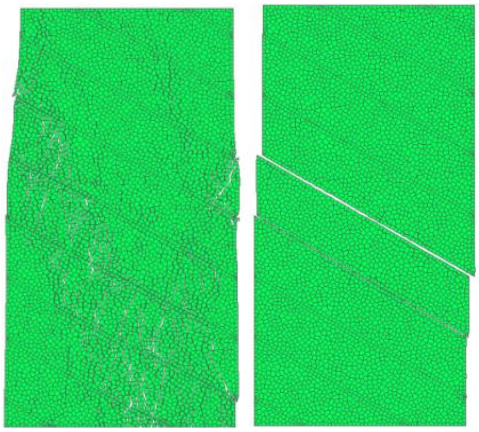

(a) 1MPa (b)20MPa

Figure 3.18 Deformed Specimen for α=60° after peak strength under confining pressures 1MPa and 20MPa (displacement in y direction×10)

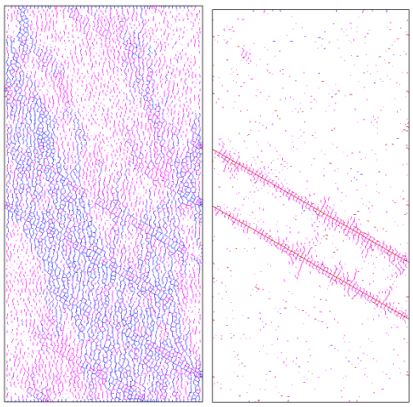

(a) 1MPa (b) 20MPa

Figure 3.19 Micro cracks distribution after peak strength for α=60° under different confining pressures (blue line represents tensile crack, purple line represents shear crack before $\sigma_{nctitical}$, red line represents shear crack after $\sigma_{nctitical}$)

3.10 Conclusion

In this research, a modified rigid body spring method is put forth for the modeling of inherently anisotropic sedimentary rocks. The main focus is on anisotropy of strength with regards to the orientation of bedding planes to loading direction.

Effects of micro parameters of bedding planes on characteristics of macro deformation and failure strength are investigated. Some conclusions can be drawn,

(1) Stiffness of bedding planes has different impacts on macro elastic modulus and poison ratio with different orientations. For α=0°, such impact is ignorable. And, there seems to be upper limits for such influence: when stiffness gets greater to some value, no obvious change in macro elastic parameters can be observed. For orientations apart from $\alpha = 0^{\circ}$, in general, decrease of stiffness of bedding planes results in decrease in macro elastic modulus and the higher the orientation is, the greater the impact is. For α=15°, 30°, 45°,and 60°, decrease of stiffness of bedding planes results in decrease of poison ratio. For specimens with 75° and 90°, however, decrease of stiffness of bedding planes results in increase of poison ratio.

(2) Cohesion and internal frictional angle of bedding planes both have significant effects on macro failure strength. Though such effects are dependent on orientations, in general, reduce of them results in drop of failure strength. Mesh size and density of bedding planes have little influence on macro uniaxial compressive strength with various orientations.

A two-step micro parameter calibration procedure is implemented against experiment results reported by Niandou [5]. With these calibrated parameters, numerical simulation is carried out with different confining pressures, results of which agree well with experiments on real rocks, demonstrating the capability of the proposed model in predicting behaviors of real anisotropic rocks.

Failure mechanisms for some orientations under different confining pressure are discussed. It is found that for lower orientation, with increase of confining pressure, the main failure mechanism tends to transit from shear along bedding planes to shear across bedding planes; for higher high orientation, with increase of confining pressure, the main failure mechanism tends to transit from tension failure to shear along bedding planes. This transition also reflects on the change of peak strength with change of confining pressures.

Reference

[1] F. A. Donath, “Experimental Study of Shear Failure in Anisotropic Rocks”, Geological Society of America Bulletin, vol 72, no 6, pp 985–989, Jan 1961.

[2] P. B. Attewell and M. R. Sandford, “Intrinsic shear strength of a brittle, anisotropic rock—I: Experimental and mechanical interpretation”, International Journal of Rock Mechanics and Mining Sciences & Geomechanics Abstracts, vol 11, no 11, pp 423–430, 1974.

[3] R. McLamore and K. E. Gray, “The Mechanical Behavior of Anisotropic Sedimentary Rocks”, J. Manuf. Sci. Eng., vol 89, no 1, pp 62–73, 1967.

[4] E. Hoek, “Strength of jointed rock masses”, Géotechnique, vol 33, no 3, pp 187–223, Jan 1983.

[5] H. Niandou, J. F. Shao, J. P. Henry, and D. Fourmaintraux, “Laboratory investigation of the mechanical behaviour of Tournemire shale”, pp 3–16, Jan 1997.

[6] Y. M. Tien, M. C. Kuo, and C. H. Juang, “An experimental investigation of the failure mechanism of simulated transversely isotropic rocks”, International Journal of Rock Mechanics and Mining Sciences, vol 43, no 8, pp 1163–1181, 2006.

[7] J. C. Jaeger, “Shear failure of anisotropic rocks”, Geological Magazine, vol 97, no 1, pp 65–72, Jan 1960.

[8] G. Duveau and J. F. Shao, “A modified single plane of weakness theory for the failure of highly stratified rocks”, International Journal of Rock Mechanics and Mining Sciences, vol 35, no 6, pp 807–813, 1998.

[9] Hoek E, Brown ET. Underground excavation in rock. London: Institution of Mining and Metallurgy, 1980. p. 157–62.

[10] R. Hill, The Mathematical Theory of Plasticity. Oxford University Press, 1998.

[11] Cazacu, N. D. Cristescu, and J. F. Shao, “A new failure criterion for transversely isotropic rocks”, International Journal of Rock Mechanics and Mining Sciences, vol 35, no 4–5, p 421, 1998.

[12] R. Nova, “The failure of transversely isotropic rocks in triaxial compression”, International Journal of Rock Mechanics and Mining Sciences & Geomechanics Abstracts, vol 17, no 6, pp 325–332, 1980.

[13] Y. M. Tien and M. C. Kuo, “A failure criterion for transversely isotropic rocks”, International Journal of Rock Mechanics and Mining Sciences, vol 38, no 3, pp 399–412, 2001.

[14] Steven Fortune (1987). A sweepline algorithm for Voronoi diagrams. Algorithmica. 2(1-4): 153-174

Chapter 4 Modeling permeability variation in the process of rock failure

4.1 Introduction

The intrinsic permeability of rocks is an important parameter in many fields of geotechnical engineering, such as deep mining, petroleum exploitation and geological disposal of nuclear waste. Many experimental researches have shown that the intrinsic permeability evolution is highly related to the damage growth of the rocks, and the intrinsic permeability can increase by several orders of magnitude at peak strength[1,2,3].

However, only a few numerical models have been developed to study the coupling effects between permeability evolution and micro crack growth. Some of them are mentioned here. Oda et al [1] used the crack tensor concept to describe the permeability change in rock failure based on the transient pulse tests on the Inada granite. Souley et al.[4]extended the anisotropic damage model developed by Homand [5] has been to account for changes in permeability induced by micro crack growth. Shao et al.[6] proposed a phenomenological anisotropic model for brittle rocks, and used the cubic law to compute crack permeability, which is further developed by Zhou et al.[7] and Jiang et al.[8]. Pereira et al.[9] modeled the influence of deformation and damage on the permeability and retention properties of cracked porous media based on the Pore Size Distribution. These models, however, are mostly macroscopic models based a homogenization or statistics concept. They cannot exactly describe the changes of micro structure which might control the permeability and other aspects of macroscopic material behaviors.

The objective of the present study is to develop a meso-scopic numerical method to model the coupling process of permeability variation and damage growth of rock masses under deviatoric stress. In this method, the process of micro crack initiation, propagation and coalescence is explicitly simulated. The basic motivation of this work is not only to improve our understanding of the fundamental mechanisms and physical processes that control the change of permeability, but also to provide a numerical model for quantitatively reproducing the curves observed in the laboratory. In the literature, very few numerical models have been developed for this coupling process in the mesoscopic level. Bruno [10] proposed a micromechanical model based on discrete element method and network model, but only in a qualitative way. Tang et al. [11] presented a coupled model of flow, stress and

damage in rock failure, but in this model the flow of fluid is governed by Biot's consolidation theory, effects of micro crack on permeability is not explicitly considered. Mansouriet al. [12] computed the permeability of a cemented granular material based on the discrete element model and the lattice Boltzmann method, but the focus of this work is on the cementation process, no stress effects is considered.

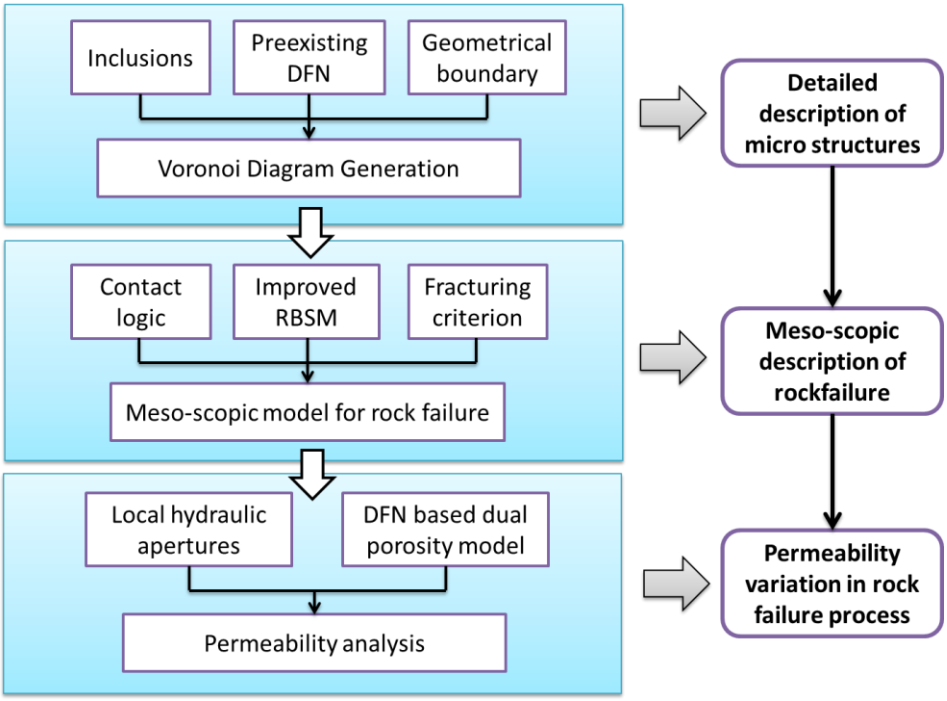

Figure 4.1 The technical roadmap for the mesoscopic model to study the permeability variation during the process of rock failure

In this study, we combine a meso-scopic mechanical model developed by Yao et al.[13]and the discrete fracture model proposed by Yao et al.[14] and Jiang et al[15]to describe the hydro-mechanical coupling processes of rock masses under biaxial loading. The technical roadmap of this work is illustrated in Figure 4.1. Firstly, we use the randomly and uniformly distributed Voronoi diagram to represent detailed information of the micro structures and rock matrix of the rock masses, in which pre-existing joint networkand internal boundaries are explicitly embedded. Secondly, with a relatively simple contact logic and local fracturing criterion, the improved rigid body spring method is employed to model the process of micro crack initiation, propagation and coalescence and other mechanical behaviors of rock masses. Finally, a simple relationship between the hydraulic aperture of interface and the local fracturing status is established and a discrete fracture network based dual porosity model is developed and applied to characterize the conductivity of the rock specimen.

4.2 The DFN based dual porosity model

4.2.1 Equivalent fracture network

In flow simulation, the randomly and uniformly distributed Voronoi diagram is treated as a kind of discrete fracture network. In order to develop a numerical model to describe the permeability evolution of rock matrix based on this concept, the relationship between the hydraulic apertures of interfaces between the macro permeability must be firstly established to make the permeability of fracture network be equivalent to the rock matrix. In order to find out this relationship, and to investigate its mesh dependency at the same time, seven groups of numerical studies are conducted by varying the total number of elements as 1010, 2053, 5235, 10566, 21329, 53584 and 107854. Each group contains 10 specimens with different element arrangement. The size of each specimen is 1m by 1m. The hydraulic aperture of every interface segment b_i is set to be 1×10^{-6}m, the transmissivity of interface is calculated by the following equation according to the cubic law,

$$T_i = \frac{g b_i^3}{12v} \tag{4-1}$$

The hydraulic boundary is shown in Figure 4.2 and the hydraulic gradient is set as 1m/m. Statistics of results of each group are listed in Table 4.1, in which, Q_h and Q_v are respectively the total horizontal flow rate and vertical flow rate; μ is the mean value, C_v is the coefficient of variation, which is defined as the ratio of the standard deviation σ to the mean. Little variance is observed between vertical flow rate and horizontal flow rate in each group, indicating that permeability isotropy is produced by this kind of network. The variation of effective conductivity among the same group is very small, not more than 0.32%, which means that mesh arrangement has little impacts on macro results. And there is a trend that as number of elements increases the variation declines.

The relationship between average total flow rate Q_0, which can be expressed as,

$$Q_0 = average(Q_h) = average(Q_v) \tag{4-2}$$

and the element number of each group N is illustrated in Figure 4.3. It can be observed that there is a linear relationship between $\sqrt{N}$ and the dimensionless parameter Q_0/T_i, which can be expressed as,

$$Q_0 / T_i = 0.9473\sqrt{N} - 1.0448 \tag{4-3}$$

Since it is an isotropic fracture network, the macro conductivity of the fracture network C_0 is expressed as

$$C_0 = C_h = Q_h / h = C_v = Q_v / w \tag{4-4}$$

in which, C_h and C_v are respectively macro horizontal and vertical conductivity, h and w are respectively width and height of the fracture network, which are both 1m here.

With equation (4-1), (4-2) and (4-4), if N and C_0 are known a priori, the effective hydraulic aperture b can be calculated. It is worth noting here that N is the element number in a unit square. If in a square, the size of which is $h\,\mathrm{m}\times w\,\mathrm{m}$, the total number is N_0, then the needed N in equation (4-2) is expressed as

$$N = N_0 / (h \times w) \tag{4-5}$$

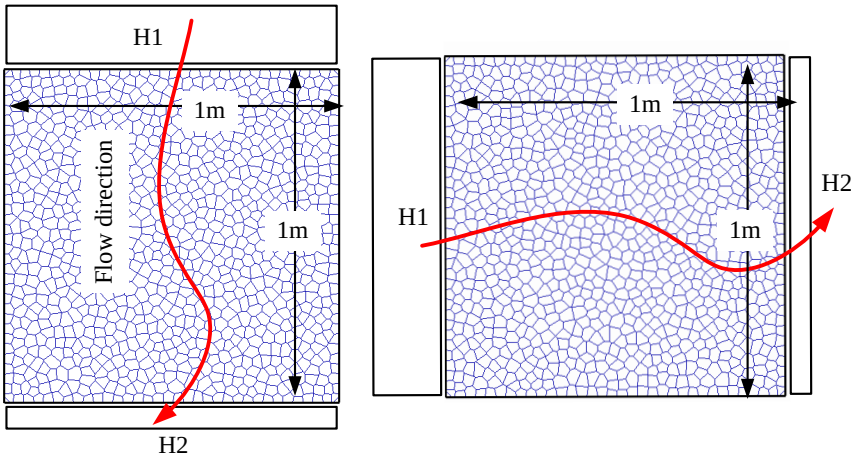

(a) Vertical flow (b) horizontal flow

Figure 4.2 Hydraulic boundary for computation of vertical and horizontal conductivity

Table 4.1 Statistics of conductivity for all groups of numerical tests

	Q_h		Q_v	
	μ (m^2/s)	C_v (%)	μ (m^2/s)	C_v (%)
1010	2.42E-11	0.31	2.42E-11	0.32
2053	3.49E-11	0.27	3.49E-11	0.20
5235	5.63E-11	0.10	5.62E-11	0.09
10566	8.03E-11	0.07	8.03E-11	0.09
21329	1.14E-10	0.06	1.14E-10	0.06
53584	1.82E-10	0.03	1.82E-10	0.03
107854	2.58E-10	0.04	2.58E-10	0.04

In this table, and respectively the macro horizontal transmissivity and vertical transmissivity; μ is the mean value, C_v is the coefficient of variation, which is defined as the ratio of the standard deviation σ to the mean. μ.

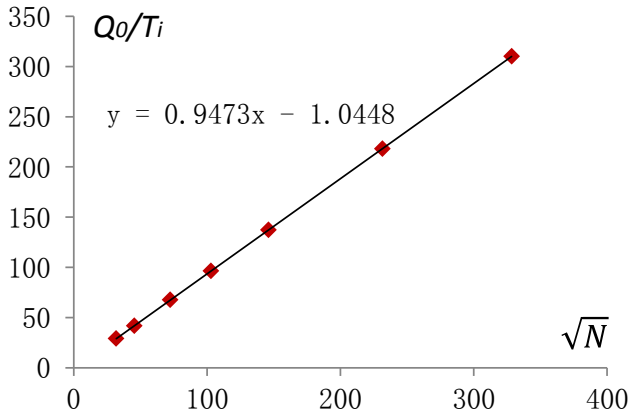

Figure 4.3 The relationship between Q_0 / T_i and $\sqrt{N}$

4.2.2 A pragmatic solution for the ill conditioned global equations for flow simulation

As mentioned in previous chapters, joints can be embedded in the Voronoi Diagram in an explicit manner. In the DFN based dual porosity model, seepage behaviors of rock matrix are represented by flow in interfaces. This way, the two dimensional problem is simplified into a one dimensional problem, and flow in both rock matrix and pre-existing joints is treated in the same way based on the discrete fracture network model. There is a problem to be solved to apply this DFN based dual porosity model into practice: since the transmissivity of joints are different from which of interfaces usually in several orders of magnitude, the global equilibrium equations for flow simulation may be very ill-conditioned, and the PCG method sometimes cannot give the correct solution. The global equilibrium equation for flow simulation can be expressed as

$$[K]\{\phi\} = \{Q\} \tag{4-6}$$

For simplicity, no details of this equation will be mentioned here, readers can refer to. In the PCG method, there needs an initialization of $\{\phi\}$, which is supposed to be $\{\phi\}^0$ here. $\{\phi\}^0$ is usually chosen according to the boundary condition by experience. The solution of the equation can be very sensitive to $\{\phi\}^0$ when $[K]$ is very ill-conditioned.

There is an example, the geometry of which is shown in Figure 4.4, in which 5 joints are randomly located. The effective conductivity of the rock matrix C_r is 1e-14m/s, and N =13527, so the equivalent hydraulic aperture of interface b_i is 4.79e-8m computed by equation (4-1) (4-3) and (4-4). The hydraulic aperture of joints b_f is 1000 times that of interface as 4.79e-5m. In this case, the difference between elements in $[K]$ can be 9 orders of magnitude. Here, the equilibrium between the flow rate on the upstream boundary Q_u and the flow rate on the downstream boundary Q_d is used as an indicator to check the

quality of the solution. Using $\{H_1\}$ (in which, all elements are equal to the water head of the upstream boundary) as the initialization of $\{\phi\}$, and with the PCG method, we get that Q_u =8.953e-14m^2/s and Q_d =9.071e-14 m^2/s. The solution is totally wrong since the flow rate on the downstream boundary Q_d should not be positive.

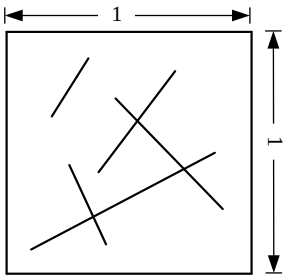

Figure 4.4 The geometry of the case study for pragmatic solution of equation

In the light of the sensitivity of the solution to $\{\phi\}^0$, a pragmatic procedure is proposed to improve the solution with PCG. We say it as pragmatic since we don't know if it is rigorous in mathematics. The basic idea is to find an initialization $\{\phi\}^0$ to approach gradually to the real solution.

①Suppose the total step of this procedure is S, in the first step,

$$\{\phi\}_1^0 = \{H_1\} \tag{4-7}$$

②In the *s*th step, assume that $b_f^{'} = \left(s/S\right)^{1/3} b_f$, using this $b_f^{'}$ as the hydraulic aperture of the joints to assemble the global matrix $[D]_s$,

$$\left.\begin{array}{c} b_i \\ b_f^{'} = \left(s/S\right)^{1/3} b_f \end{array}\right\} \Rightarrow \left[D\right]_s \tag{4-8}$$

③With the solution in the step *s*-1 as the initialization in the step *s*,

$$\{\phi\}_s^0 = \{\phi\}_{s-1} \tag{4-9}$$

Solving the following equation,

$$\left[D\right]_s \{\phi\}_s = \{B\} \tag{4-10}$$

In the last step *S*, we can get the final solution of the equation (4-6).

Using the proposed procedure, the results of the example in this section are illustrated in Table 4.2 with different *S*. In this table, Q_{32}=1.946e-14 m/s, is the flow rate computed when $b_f = 32b_i$. We can see that the gap between Q_u and Q_d generally becomes narrower as S increases, indicating that this procedure can effectively solve this kind of ill conditioned linear equations.

Table 4.2 Solution of this example with the proposed procedure using different

S	Q_u (e-14m/s)	Q_d (e-14m/s)	Error=$\lvert(Q_u+Q_d)/Q_{32}\rvert$ (%)
1	8.953	9.071	926.21
10	2.463	-1.138	68.09
100	2.204	-1.545	33.86
1000	1.739	-2.276	27.60
10000	1.901	-2.021	6.17
1000000	1.943	-1.956	0.67

4.3 Validity of the DFN based dual porosity model

In the proposed DFN based dual porosity model, the interfaces representing the intact rock are treated in the same manner as pre-existing joints, only with different hydraulic apertures or local transmissivity. A simple example reported in Lough et al.[16] is used here to validate the ability of the DFN based dual porosity model in predicting the effective conductivity of a jointed rock. This example is a block in the shape of a unit cube containing a single joint. The joint is centered at the cube, oriented at an angle α relative to the x-direction and with a length of 0.6 units. Depicted in Figure 4.5(a) is the geometry of Lough's example, in Figure 4.5(b) is which used in this study. The simplification of the problem from 3- dimensional to 2-dimensional is reasonable since the main aim of this example is to study effects of the pre-existing joint on conductivity in *x* and *y* direction, and they are not affected by the conductivity in *z* direction. The local transmissivity of interface T_i is set as 1 unit and the transmissivity of the joint T_f is set as 2×10^6 in the same units. Voronoi mesh for this case is illustrated in Figure 4.6.

We know that effective conductivity will depend on the joint orientation. If when $\alpha=0$, the macro horizontal and vertical conductivity are C_{h0} and C_{v0}, then in a general orientation α, the effective conductivity can be written as,

$$C_h = C_{h0}\cos^2\alpha + C_{v0}\sin^2\alpha \tag{4-11}$$

$$C_v = C_{h0}\sin^2\alpha + C_{v0}\cos^2\alpha \tag{4-12}$$

Assuming that $C_{v0}=1.000$, the relative value of C_{h0} computed by the proposed model is 1.347, with a minor error of 0.12% compared to Lough's result 1.3486. Comparison between the computed and predicted relative effective conductivity with different oriented joint is illustrated in Figure 4.7. In this figure, it can be seen that the numerical results agree well with the theoretically predicted counterparts from equation (4-5).

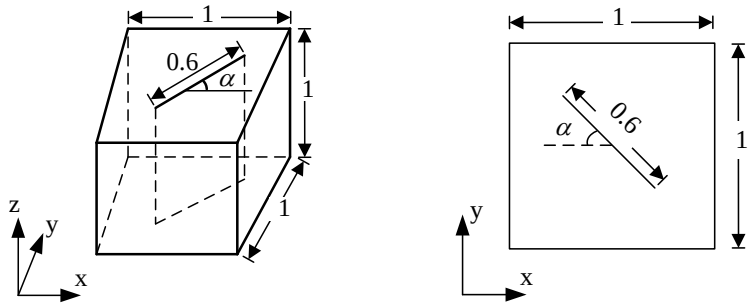

(a)The geometry of Lough's example (b) Geometry used in this study

Figure 4.5 The geometry used in the example with a general orientation of the joint

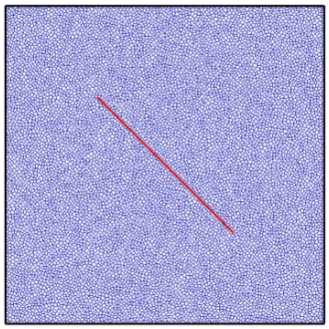

Figure 4.6 Voronoi mesh for the sample with a joint orientated at 45 degree

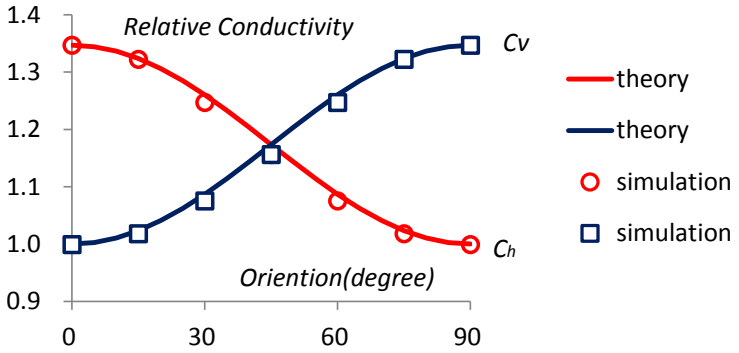

Figure 4.7 Illustration of the theoretical prediction and numerical results of effective conductivity for different joint orientation

4.4 Effects of joint geometries on the effective conductivity

In this section, the impacts of some other geometric parameters of the pre-existing joints apart from orientation, i.e. hydraulic aperture, length and connection with each other, on the effective conductivity of rock mass are investigated.

4.4.1 Hydraulic apertures of pre-existing joints

A group of tests are conducted by varying the hydraulic aperture of the pre-existing joint b_f to investigate its effect on effective horizontal conductivity of rock mass C_h. The

geometry of this example is the same as Figure 4.5(b), with $\alpha = 0^{\circ}$. The hydraulic boundary is using the one in Figure 4.2(b). N is set as 11458, and the effective conductivity of rock matrix C_r 1e-12m/s. By equation (4-1) and (4-2), the hydraulic aperture of interface b_i is computed to be 2.287e-7m. Numerical results are shown in Figure 4.8 by varying b_f from b_i to $512b_i$. It can be seen from this figure that C_h / C_r increases as b_f increases until $b_f = 32b_i$, after that C_h / C_r keeps constant, and increase of b_f has no impacts on C_h / C_r any more. The threshold of the increase of C_h / C_r is 1.347 in this case.

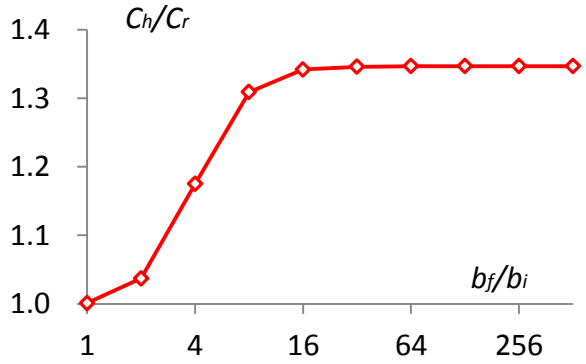

Figure 4.8 Effective conductivity computed by different hydraulic aperture of joint

4.4.2 Length

Two different cases are used to study the length effects on the effective conductivity. In the first case, the joint is located in the center of the rock block (Figure 4.9(a)); in the second case, the joint is connected to the upstream boundary (Figure 4.9(b)). The hydraulic boundary is using the one in Figure 4.2(b). N is set as 11458, and the effective conductivity of rock matrix C_r 1e-12m/s. The computed ratios between effective horizontal conductivity C_h and C_r are illustrated in Figure 4.10 by varying the joint length l from 0.1 to 0.9. As can be seen from this figure , C_h / C_r increases as the length gets larger, and C_h / C_r for the connected one are overall larger than which of the one with a centered joint When $l = 1.0$, which means that a percolation condition is satisfied, T_h / T_r rises abruptly to 834, about 300 times which when $l = 0.9$.

In some constitutive models based on the homogenization procedure [6, 8], there is a simple assumption that the local pressure gradient is equal to the macroscopic one. According to the present study, this assumption seems to be debatable. The contour graphs of water head for l =0.1, 0.5 and 0.9 are shown in Figure 4.11. It can be computed that, the local pressure gradient of the joint are respectively 1.08e-4m/m, 3.03e-4m/m and 1.64e-3m/m, which are all much smaller than the macroscopic gradient 1m/m. And there

seems to be a trend that the shorter the joint is, the smaller the gradient is. As a result, the models which adopt this assumption may greatly exaggerate the contribution of the isolated joints to the macro permeability.

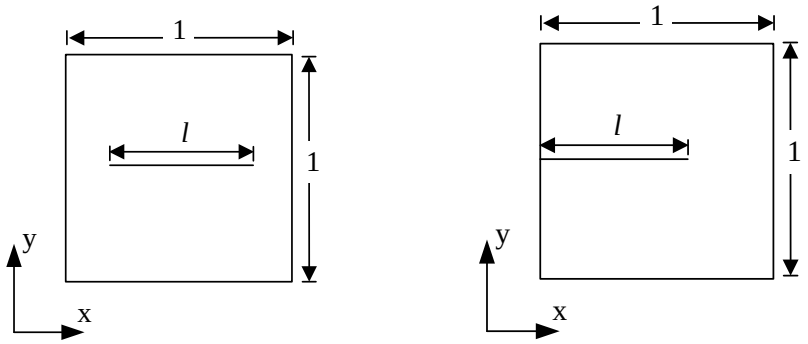

(a) joint located at center (b) joint connected to the upstream boundary

Figure 4.9 Geometry for study of length effects

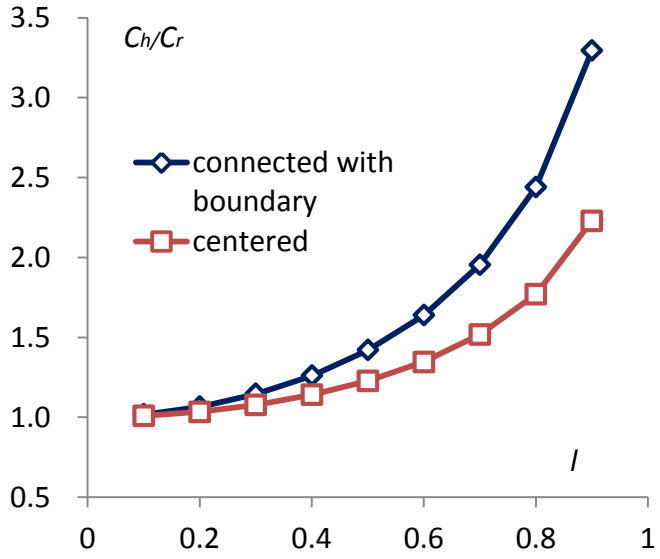

Figure 4.10 Effective conductivity computed with different joint length

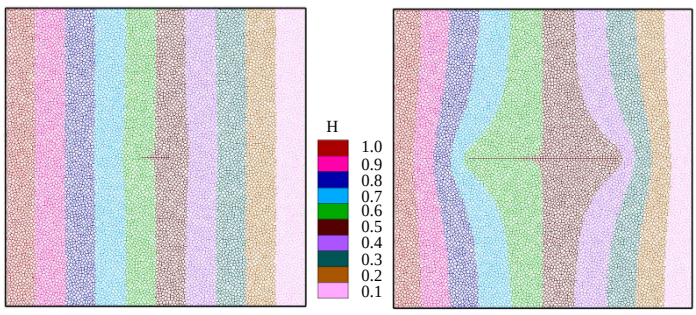

(a) *l*=0.1 (b) *l*=0.5

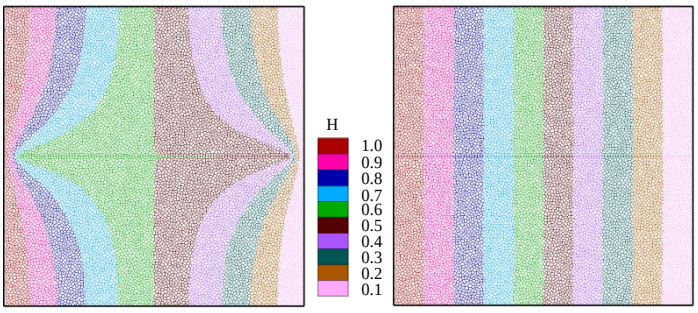

(c) l=0.9 (d) l=1

Figure 4.11 Contours of water head with different value of l

4.4.3 Intersection between multi joints

Intersections of multi joints may result in more complex flow behaviors. A simple example containing two joints is employed to study its effects, which is shown in Figure 4.12. Two joints respectively extend in the horizontal and the vertical direction. They are both 0.4 in length and perpendicular to each other. The horizontal joint is positioned in the center. A parameter is used to define their intersection position. The combined effects of these two joints are analyzed by varying r from 0 to 0.4.

The computed effective horizontal conductivities with different values of r is shown in Figure 4.13. As can be seen from this figure, with the increase of r, C_h first goes down before r reaches 0.2 -- the middle of the horizontal joint; then goes up until r reaches the end. When $r=0$ and $r=0.4$, C_h gets to the maximum value as 1.23; and when $r=0.2$, C_h gets to the minimum value as 1.14, in such a case, the vertical has no impact on the effective conductivity.

In Figure 4.7, it can be learned that the isolated vertical joint cannot cause increase in C_h. However, as we can see in Figure 4.13, through an intersection with the horizontal joint, it can make great contribution to the increase of C_h, and the effects depends on the intersection position.

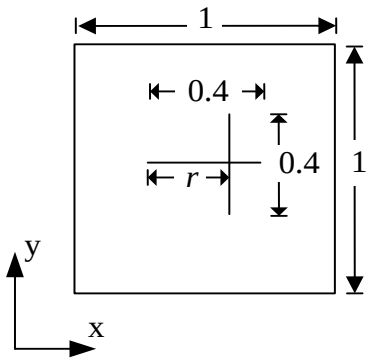

Figure 4.12 Geometry for study of intersection effects

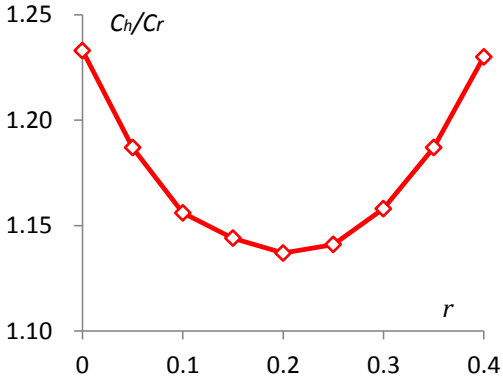

Figure 4.13 Effects of the intersection position on the effective horizontal conductivity

4.5 The conductivity variation in the process of rock masses

4.5.1 Conductivity variation in the failure process of an intact rock specimen

In this section, a specimen shown in Figure 4.14 is used to study the permeability variation during the process of rock failure. The size of this specimen is 0.05*m* ×0.10*m*, and the total number of elements is 13236. Assuming that the conductivity of this rock specimen is 1e-14*m/s*, i.e. C_r = 1e-14*m/s*, according to equation (4-1), (4-2) and (4-4), the hydraulic aperture of the interfaces is computed to be1.983e-8m. With this value of interface, the effective vertical conductivity of this specimen is computed to be 9.94e-15*m/s*, which is approximately equal to 1e-14*m/s*. The influence of local failure on the hydraulic aperture of interface is simply considered as follows: once a failure event is detected on an interface, either tensile failure or shearing failure, the hydraulic aperture of which is set to be 100 times of the original aperture, i.e. 1.983e-6*m* in this case.

The mechanical parameters for this specimen are listed in Table 4.3. Using these parameters, the stress-strain relationships of the rock specimen under various confining pressures are calculated, which are illustrated in Figure 4.15. In this figure, it can be observed that the failure strength goes up with the increase of the confining pressure. And there is an obvious transition from brittle to ductile as the confining pressure rises up from 0MPa to 40MPa,which is qualitatively in accordance with the previous experimental evidences [17]. The failure patterns under different confining pressures are depicted in Figure 4.17(a) - Figure 4.20(a).

Shown in Figure 4.16 are relationships between the relative axial conductivity C/C_r, the deviatoric stress $\sigma_1-\sigma_3$ and the principal strain ε_1 under various confining pressures. Abrupt increase in conductivity is observed after peak strength for every different confining pressure. And the increase can be five orders of magnitude. It can also be noted that the strain and stress threshold for onset of conductivity increase is depending on confining pressure, which is correlated with the fracturing criterion. Illustrated in figure 4.17(b) - 4.20(b) are flow rate distribution of rock specimen respectively at ε_1=1700, 1797, 2095 and 3689, where sudden conductivity jumps are observed respectively under the confining pressure of 0MPa, 10MPa, 20MPa and 40MPa. Main channels for water flow are clearly depicted, indicating that the connectivity of micro cracks are the main mechanisms of conductivity acceleration.

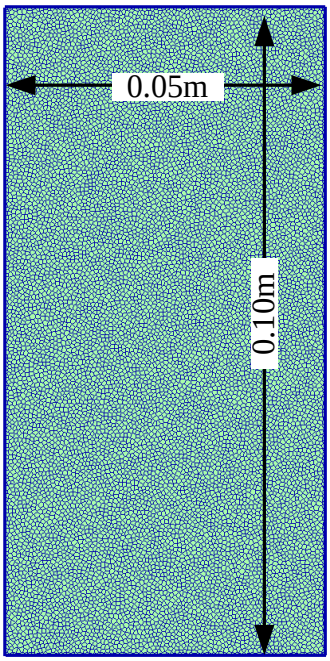

Figure 4.14 Rock specimen for case study in which 13236 elements are included

Table 4.3 Mechanical parameters for the intact rock

parameters	E	v	$\tan\varphi_1$	$\tan\varphi_2$	c	t	$\sigma_{n\,\text{critical}}$
Matrix	80GPa	0.18	0.5	0.1	30MPa	9MPa	60MPa

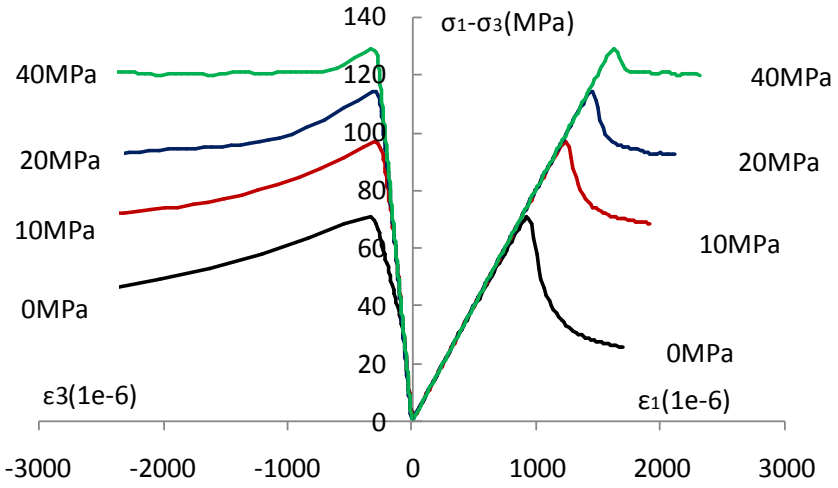

Figure 4.15 Stress - strain curves for the rock specimen under different confining pressures

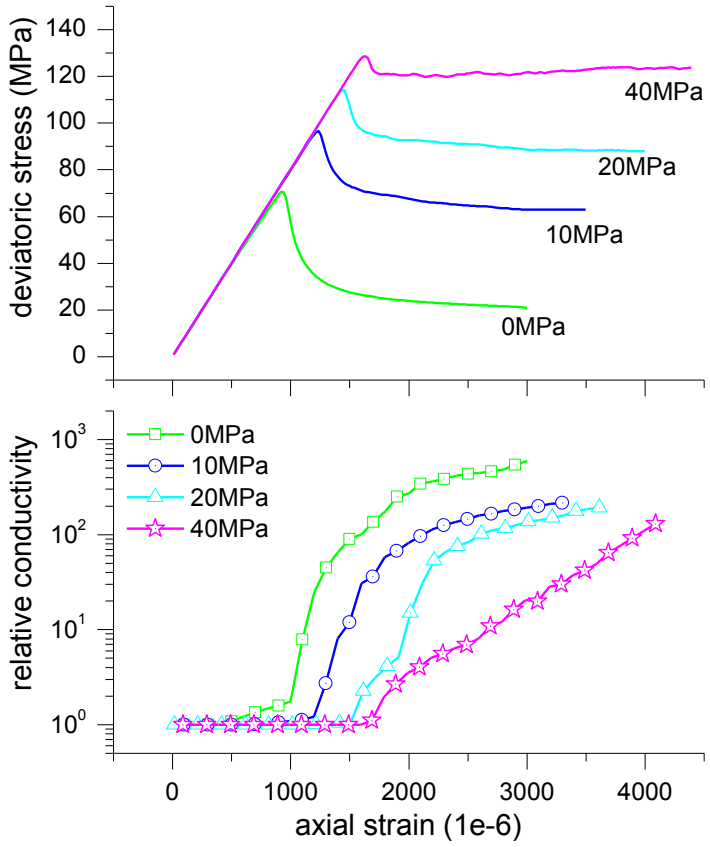

Figure 4.16 Axial conductivity variation of the intact rock as strain increases under different confining pressures

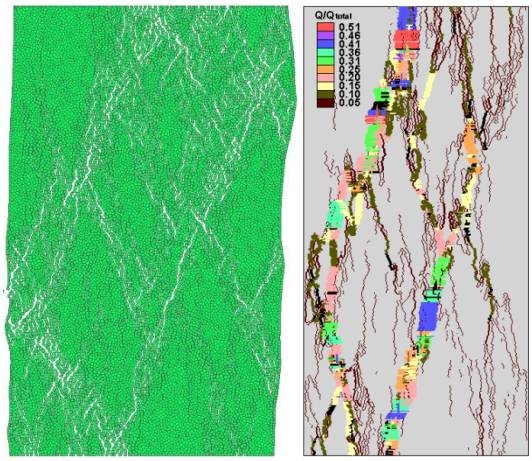

(a) Failure pattern (b) flow rate distribution

Figure 4.17 Failure modes and main flow paths of intact rock for σ3=0MPa

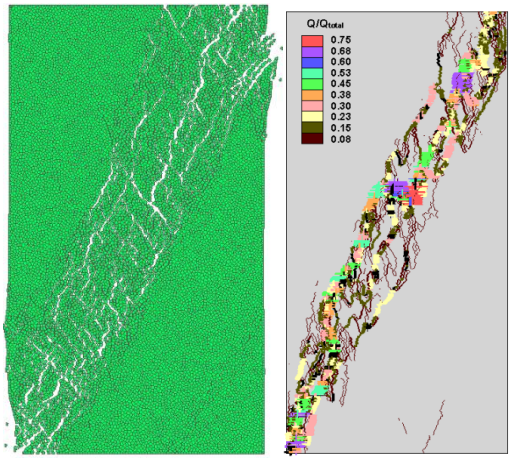

(a) Failure pattern (b) flow rate distribution

Figure 4.18 Failure modes and main flow paths of intact rock for σ3=10MPa

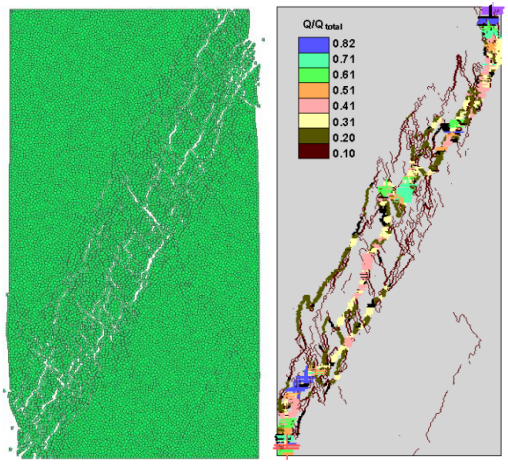

(a) Failure pattern (b) flow rate distribution

Figure 4.19 Failure modes and main flow paths of intact rock for σ3=20MPa

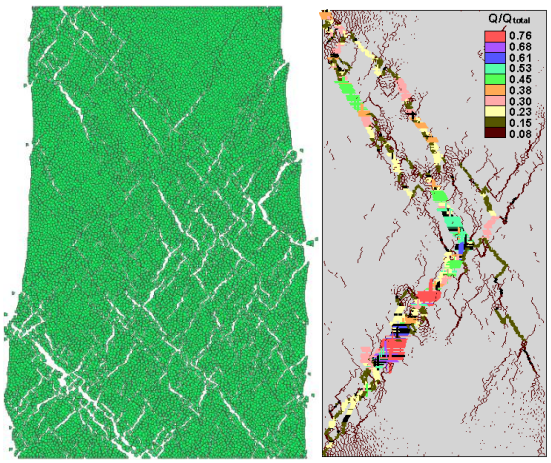

(a) Failure pattern (b) flow rate distribution

Figure 4.20 Failure modes and main flow paths of intact rock for σ3=40MPa

4.5.2 Conductivity variation in the failure process of the rock specimen with a pre-existing joint

In this section, a specimen shown in Figure 4.21 with a 45° oriented pre-existing joint is used to study the permeability variation during the process of rock failure. Apart from this center located joint, other parameters are the same as which of the rock specimen in section 4.5.1. The length of the joint is 1.414e-2*m*, and the hydraulic aperture is 1.983e-6*m*, which is 100 times that of the interface. Mechanical parameters of this joint are listed in Table 4.4. The effective vertical conductivity of this specimen is 1.02e-14 m/s, a little higher than C_r due to the existence of the pre-existing joint.

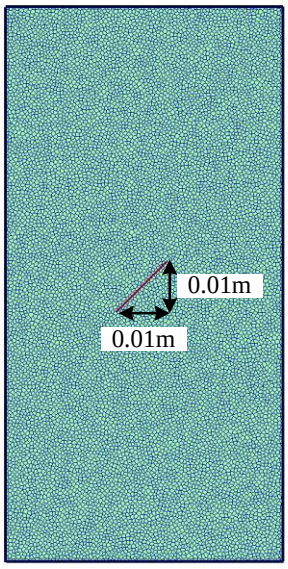

Figure 4.21 Mesh for the pre-cracked rock specimen with a pre-existing joint

Table 4.4 Mechanical parameters for the pre-existing joint

parameters	E	v	$\tan\varphi_1$	$\tan\varphi_2$	c	t	$\sigma_{n\,\text{critical}}$
Matrix	30GPa	0.18	0.3	0.3	5MPa	0.15MPa	20MPa

The stress-strain curves and the relative conductivity- strain curves for this pre-cracked specimen under different confining pressures are shown in Figure 4.22. It can be found that the stress-strain curves exhibit more ductile behaviors than that shown in figure Figure 4.15. And there is also dramatic rise in effective conductivity in the axial direction by about 5 orders of magnitude when confining pressure is 0MPa, 10MPa and 20MPa. When confining pressure increases to 40MPa, however, the abrupt conductivity rise is not attained, and the increase is only about 1 order of magnitude.

Comparison of deviatoric strength between the intact rock specimen and the pre-cracked rock specimen under different confining pressures is shown in Figure 4.23. In this figure, we can see that deviatoric strength of the pre-cracked rock is generally lower than which of the intact one, demonstrating the degradation effects of the pre-existing joint on rock strength.

Illustrated in Figure 4.24(a) - Figure 4.27(a) are failure patterns and flow rate distribution of the pre-cracked specimen after peak strength. Compared to the intact rock, the failure modes of the pre-cracked rock specimen are more consistent under different confining pressures. The final failure of the pre-cracked specimen occurred by the development of an “X” shaped black band [18]. Shown in Figure 4.24(b) - Figure 4.27(b) are the flow rate distributions under vertical hydraulic gradient. The main flow channels are in line with the main failure surface, demonstrating that crack propagation and coalescence are the controlling mechanisms in the increase of hydraulic conductivity.

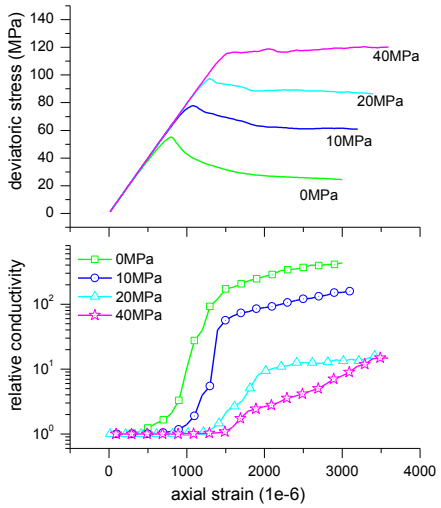

Figure 4.22 Axial conductivity variation of the pre-cracked rock as strain increases under different confining pressures

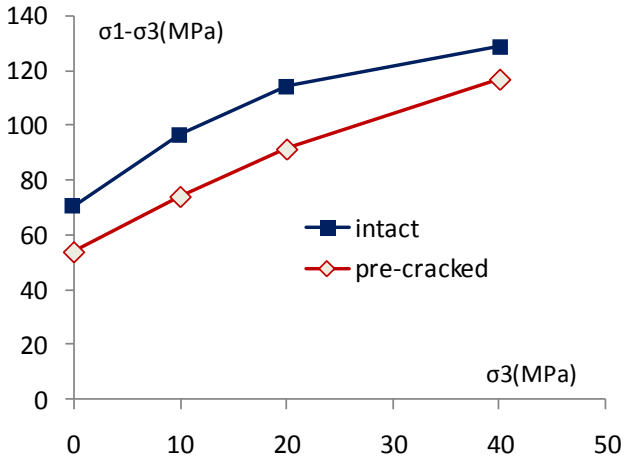

Figure 4.23 Comparison of deviatoric strength between the intact rock specimen and the pre-cracked rock specimen under different confining pressures

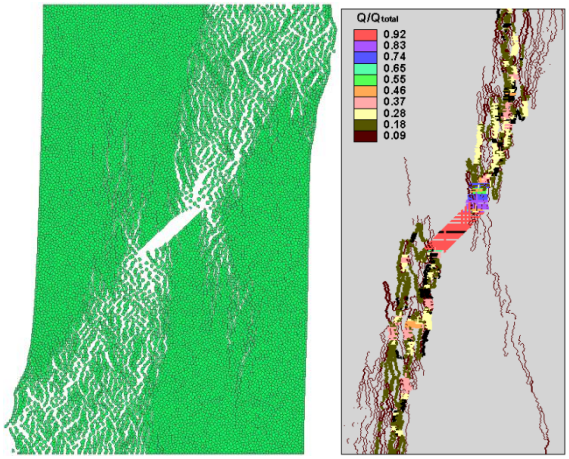

(a) Failure pattern (b) flow rate distribution

Figure 4.24 Failure modes and main flow paths of intact rock for σ_3=0MPa

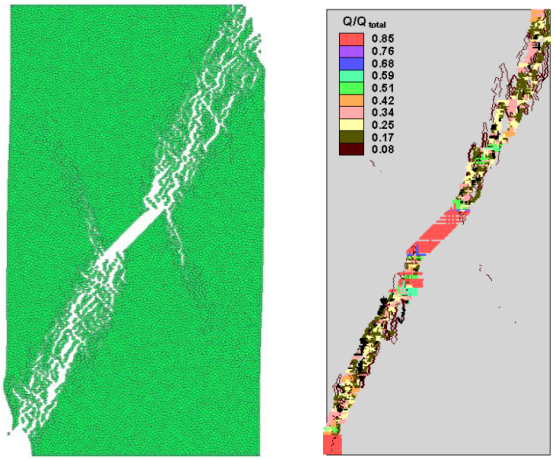

(a) Failure pattern (b) flow rate distribution

Figure 4.25 Failure modes and main flow paths of pre-cracked rock for σ_3=10MPa

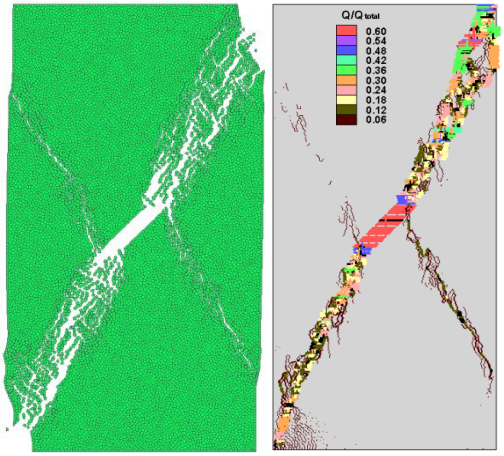

(a) Failure pattern (b) flow rate distribution

Figure 4.26 Failure modes and main flow paths of pre-cracked rock for σ3=20MPa

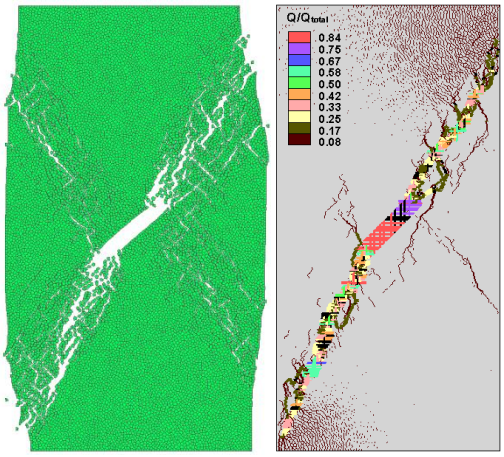

(a) Failure pattern (b) flow rate distribution

Figure 4.27 Failure modes and main flow paths of pre-cracked rock for σ3=40MPa

4.6 Conclusion

In this study, a DFN based dual porosity model is developed on the randomly and uniformly distributed Voronoi Diagram. The validity of this model is demonstrated by comparison with Lough's work and theoretical predictions. Effects of some geometrical parameters of the pre-existing joints on the effective conductivity of the rock mass are investigated, including orientation, aperture, length, inter-section relation of multi pre-existing joints. Some interesting phenomenon is observed:

(1) Isolated joints have a significant impact on the local flow field. The hydraulic gradient in these joints is much smaller than the macroscopic hydraulic gradient. Intersection of joints holds a meaning for the local flow field as well, the influence of which varies with the intersection position.

(2) The increase of effective conductivity induced by isolated joints or joint clusters is very limited. But when a percolation condition is attained, the increase can be several orders of magnitude.

This DFN based dual porosity model is combined with the improved RBSM to investigate the conductivity variation of rocks induced by damage growth. Numerical tests have been conducted on intact rock specimen and the pre-cracked rock under biaxial compression with different confining pressures. Typical failure modes and increase of conductivity by about 5 orders of magnitude are observed after peak strength. Some basic conclusions can be drawn as follows:

(1) Typical phases of the macro stress-strain curve are reproduced by the improved RBSM, such as linear elasticity, inelastic deformation, softening and residual phase. The shear bands leading to the final failure of rocks is also captured. And there is a clear transition from brittle to ductile as the confining pressure increases.

(2) The significant increase in conductivity is observed in the softening and residual phase, during which the global rock failure takes place and the percolation threshold is attained. The main failure surfaces constitute the main channels for water flow.

Reference

[1] M. Oda, T. Takemura, and T. Aoki, “Damage growth and permeability change in triaxial compression tests of Inada granite”, Mechanics of Materials, vol 34, no 6, pp 313–331, 2002.

[2] Schulze, T. Popp, and H. Kern, “Development of damage and permeability in deforming rock salt”, Engineering Geology, vol 61, no 2–3, pp 163–180, 2001.

[3] P. Bossart, P. M. Meier, A. Moeri, T. Trick, and J.-C. Mayor, “Geological and hydraulic characterisation of the excavation disturbed zone in the Opalinus Clay of the Mont Terri Rock Laboratory”, Engineering Geology, vol 66, no 1–2, pp 19–38, 2002.

[4] M. Souley, F. Homand, S. Pepa, and D. Hoxha, “Damage-induced permeability changes in granite: a case example at the URL in Canada”, International Journal of Rock Mechanics and Mining Sciences, vol 38, no 2, pp 297–310, 2001.

[5] F. Homand-Etienne, D. Hoxha, and J. F. Shao, “A continuum damage constitutive law for brittle rocks”, Computers and Geotechnics, vol 22, no 2, pp 135–151, 1998.

[6] J. F. Shao, H. Zhou, and K. T. Chau, “Coupling between anisotropic damage and permeability variation in brittle rocks”, International Journal for Numerical and Analytical Methods in Geomechanics, vol 29, no 12, pp 1231–1247, 2005.

[7] J. J. Zhou, J. F. Shao, and W. Y. Xu, “Coupled modeling of damage growth and permeability variation in brittle rocks”, Mechanics Research Communications, vol 33, no 4, pp 450–459, 2006.

[8] T. Jiang, J. F. Shao, W. Y. Xu, and C. B. Zhou, “Experimental investigation and micromechanical analysis of damage and permeability variation in brittle rocks”, International Journal of Rock Mechanics and Mining Sciences, vol 47, no 5, pp 703–713, 2010.

[9] J.-M. Pereira and C. Arson, “Retention and permeability properties of damaged porous rocks”, Computers and Geotechnics, vol 48, pp 272–282, 2013.

[10] M. S. Bruno, “Micromechanics of stress-induced permeability anisotropy and damage in sedimentary rock”, Mechanics of Materials, vol 18, no 1, pp 31–48, 1994.

[11] C. A. Tang, L. .Tham, P. K. . Lee, T. . Yang, and L. . Li, “Coupled analysis of flow, stress and damage (FSD) in rock failure”, International Journal of Rock Mechanics and Mining Sciences, vol 39, no 4, pp 477–489, 2002.

[12] M. Mansouri, J.-Y. Delenne, A. Seridi, and M. S. El Youssoufi, “Numerical model for the computation of permeability of a cemented granular material”, Powder Technology, vol 208, no 2, pp 532–536, 2011.

[13] Yao C., Jiang QH, Shao JF, Zhou CB. A mesoscopic numerical model for simulation of rock fracturing. Chinese Journal of Rock Mechanics and Engineering. 2013 (in press)

[14] Yao Chi, Jiang Qinghui, Ye Zuyang, Zhou Chuangbing. Initial flow method for unconfined seepage problems of fracture networks. Rock and Soil Mechanics, vol33, no 6, pp1896-1903, 2012.

[15] Q. Jiang, C. Yao, Z. Ye, and C. Zhou, “Seepage flow with free surface in fracture networks”, Water Resources Research, vol 49, no 1, pp 176–186, 2013.

[16] M. F. Lough, S. H. Lee, and J. Kamath, “An Efficient Boundary Integral Formulation for Flow Through Fractured Porous Media”, Journal of Computational Physics, vol 143, no 2, pp 462–483, 1998.

[17] J. D. Byerlee, “Brittle-ductile transition in rocks”, Journal of Geophysical Research, vol 73, no 14, pp 4741–4750, 1968.

[18] Chen, G., J. M. Kemeny, and SatyaHarpalani. "Fracture propagation and coalescence in marble plates with pre-cut notches under compression." Fracture and Jointed Rock Mass 14 (1992): 435-439.

Chapter 5 Seepage flow with free surface in two dimensional fracture networks

5.1 Introduction

The fractured rocks are complicated geological media that have undergone a long process of geological evolution. There are numerous discontinuities with various attitudes and different scales. Generally, the models used in the study of seepage behaviors through the fractured rocks may be divided into two categories: one is based on the equivalent continuum approaches [e.g., Snow, 1969; Duiguid and Lee, 1977; Streltsova, 1981; Long et al., 1982; Hsieh and Neuman, 1985; Oda, 1985, 1986; Jackson et al., 2000] and the other is based on the discrete fracture network representations [e.g., Wilson and Witherspoon, 1974; Schwartz et al., 1983; Long et al., 1985; Andersson and Dverstorp, 1987; Dershowitz and Einstein, 1987; Cacas et al., 1990; Jing et al, 2001; Baghbanan and Jing, 2007]. The equivalent continuum models generalize the fractured rocks as equivalent porous media and usually assume that the seepage flow of underground water through the fractured rocks follows the Darcy's law. At the present, the equivalent models are widely used to simulate groundwater flow through fractured rocks in the field of rock engineering. However, it is very difficult for the models to describe the heterogeneous spatial distribution of groundwater fluxes due to the discrete nature of the fractures. On the other hand, the discrete fracture network models take into account the geological and hydraulic characteristics of each fracture explicitly. The rock matrix is assumed to be impermeable, and groundwater only flows within connected fracture paths. In fact, since the permeability of intact rock is usually low compared with the fractures developed in the rocks, the seepage flow behavior through fractured rocks is mainly controlled by the fractures. In essence, the models based on discrete fracture network can describe the geometrical properties of the fractures and heterogeneity of seepage problem of fractured rocks fairly well. Consequently, the discrete fracture network models become useful and widely applied for theoretical researches and engineering applications. However, engineering applications of the discrete models can be restricted if the field mapping results about distribution of fractures are not available; for the demand of calibration, such model needs more data than equivalent continuum model [Berkowitz, 2002].

When adopting equivalent continuum models to predict the seepage behavior of

fractured rocks, the premise is that there exists a representative element volume (REV), and the key point is the determination of the permeability tensor of the fractured rocks. Since fracture distribution in the rocks is geometrically complicated, the so-called REV may or may not exist at the scales of the problems concerned. If the REV cannot be established, it is no longer suitable to employ the equivalent continuum model. Instead, the models of the discrete fracture network may be applied to analyze the flow behavior through fractured rocks. The steady seepage problems for fracture networks include confined and unconfined seepage (seepage with free surfaces) problems. For the confined seepage problems, the seepage flow domain and boundary conditions are known, and the solutions to this type of problems usually are linear ones. For the seepage problems with free surfaces, the seepage flow domain and the location of the free surface are unknown in advance, and the solutions to this type of the problems are typically nonlinear and require iterative calculations. At present, studies on steady seepage flow through fracture networks mainly focus on confined seepage analysis, while for the unconfined seepage problem with free surface, few works were carried out.

Finite element methods are powerful tools for simulation of seepage problems with free surfaces. For seepage in porous media, both adaptive mesh and fixed mesh approaches were proposed in the literature. The adaptive mesh approaches [Taylor and Brown, 1967; Finn, 1967; Neuman and Witherspoon, 1970] usually easily result in mesh malformation and convergence problems, and are therefore substituted by the fixed mesh approaches gradually. The fixed mesh approaches include the residual flow method [Desai and Li, 1983], the initial flow method [Zhang et al., 1988], the permeability adjustment method [Bathe and Khoshgoftaar, 1979] and the variational inequality methods [Kikuchi, 1977; Brezis et al., 1978; Alt, 1980; Oden and Kikuchi, 1980; Westbrook, 1985; Lacy and Prevost, 1987; Zheng et al., 2005]. Among the proposed fixed mesh approaches, the variational inequality method is established on a rigorous mathematical basis. By constructing a new boundary value problem defined on a fixed region, it transforms the free surface into an internal boundary. Once the problem is solved, the free surfaces can be determined in the light of the water head values of nodes of the finite elements in the fixed region. This study aims to develop a numerical method for the free-surface seepage analysis in complex fracture networks.

5.2 Statement of the problem

Since the hydraulic conductivity of intact rock is extremely low, the main flow

pathways for groundwater are dominated by fracture networks. It should be noticed that a fracture network is not the same as a percolating network for groundwater. The main difference between them lies in the fact that there may be dead-end fractures and isolated fractures and singly unconnected fractures in the fracture system, which should be removed since they do not contribute to groundwater flow. In this sense, a fracture network needs to be regularized to become a completely connected graph, namely, the percolating network. From a viewpoint of the graph theory, a connected graph indicates that there exists one access at least between any two arbitrary intersections. Figure 1(a) and 1(b) show a randomly generated fracture network and the percolating network after its regularization, respectively.

As shown in Figure 1, we take the steady seepage flow through a fractured rock slope as an example. For the seepage flow problem with free surface, groundwater actually flows only in the wet domain Ω_w below a free surface Γ_f . Obviously, the wet domain Ω_w will be determined if the free surface Γ_f is located. For seepage flow through porous media, free surface is a continuous surface where the pressure head is zero and the normal flux is also zero. However, when considering fractured rocks and ignoring the permeability of intact rock, fluid flows directionally along the fracture network concerned. In such a case, a free surface in a fracture network is composed of the zero pressure water table surface in the discrete fractures. Therefore, we can define the free surface by sequentially connecting the locations of fracture surfaces where water pressure is zero, as shown in Figure 5.1. Keep in mind that a free surface in a fracture network is not a flow line any more, which is different from the one defined in porous media.

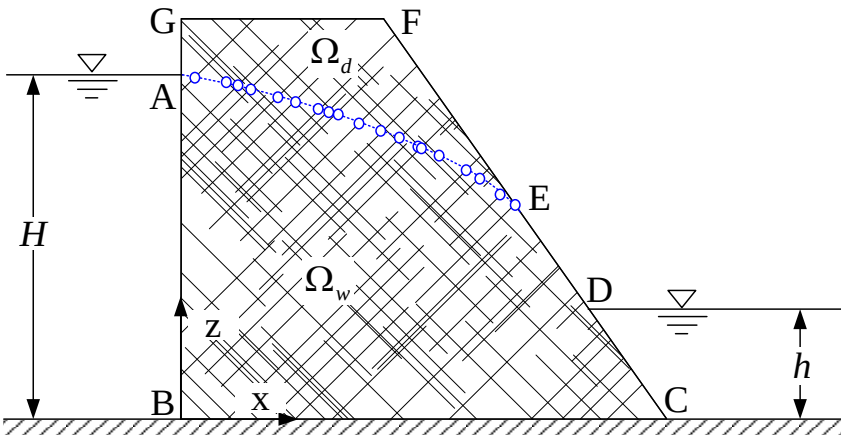

(a) initially generated fracture network;

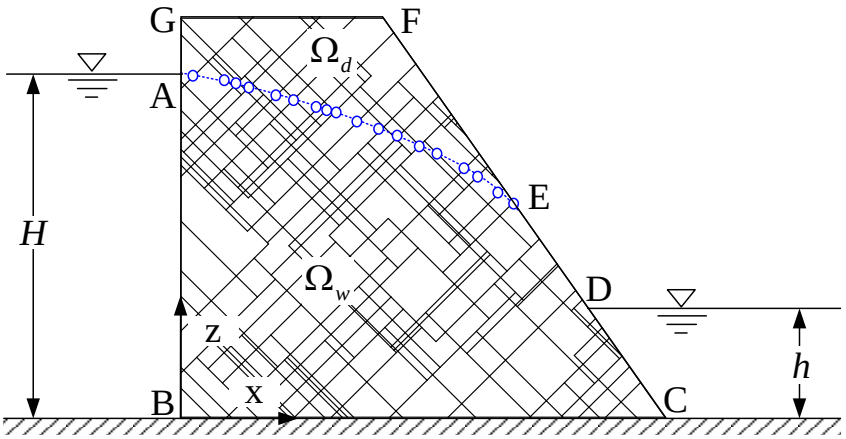

(b) percolating network after regularization

Figure 5.1 Illustration of seepage flow with free surface through a fractured rock slope

For the fractured rock slope illustrated in Figure 5.1, we suppose that the upstream and downstream water levels are located at point A and D respectively, segment BC is an impermeable boundary, E is the seepage point, and segment AE is the free surface in the fracture network. In order to establish the PDE formulation for the problem of free surface seepage through the fracture network, the following assumptions are introduced: (1) the fluid is incompressible; (2) the intact rock matrix is impermeable and water flows only in the percolating network; and (3) the flow of water in the fractures follows the cubic law.

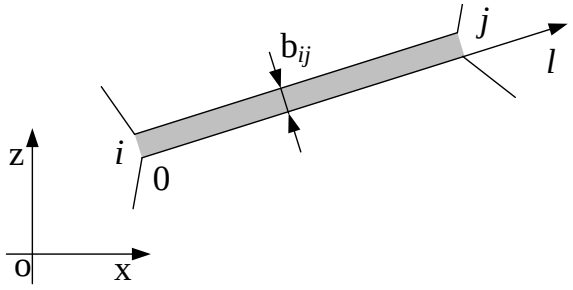

Figure 5.2 Local coordinate system for fracture segment *ij*.

Take the fracture segment as a pair of smooth, parallel plates and set a local coordinate system for an arbitrary fracture segment *ij*, as shown in Figure 5.2. According to Darcy's law, the flow velocity within the fracture segment *ij* can be expressed as:

$$v_{ij} = -k_{ij}\frac{\partial \phi}{\partial l} \qquad (\text{in } \Omega_w) \qquad (5\text{-}1)$$

where $\phi = z + p/r_w$ is the total head, p the pressure head, z the vertical coordinate, r_w water unit weight; k_{ij} is the permeability of the facture segment ij and can be obtained by the cubic law, given by

$$k_{ij} = \frac{g b_{ij}^{\ 2}}{12\upsilon} \tag{5-2}$$

in which g is the gravity acceleration, b_{ij} is the hydraulic aperture of fracture ij, and υ is the dynamic viscosity of water.

The flow of water in fracture segment ij is determined by the equation of continuity

$$\frac{\partial v_{ij}}{\partial l} = 0 \quad (\text{in } \Omega_w) \tag{5-3}$$

It can be seen from Equation (5-3) that v_{ij} is constant within the fracture segment ij. In this study, the endpoints of fractures and the intersections between fractures are termed as nodes. Assuming that there are m_i fracture segments converge at node i, as shown in Figure 5.3. Due to the fact that node i itself cannot store water, the algebraic sum of flux at node i should be null according to the principle of mass conservation, i.e.,

$$\sum_{j=1}^{m_i} b_{ij} v_{ij} = 0 \quad (\text{in } \Omega_w) \tag{5-4}$$

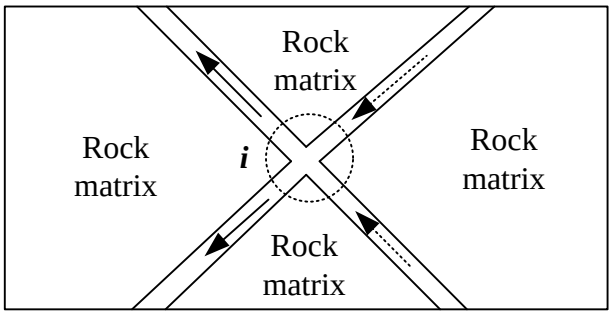

Figure 5.3 Schematic diagram for water flow at fracture intersection.

The water flow in the wet domain Ω_w should satisfy the continuity equations (5-3) and (4), as well as the following boundary conditions:

(1) The condition on the water head boundary

$$\phi_i = \bar{\phi} \qquad (\text{node } i \in \Gamma_\phi = \text{AB} + \text{CD}) \tag{5-5}$$

where $\bar{\phi}$ is the known head on Γ_ϕ. For the upstream and downstream faces, $\bar{\phi}$ equals to H and h, respectively.

(2) The condition on the flux boundary

$$q_{ij} = b_{ij} v_{ij} = 0 \qquad (\text{node } i \in \Gamma_q = \text{BC}) \tag{5-6}$$

where Γ_q is the impermeable boundary.

(3) The condition on the free surface boundary

$$\phi_c = z_c, \quad q_{ic}|_{\Omega_w} = q_{cj}|_{\Omega_d} = 0 \qquad (\text{fracture } ij \text{ a crosses } \Gamma_f = \text{AE}) \tag{5-7}$$

where *c* stands for the intersection point of fracture *ij* and the free surface.

(4) The condition on the seepage face boundary

$$\phi_i = z_i, \quad q_{ij} \le 0 \qquad (\text{ node } \ i \in \Gamma_s' = \mathrm{DE} \ ) \tag{5-8}$$

So far, we established the basic equations and boundary conditions for the free surface seepage problems in fracture networks. Since the location of the free surface is unknown beforehand, the main task of analyzing unconfined seepage through the fracture network is how to determine the location of the free surface.

5.3 PDE formulation on the whole fracture network domain

To construct a boundary value problem defined on the whole fracture network, the Darcy's law only applicable to the wet domain Ω_w is extended to the whole fracture network domain Ω ($\Omega = \Omega_w \cup \Omega_d$). The extended Darcy's law can be written as

$$v_{ij} = -k_{ij} \frac{\partial \phi}{\partial l} + v_0 \tag{5-9}$$

In which v_0 is the initial velocity of flow, and is employed to counteract the suppositional seepage velocity in Ω_d,

$$v_0 = H(\phi - z) k_{ij} \frac{\partial \phi}{\partial l} \tag{5-10}$$

where $H(\phi - z)$ is a Heaviside function

$$H(\phi - z) = \begin{cases} 0 & if \ \phi \ge z \ \ (in \ \ \Omega_w) \\ 1 & if \ \phi < z \ \ (in \ \ \Omega_d) \end{cases} \tag{5-11}$$

Obviously, the flow velocity v_{ij} defined by the Equation (5-9) still obeys the continuity equation (5-3). To avoid the uncertainty of Ω_w, a boundary value problem on the whole fracture network is constructed. It comes to find a function ϕ which satisfies:

(1) The extended Darcy's law (5-9), the continuity equation (5-3) and the mass conversation equation (5-4);

(2) The water head boundary condition (5-5) at $\Gamma_\phi = \mathrm{AB} + \mathrm{CD}$;

(3) The flux boundary condition (5-6) at $\Gamma_q = \mathrm{BC}$

(4) The Signorini's type complementary condition at the rest of boundary $\Gamma_s = \mathrm{AGFD}$, which reads:

$$\begin{cases} \phi_i \le z_i, q_{ij} \le 0 \\ (\phi_i - z_i) q_{ij} = 0 \end{cases} \quad (\text{node } \ i \in \Gamma_s = \mathrm{AGFD}) \tag{5-12}$$

The total water head ϕ on the entire fracture network domain Ω has the following properties: (1) the maximum and minimum values of ϕ are the elevations *H* and *h* of the water level on the upstream and downstream boundaries, respectively, see Figure 1; (2) ϕ divides the entire domain Ω into two sub-domains, namely, the wet domain

$$\Omega_w = \left\{(x,z)\middle|\phi(x,z) \geq z,\ \ (x,z) \in \Omega\right\} \tag{5-13}$$

and the dry domain

$$\Omega_d = \left\{(x,z)\middle|\phi(x,z) < z,\ \ (x,z) \in \Omega\right\} \tag{5-14}$$

The proof is as follows. For an arbitrary fracture segment *ij*, firstly, ϕ only reaches its maximum or minimum values at node *i* or *j* because ϕ varies linearly along the fracture segment ij according to the continuity equation $\partial v_{ij} / \partial l = 0$. Secondly, if ϕ reaches its maximum (or minimum) value at node i, then there is $q_{ij} > 0$ (or $q_{ij} < 0$). For the whole fracture network, it is followed that ϕ cannot reach its maximum value at the nodes inside the fracture network Ω, nodes on the impermeable boundary Γ_q and the potential seepage boundary Γ_s. If ϕ reaches its maximum value at a certain node *i* inside Ω, then for all the fractures that connected to node *i*, there is $\sum_{j=1}^{m_i} q_{ij} > 0$, which contradicts the mass conservation equation (5-4). If ϕ arrives in its maximum value at a certain node *i'* located on the impermeable boundary $\Gamma_q = \mathrm{BC}$ or the potential seepage boundary $\Gamma_s = \mathrm{AGFD}$, then there is $q_{i'j} > 0$, which contradicts the boundary condition (6) or (12). Definitely, ϕ will not arrive in its maximum value on the downstream water head boundary $\Gamma_\phi = \mathrm{CD}$. Hence, ϕ can get its maximum value *H* only on the upstream water head boundary $\Gamma_\phi = \mathrm{AB}$.

Similarly, it is not possible for ϕ to get its minimum value at the nodes located inside the fracture network Ω or at the nodes on the impermeable boundary Γ_q. If ϕ reaches its minimum value at a certain node *i* inside Ω, then for all the fractures that connected to node *i*, we have $\sum_{j=1}^{m_i} q_{ij} < 0$, which contradicts the mass conservation equation (5-4). If ϕ gets its minimum value at a certain node *i'* located on the impermeable boundary $\Gamma_q = \mathrm{BC}$, we have $q_{i'j} < 0$, which contradicts the boundary condition (6). Again, if ϕ reaches its minimum value at the node *i* located on the boundary $\Gamma_s = \mathrm{AGFD}$, we have $q_{ij} < 0$. According to the complementary boundary condition (12), we have $\phi_i = z_i$ under this condition. However $z_i > h$, thus ϕ can get its minimum value h only on the downstream water head boundary $\Gamma_\phi = \mathrm{CD}$.

According to the above discussion and the definition of potential function, $\phi = z + p / r_w$, one can conclude that $p > 0$ at the nodes located the boundaries AB, BC and CD, see Figure 1. In the fractures near the boundary ABCD, the potential function

ϕ varies linearly, therefore there exists a domain, written as Ω_w, in the fracture network where water pressure p is positive. Analogously, for the nodes located on the boundary AGF, we have $p/r_w = \phi - z < H - z < 0$. Therefore, there exists a domain, written as Ω_d, in the fracture network where water pressure p has a negative value. Till now, the aforementioned properties of ϕ have been verified.

To make the restriction of potential function ϕ on the wet domain Ω_w be the solution to the original problem, it still demands that on the interface $\Gamma_f = \{(x,z) \mid \phi = z\}$ between the dry domain Ω_d and the wet domain Ω_w, ϕ satisfy the flux equilibrium condition

$$q_{ic}|_{\Omega_w} = q_{cj}|_{\Omega_d} = 0 \quad \text{on} \quad \Gamma_f = \text{AE} \tag{5-15}$$

Condition (5-15) on Γ_f is necessary for the PDE formulation of this problem, which remains with the internal free boundary condition.

To sum up, the PDE formulation defined on the entire fracture network domain Ω is as follows: seek a function ϕ which satisfies the controlling equations (5-9), (5-3) and (5-4), the external boundary conditions (5-5), (5-6) and (5-12), together with the internal free surface boundary condition (5-15).

The PDE formulation for free-surface seepage problem defined on the entire fracture network domain is now established. The external free boundary problem has been transformed into the internal boundary one, and the uncertainty of the free surface Γ_f in the 2D space has been transformed into that of the seepage point E at the potential seepage surface DFGA. Thus, the difficulty for unconfined seepage analysis has been reduced to a great extent.

5.4 VI formulation on the whole fracture network domain

Since there are an unknown internal free surface Γ_f and a Signorini's complementary condition on the seepage face in the aforementioned PDE formulation, it is very difficult to find a trial function for a numerical solution. To make Condition (15) on Γ_f and the flux component of Condition (12) on Γ_s become natural boundary conditions, we seek a variational inequality (VI) formulation which is equivalent to the PDE formulation in mathematics.

Given a trial function set,

$$\Phi_{VI} = \left\{ \varphi \mid \varphi_i = \bar{\phi}, on \quad \Gamma_\phi; \varphi_i \le z_i, on \quad \Gamma_s \right\} \tag{5-16}$$

the VI formulation equivalent to the PDE formulation can be represented as: find a function

ϕ in Φ_{VI}, so that for $\forall \psi \in \Phi_{VI}$, there holds

$$\xi(\phi, \psi - \phi) \geq \zeta_\phi(\psi - \phi) \tag{5-17}$$

where $\xi(\phi, \psi - \phi)$ and $\zeta_\phi(\psi - \phi)$ take the following form

$$\xi(\phi, \psi - \phi) \equiv \sum_{\Omega} \int_{l_{ij}} \frac{\partial(\psi - \phi)}{\partial l} b_{ij} k_{ij} \frac{\partial \phi}{\partial l} dl \tag{5-18}$$

$$\zeta_\phi(\psi - \phi) \equiv \sum_{\Omega} \int_{l_{ij}} \frac{\partial(\psi - \phi)}{\partial l} b_{ij} v_0 dl \tag{5-19}$$

In order to prove the equivalence between these two formulations, we first expand $\xi(\phi, \psi - \phi) - \zeta_\phi(\psi - \phi)$ via integration by parts

$$\begin{aligned}
&\xi(\phi, \psi - \phi) - \zeta_\phi(\psi - \phi) = \sum_{\Omega} \int_{l_{ij}} \frac{\partial(\psi - \phi)}{\partial l} \left(b_{ij} k_{ij} \frac{\partial \phi}{\partial l} - b_{ij} v_0 \right) dl \\
&= \sum_{\Omega} \left(-(\psi - \phi) b_{ij} v_{ij} \Big|_0^{l_{ij}} + \int_{l_{ij}} (\psi - \phi) b_{ij} \frac{\partial v_{ij}}{\partial l} dl \right) \\
&= \sum_{\Omega} \left((\psi_i - \phi_i) b_{ij} v_{ij} - (\psi_j - \phi_j) b_{ij} v_{ij} \right) + \sum_{\Omega} \int_{l_{ij}} (\psi - \phi) b_{ij} \frac{\partial v_{ij}}{\partial l} dl \\
&= \sum_{i=1}^{n} \left(\sum_{j=1}^{m_i} (\psi_i - \phi_i) b_{ij} v_{ij} \right) + \sum_{\Omega} \int_{l_{ij}} (\psi - \phi) b_{ij} \frac{\partial v_{ij}}{\partial l} dl
\end{aligned} \tag{5-20}$$

where n stands for the total number of nodes in the whole domain.

5.4.1 The proof for PDE $\Rightarrow$ VI

If ϕ is the solution to the PDE formulation, then by substituting the continuity equation (5-3), mass conservation equation (5-4) and the external boundary conditions (5-5), equation (5-6) and equation (5-12) into Equation (5-20), combing with the fact of $\forall \psi \in \Phi_{VI}$, we obtain

$$\begin{aligned}
\xi(\phi, \psi - \phi) - \zeta_\phi(\psi - \phi) &= \sum_{i \in \Gamma_s} \left(\sum_{j=1}^{m_i} (\psi_i - \phi_i) q_{ij} \right) \\
&= \sum_{i \in \Gamma_s} \left(\sum_{j=1}^{m_i} (\psi_i - z_i) q_{ij} \right) - \sum_{i \in \Gamma_s} \left(\sum_{j=1}^{m_i} (\phi_i - z_i) q_{ij} \right) \\
&= \sum_{i \in \Gamma_s} \left(\sum_{j=1}^{m_i} (\psi_i - z_i) q_{ij} \right) \geq 0
\end{aligned} \tag{5-21}$$

Therefore, ϕ is also the solution to the VI formulation.

5.4.2 The proof for VI $\Rightarrow$ PDE

Suppose ϕ is the solution to VI formulation. From the Equations (5-17), (5-20) and

the fact that both ϕ and ψ belong to Φ_{VI}, i.e., they satisfy the water head boundary condition on Γ_ϕ, we have

$$\begin{aligned}&\xi(\phi,\psi-\phi)-\zeta_\phi(\psi-\phi)\\&=\sum_{i\in\Omega_{in}}\left(\sum_{j=1}^{m_i}(\psi_i-\phi_i)b_{ij}v_{ij}\right)+\sum_{i\in\Gamma_q\cup\Gamma_s}\left(\sum_{j=1}^{m_i}(\psi_i-\phi_i)b_{ij}v_{ij}\right)+\sum_{\Omega}\int_{l_{ij}}(\psi-\phi)b_{ij}\frac{\partial v_{ij}}{\partial l}\geq 0\end{aligned}\tag{5-22}$$

where Ω_{in} denotes all the nodes inside the fracture network.

Take $\psi=\phi+\theta_1$ and $\psi=\phi-\theta_1$ respectively, where θ_1 is any function that equals to zero at all the nodes on the entire fracture network domain. The continuity equation is derived

$$\frac{\partial v_{ij}}{\partial l}=0 \quad (\text{in } \Omega)\tag{5-23}$$

Therefore, Equation (5-22) can be reduced to

$$\begin{aligned}&\xi(\phi,\psi-\phi)-\zeta_\phi(\psi-\phi)\\&=\sum_{i\in\Omega_{in}}\left(\sum_{j=1}^{m_i}(\psi_i-\phi_i)b_{ij}v_{ij}\right)+\sum_{i\in\Gamma_q}\left(\sum_{j=1}^{m_i}(\psi_i-\phi_i)b_{ij}v_{ij}\right)+\sum_{i\in\Gamma_s}\left(\sum_{j=1}^{m_i}(\psi_i-\phi_i)b_{ij}v_{ij}\right)\geq 0\end{aligned}\tag{5-24}$$

Take $\psi=\phi+\theta_2$ and $\psi=\phi-\theta_2$, respectively, in Equation (5-24), with θ_2 being any function that equals to zero at the nodes located on boundaries Γ_ϕ, Γ_q and Γ_s. The mass conservation equation at any nodes inside the fracture network is derived

$$\sum_{j=1}^{m_i}b_{ij}v_{ij}=0 \quad (\text{in } \Omega)\tag{5-25}$$

Therefore, Equation (24) can be simplified as

$$\begin{aligned}&\xi(\phi,\psi-\phi)-\zeta_\phi(\psi-\phi)\\&=\sum_{i\in\Gamma_q}\left(\sum_{j=1}^{m_i}(\psi_i-\phi_i)b_{ij}v_{ij}\right)+\sum_{i\in\Gamma_s}\left(\sum_{j=1}^{m_i}(\psi_i-\phi_i)b_{ij}v_{ij}\right)\geq 0\end{aligned}\tag{5-26}$$

Let $\psi=\phi+\theta_3$ and $\psi=\phi-\theta_3$ respectively in Equation (5-26), in which θ_3 is any function that becomes null at the nodes located on boundaries Γ_ϕ and Γ_s. The flux boundary condition on Γ_q is obtained as:

$$q_{ij}=b_{ij}v_{ij}=0 \qquad (\text{node } i\in\Gamma_q=\text{BC})\tag{5-27}$$

Therefore, Equation (5-26) can be simplified as

$$\begin{aligned}&\xi(\phi,\psi-\phi)-\zeta_\phi(\psi-\phi)\\&=\sum_{i\in\Gamma_s}\left(\sum_{j=1}^{m_i}(\psi_i-z_i)q_{ij}\right)-\sum_{i\in\Gamma_s}\left(\sum_{j=1}^{m_i}(\phi_i-z_i)q_{ij}\right)\geq 0\end{aligned}\tag{5-28}$$

Notice that the second term on the right side of Equation (5-28) is a constant. Thus, if the above inequality holds for $\forall\psi\in\Phi_{VI}$, then the first term on the right side of the

Equation (5-28) must be non-negative, i.e.

$$\sum_{i\in\Gamma_s}\left(\sum_{j=1}^{m_i}(\psi_i - z_i)q_{ij}\right)\geq 0 \tag{5-29}$$

Since ψ is any function that satisfies $\psi \leq z$ on Γ_s, we obtain

$$q_{ij}\leq 0 \quad (\text{node } i\in\Gamma_s) \tag{5-30}$$

Of course, we can also take $\psi = z$ in Equation (5-28), which leads to

$$\sum_{i\in\Gamma_s}\left(\sum_{j=1}^{m_i}(z_i - \phi_i)q_{ij}\right)\geq 0 \tag{5-31}$$

Combining Equations (5-30), (5-31) with the condition of $\phi_i \leq z_i$ on Γ_s, we can obtain the complementary condition on Γ_s as

$$(\phi_i - z_i)q_{ij} = 0 \quad (\text{node } i\in\Gamma_s) \tag{5-32}$$

In order to deduce the inner boundary condition on Γ_f, the integration on Ω in Equation (5-20) is now represented as the sum of the integrations in sub-domain Ω_w and Ω_d.

$$\begin{aligned}&\xi(\phi,\psi-\phi)-\zeta_\phi(\psi-\phi)\\&=\sum_{\Omega_w}\left(\sum_{j=1}^{m_i}(\psi_i-\phi_i)q_{ij}\right)+\sum_{\Omega_w}\int_{l_{ij}}(\psi-\phi)b_{ij}\frac{\partial v_{ij}}{\partial l}dl\\&+\sum_{\Omega_d}\left(\sum_{j=1}^{m_i}(\psi_i-\phi_i)q_{ij}\right)+\sum_{\Omega_d}\int_{l_{ij}}(\psi-\phi)b_{ij}\frac{\partial v_{ij}}{\partial l}dl\geq 0\end{aligned} \tag{5-33}$$

Using the results of above derivations, the following inequality holds for $\forall\psi\in\Phi_{IV}$.

$$\begin{aligned}&\xi(\phi,\psi-\phi)-\zeta_\phi(\psi-\phi)=\\&\sum_{c\in\Gamma_f}(\psi_c-\phi_c)(q_{ci}|_{\Omega_w}+q_{cj}|_{\Omega_d})+\sum_{i\in\Gamma_s}\left(\sum_{j=1}^{m_i}(\psi_i-\phi_i)q_{ij}\right)\geq 0\end{aligned} \tag{5-34}$$

Take $\psi = \phi + \theta_4$ and $\psi = \phi - \theta_4$, respectively, in Equation (5-34), with θ_4 being an arbitrary function that becomes null at the nodes located on boundaries Γ_ϕ and Γ_s, then we get

$$q_{ic}|_{\Omega_w} = q_{cj}|_{\Omega_d} = 0 \tag{5-35}$$

Up to the present, all the equations and boundary conditions in the PDE formulation have been derived. Hence, the solution to the VI formulation is also the solution to the PDE one. Obviously, in the VI formulation, except for the condition $\phi_i = \bar{\phi}$ on the up- and down-stream water head boundary Γ_ϕ and the condition $\phi_i \leq z_i$ on the potential seepage face Γ_ϕ, all the remaining boundary conditions involving flux components on Γ_q, Γ_f and Γ_s become natural boundary conditions. Therefore, the requirement for trial function in VI formulation is much lower than that for the PDE formulation.

5.5 Numerical solution by finite element method

5.5.1 FE formulation

The fracture segments in the fracture network are modeled as line elements in finite element method. The nodes of the element are just the two endpoints of the fracture segment. By using linear interpolation, the hydraulic potential function of the fracture segment *ij* can be written as

$$\phi = N_i\phi_i + N_j\phi_j \tag{5-36}$$

where ϕ_i and ϕ_j are the total water head values of nodes *i* and *j*, respectively; N_i and N_j are shape functions with $N_i = 1 - l/l_{ij}$ and $N_j = l/l_{ij}$.

Adopting finite element approximation to Equation (5-17), the discrete form of the VI is stated as follows: Seek a water head vector $\boldsymbol{\phi}^{r+1}$ in Φ_{VI}^h, such that for $\forall \boldsymbol{\psi} \in \Phi_{VI}^h$, there always holds

$$(\boldsymbol{\psi} - \boldsymbol{\phi}^{r+1})^{\mathrm{T}} \boldsymbol{K}\boldsymbol{\phi}^{r+1} \geq (\boldsymbol{\psi} - \boldsymbol{\phi}^{r+1})^{\mathrm{T}} \boldsymbol{q}^r \tag{5-37}$$

in which

$$\boldsymbol{K} = \sum_{\Omega} \boldsymbol{K}_e, \quad \boldsymbol{K}_e = \int_{l_{ij}} \boldsymbol{B}^{\mathrm{T}} b_{ij} k_{ij} \boldsymbol{B} dl \tag{5-38}$$

$$\boldsymbol{q}^r = \sum_{\Omega} \int_{l_{ij}} \boldsymbol{B}^{\mathrm{T}} b_{ij} \boldsymbol{v}_0^r dl = \boldsymbol{K}_\lambda \boldsymbol{\phi}^r \tag{5-39}$$

$$\boldsymbol{K}_\lambda = \sum_{\Omega} \boldsymbol{K}_\lambda^e, \quad \boldsymbol{K}_\lambda^e = \int_{l_{ij}} H(\phi^r - z) \boldsymbol{B}^{\mathrm{T}} b_{ij} k_{ij} \boldsymbol{B} dl \tag{5-40}$$

$$\boldsymbol{B} = \left\{ \frac{\partial N_i}{\partial l} \quad \frac{\partial N_j}{\partial l} \right\} \tag{5-41}$$

$$\Phi_{VI}^h = \left\{ \varphi \,|\, \varphi \in R^n; \varphi_i = \overline{\phi_i},\ for\ \ i \in \Gamma_\phi; \varphi_i \leq z_i,\ for\ \ i \in \Gamma_s \right\} \tag{5-42}$$

where *r* denotes the iteration step; $\boldsymbol{B}$ is the geometric matrix of the line element *ij*; $\boldsymbol{K}_e$ and $\boldsymbol{K}$ stand for the local element hydraulic conductivity matrix and global hydraulic conductivity matrix, respectively; $\boldsymbol{q}$ is the virtual flux matrix caused by the initial flow rate $\boldsymbol{v}_0$; and $\boldsymbol{K}_\lambda^e$ and $\boldsymbol{K}_\lambda$ denote the local element penalized hydraulic conductivity matrix and the global penalized hydraulic conductivity matrix, respectively.

5.5.2 The penalized Heaviside function

When solving the variational inequality in the discrete form (5-37), numerical

instability may occur due to the discontinuity of the Heaviside function (11). The main reason lies in the fact that the Heaviside function is a discontinuous step function (as shown in Figure 5.4a), which may cause oscillation of numerical integration when fracture elements intersect the free surface.

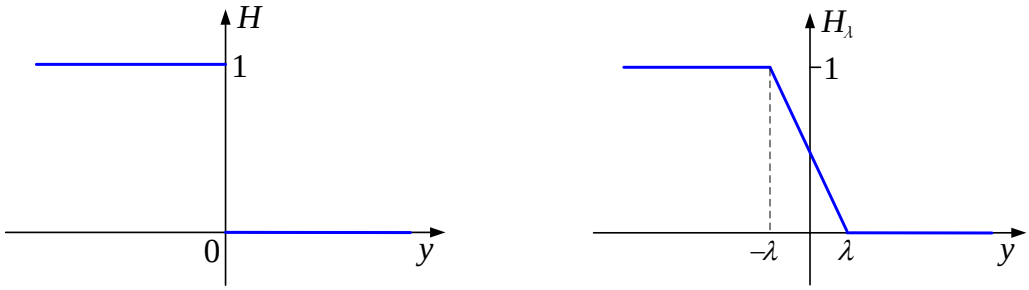

(a) step function (b) continuous function

Figure 5.4 Two types of penalized Heaviside functions

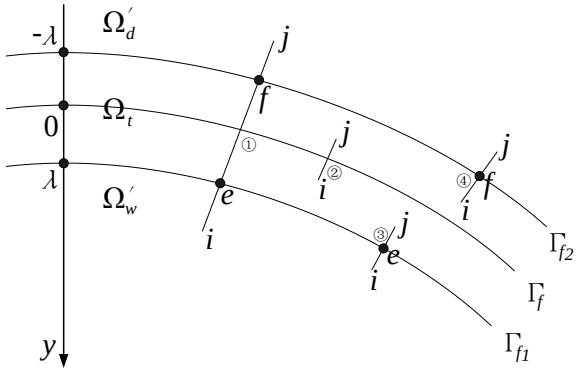

Figure 5.5 Fracture elements located in the transition domain Ω_t

In order to evade the potential instability of the FE solution process, Heaviside function in Equation (5-37) is substituted by a continuous penalized Heaviside function, as is shown in Figure 5.4b. The penalized Heaviside function is written as

$$H_\lambda(\phi - z) = \begin{cases} 1 & if \quad \phi - z \le -\lambda \\ \dfrac{\lambda - (\phi - z)}{2\lambda} & if \quad -\lambda < \phi - z < \lambda \\ 0 & if \quad \phi - z \ge \lambda \end{cases} \tag{5-43}$$

where the penalty parameter λ are defined as half of the width of the transition layer from the wet domain to the dry domain, as shown in Figure 5.5. Generally, we take the value of λ as the mean length of fracture elements. For specially complicated cases where dramatic water depression occurs in the complex fracture network, the value of λ can be properly relaxed to obtain good convergence. Obviously, when λ tends towards zero, the penalized Heaviside function $H_\lambda(\phi - z)$ tends towards the original Heaviside function $H(\phi - z)$.

In reality, there is a transition layer between the wet and dry domains for unconfined water seepage due to the capillary pressure effects (Vardose zone), where water pressure decreases to null gradually. Therefore, for the unconfined seepage problems through fractured rocks, the whole material domain can be divided into three sub-domains for FE analysis, i.e. the domain Ω'_w that consists of the fracture elements absolutely located in the wet domain; the domain Ω'_d that consists of the fracture elements absolutely located in the dry domain; and the domain Ω_t that consists of the fracture elements located in the transition zone from the wet domain to the dry domain near free surface. As can be seen from Figure 5.5, the fracture elements located in the transition domain Ω_t can generally be classified into the following four types:

Type 1: Node *i* of the fracture element *ij* located in the wet domain Ω'_w while node *j* in the dry domain Ω'_d

When the fracture element *ij* passes through the transition layer, and nodes *i* and *j* located in the wet domain and dry domain, respectively, conditions $\phi_i - z_i \geq \lambda$ and $\phi_j - z_j \leq -\lambda$ are tenable in this case. The pressure head at any point in the fracture element *ij* can be written as

$$\begin{aligned} \phi - z &= N_i\phi_i + N_j\phi_j - N_i z_i - N_j z_j \\ &= y_i - (y_i - y_j)l / l_{ij} \end{aligned} \tag{5-44}$$

where y_i and y_j denote the pressure head at the nodes *i* and *j* respectively with $y_i = \phi_i - z_i$ and $y_j = \phi_j - z_j$.

From Equations (5-43) and (5-44), the penalized hydraulic matrix of the fracture element *ij* can be written as

$$\begin{aligned} \boldsymbol{K}_\lambda^e &= \int_{l_{ij}} H_\lambda \boldsymbol{B}^T b_{ij} k_{ij} \boldsymbol{B} dl \\ &= [\int_{l_{ef}} \frac{\lambda - (\phi - z)}{2\lambda} dl + \int_{l_{fj}} dl] \boldsymbol{B}^T b_{ij} k_{ij} \boldsymbol{B} \\ &= \frac{-y_j}{y_i - y_j} l_{ij} b_{ij} k_{ij} \boldsymbol{B}^T \boldsymbol{B} \end{aligned} \tag{5-45}$$

Type 2: Both nodes *i* and *j* of the fracture element *ij* are located in the transition domain Ω_t

When the fracture element *ij* is absolutely located inside the transition domain, conditions $-\lambda < \phi_i - z_i < \lambda$ and $-\lambda < \phi_j - z_j < \lambda$ are tenable in this case. From Equations (43) and (44), the penalized hydraulic matrix of fracture *ij* can be expressed as

$$\boldsymbol{K}_{\lambda}^{e}=\int_{l_{ij}} H_{\lambda}\boldsymbol{B}^{T}b_{ij}k_{ij}\boldsymbol{B}dl$$

$$=(\int_{l_{ij}}\frac{\lambda-(\phi-z)}{2\lambda}dl)\boldsymbol{B}^{T}b_{ij}k_{ij}\boldsymbol{B}$$

$$=\frac{2\lambda-y_i-y_j}{4\lambda}l_{ij}b_{ij}k_{ij}\boldsymbol{B}^{T}\boldsymbol{B} \tag{5-46}$$

Type 3: Node *i* of the fracture element *ij* located in the wet domain Ω_w' while node *j* in the transition domain Ω_t

When the fracture element *ij* only intersects with the lower boundary of the transition layer Γ_{f1}, and nodes *i* and *j* located in the wet domain Ω_w' and the transition domain Ω_t, respectively, conditions $\phi_i-z_i\geq\lambda$ and $-\lambda<\phi_j-z_j<\lambda$ are tenable. From Equations (43) and (44), the penalized hydraulic matrix of fracture *ij* is expressed as

$$\boldsymbol{K}_{\lambda}^{e}=\int_{l_{ij}} H_{\lambda}\boldsymbol{B}^{T}b_{ij}k_{ij}\boldsymbol{B}dl$$

$$=(\int_{l_{ej}}\frac{\lambda-(\phi-z)}{2\lambda}dl)\boldsymbol{B}^{T}b_{ij}k_{ij}\boldsymbol{B}$$

$$=\frac{(\lambda-y_j)^2}{4\lambda(y_i-y_j)}l_{ij}b_{ij}k_{ij}\boldsymbol{B}^{T}\boldsymbol{B} \tag{5-47}$$

Type 4: Node *i* of the fracture element *ij* located in the transition domain Ω_t while node *j* in the wet domain Ω_w'

When the fracture element *ij* only intersects with the upper boundary of the transition layer Γ_{f2}, and nodes *i* and *j* located in the transition domain Ω_t and wet domain Ω_w' respectively, conditions $-\lambda<\phi_i-z_i<\lambda$ and $\phi_j-z_j\leq-\lambda$ are tenable. From Equations (5-43) and (5-44), the penalized hydraulic matrix of the fracture element *ij* is expressed as:

$$\boldsymbol{K}_{\lambda}^{e}=\int_{l_{ij}} H_{\lambda}\boldsymbol{B}^{T}b_{ij}k_{ij}\boldsymbol{B}dl$$

$$=[\int_{l_{if}}\frac{\lambda-(\phi-z)}{2\lambda}dl+\int_{l_{fj}}dl]\boldsymbol{B}^{T}b_{ij}k_{ij}\boldsymbol{B}$$

$$=\frac{2\lambda y_i-4\lambda y_j-\lambda^2-y_i^2}{4\lambda(y_i-y_j)}l_{ij}b_{ij}k_{ij}\boldsymbol{B}^{T}\boldsymbol{B} \tag{5-48}$$

5.5.3 Numerical procedure

For solving the variational inequality of discrete form (5-37), the complementary algorithm proposed by Zheng et al. [32] is adopted to locate the seepage point. For

convenience, the set of nodes located on Γ_s may be divided into the following two subsets:

$$\mathbb{N}_{s1} = \{i \mid i \in \Gamma_s; \phi_i < z_i, q_{ij} = 0\}, \quad \mathbb{N}_{s2} = \{i \mid i \in \Gamma_s; \phi_i = z_i, q_{ij} \le 0\} \tag{5-49}$$

where $\mathbb{N}_{s1}$ denotes the nodal set of all nodes located on the potential seepage surface above the seepage point, while $\mathbb{N}_{s2}$ denotes the nodal set of all nodes located on the potential seepage surface below the seepage point.

The entire FE iterative procedure for the aforementioned discrete VI formulation is summarized in Table 5.1.

The above procedure is similar to the constant stiffness approach in structural analysis, where the global hydraulic matrix is assembled and decomposed only once. Thus this algorithm has superior computation efficiency.

Table 5.1 The iterative algorithm for the seepage flow analysis with free surface in the fracture network

1. Initialize data

2. Take the whole domain of the fracture network as the wet domain. For $\forall i$ on Γ_s, let $i \in \mathbb{N}_{s1}^1$ and $q_{ij}^1 \leftarrow 0$

3. Calculate the element hydraulic matrix $\boldsymbol{K}_e$, then assemble all element hydraulic matrices to form the global hydraulic matrix $\boldsymbol{K}$

$$\boldsymbol{K}_e = \int_{l_{ij}} \boldsymbol{B}^{\mathrm{T}} b_{ij} k_{ij} \boldsymbol{B} dl, \qquad \boldsymbol{K} = \sum_{\Omega} \boldsymbol{K}_e$$

4. Solve Equation $\boldsymbol{K}\boldsymbol{\phi}^1 = 0$ by the precondition conjugate gradient method (PCG), then obtain $\boldsymbol{\phi}^1$

5. Set the iteration step $r \leftarrow 1$

6. Do decomposition to the set of nodes located on Γ_s:

If $i \in \mathbb{N}_{s1}^r$ and $\phi_i^r \ge z_i$, then let $\mathbb{N}_{s1}^{r+1} \leftarrow \mathbb{N}_{s1}^r - \{i\}$ and $\mathbb{N}_{s2}^{r+1} \leftarrow \mathbb{N}_{s2}^r + \{i\}$

If $i \in \mathbb{N}_{s2}^r$ and $q_{ij}^r > 0$, then let $\mathbb{N}_{s1}^{r+1} \leftarrow \mathbb{N}_{s1}^r + \{i\}$ and $\mathbb{N}_{s2}^{r+1} \leftarrow \mathbb{N}_{s2}^r - \{i\}$

7. For $i \in \mathbb{N}_{s1}^{r+1}$, let $q_{ij}^{r+1} \leftarrow 0$; while for $i \in \mathbb{N}_{s2}^{r+1}$, let $\phi_i^{r+1} \leftarrow z_i$

8. Calculate the penalized hydraulic matrix $\boldsymbol{K}_\lambda^e$ of the fracture elements located in Ω_w', Ω_t and Ω_d' respectively, then assemble to form the global penalized matrix $\boldsymbol{K}_\lambda$

$$\boldsymbol{K}_\lambda^e = \int_{l_{ij}} H_\lambda(\phi^r - z) \boldsymbol{B}^T b_{ij} k_{ij} \boldsymbol{B} dl, \qquad \boldsymbol{K}_\lambda = \sum_{\Omega} \boldsymbol{K}_\lambda^e$$

9. Calculate the virtual flux matrix $\boldsymbol{q}^r$, $\boldsymbol{q}^r = \boldsymbol{K}_\lambda \boldsymbol{\phi}^r$

10. Solve Equation $\boldsymbol{K}\boldsymbol{\phi}^{r+1} = \boldsymbol{q}^r$ by PCG method, then obtain $\boldsymbol{\phi}^{r+1}$

11. If $\| \boldsymbol{\phi}^{r+1} - \boldsymbol{\phi}^{r} \| \leq \varepsilon \| \boldsymbol{\phi}^{r+1} \|$, where ε is a user-specified tolerance ($\varepsilon = 10^{-3}$ in this study), turn to step (12); otherwise, let $r \leftarrow r+1$, turn to step (6)

12. Let $\boldsymbol{\phi} = \boldsymbol{\phi}^{r+1}$, then end calculation

5.6 The illustrative examples

The FE solution algorithm of the unconfined seepage analysis for the fracture network is implemented into a computer program named FracSeep. Three typical examples are solved using the program to illustrate the validity and capability of the VI formulation established in this study.

5.6.1 A homogeneous rectangular dam

Consider a homogeneous rectangular dam with a height of 12m and a width of 10m, as shown in Figure 5.6. The bottom boundary of the dam is assumed to be impermeable. The water levels of the upstream and downstream surfaces are 10m and 2m, respectively. An artificial fracture network system formed by two orthogonal sets of fractures with constant hydraulic apertures and constant spacing is employed to simulate the homogeneous isotropic medium. The equivalent hydraulic aperture of the fracture can be expressed as:

$$b = (12\upsilon Bk / g)^{1/3} \qquad (5\text{-}50)$$

where k is the permeability coefficient of the dam material; B is the spacing between the fractures. Specifically in this example, by choosing $k = 4.13 \times 10^{-6} \mathrm{m/s}$ and $B = 0.2\mathrm{m}$, we then obtain $b = 0.1\mathrm{mm}$.

For this problem, the empirical solution of the free surface [Zhou et al., 1996] is

$$z = (100 - 8x)^{1/2} \qquad (5\text{-}51)$$

Figure 6 shows the locations of the free surfaces from the empirical solution and the proposed method, respectively. We can observe from Figure 6 there is good agreement between these two methods.

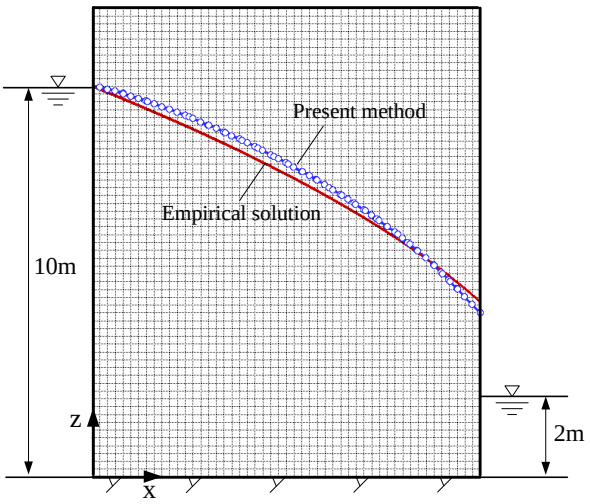

Figure 5.6 Rectangular dam with tail water.

According to Dupuit's formula, the total discharge (per unit width) of a homogeneous dam can be expressed as

$$q = k\frac{h_1^2 - h_2^2}{2L} \qquad (5\text{-}52)$$

where h_1 and h_2 represent the water levels of the upstream and downstream faces, respectively, and L denotes the width of the dam.

The discharge of the dam calculated by Dupuit's formula is $1.98\times10^{-5} m^3/s$, while the numerical solution based on the fracture network seepage analysis is $1.95\times10^{-5} m^3/s$. The error between these two results is only 1.79%, showing that the numerical solution is reasonable and reliable.

5.6.2 DFN model from DECOVALEX-2011 project

In order to evaluate the hydraulic permeability and hydro-mechanical behaviors of the fractured rockmass, the international cooperative research project Decovalex for radioactive waste disposal provided a complicated discrete fracture network (DFN) model of $20\text{m}\times20\text{m}$ in size which contains 7996 fractures (52540 fracture elements) and 29814 nodes in Task C of the fifth stage (Decovalex-2011), as shown in Figure 5.7. The statistical parameters of fractures that generate the DFN model are from the field geological survey at the Sellafield area, Cambria, England [Min et al., 2004]. The trace lengths of the fractures obey a truncated power-law distribution with a fractal dimension of 2.2 and a density of 4.6 m^{-2}. The fracture orientations are assumed to obey the Fisher distribution. The geometric parameters of the identified four sets of fractures are listed in Table 5.2.

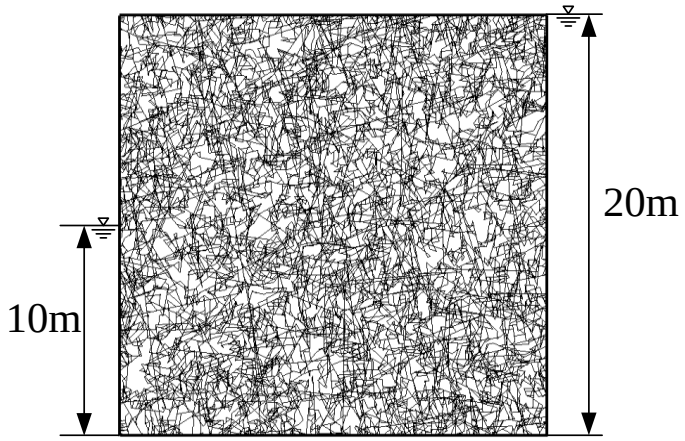

Figure 5.7 Geometry of fracture system in the DFN model with 20m×20m size (adapted from Min et al., 2004).

Table 5.2 Fracture parameters used for DFN generation (Min et al., 2004)

Joint set	Dip/Dip direction	Fisher constant	Fracture density (m^{-2})	Mean trace length (m)
1	8/145	5.9	4.6	0.92
2	88/148	9.0	4.6	0.92
3	76/21	10.0	4.6	0.92
4	69/87	10.0	4.6	0.92

As a challenging example, we employ this DFN model to perform a unconfined seepage analysis. Suppose the water head on the left boundary of the model is 10m, while 20m on the right boundary, and the bottom is impermeable. In order to analyze the influences of hydraulic apertures of the fractures on fluid flow behavior of the fracture network, two cases are considered: (1) the apertures of all fractures are constant and equal to $65\ \mathrm{um}$; (2) fracture apertures obey the lognormal distribution and are related to trace lengths of the fractures by the following equation [3]

$$l=\left\{l_{\min}^{-D}+\left[\frac{g(b_i)-g(b_{in})}{g(b_{im})-g(b_{in})}\right](l_{\max}^{-D}-l_{\min}^{-D})\right\}^{-1/D} \qquad (5\text{-}53)$$

where $l_{\min}$ is the minimum fracture trace length, $l_{\max}$ the maximum trace length; b_{im} and b_{in} stand for the upper and lower limits of fracture aperture respectively; D denotes the fractal dimension. In this equation $g(b_i)=erf[(\ln b_i-\overline{b}_{i\log})/\sqrt{2}\omega]$, the term $\overline{h}_{i\log}$ and ω are the first and second moments of the lognormal distribution of fracture apertures, respectively, and *erf*() is the error function.

Figure 5.8 shows the location of free surface and fluid flow rate distribution in the DFN model under the two different aperture conditions. When the fracture system has a constant hydraulic aperture, the fluid flow rate distribution pattern inside the DFN model is relatively uniform and the free surface is gently depressed. When fracture apertures follow the lognormal distribution and are correlated with fracture trace lengths, the flow pathways are dominated more by the fractures with larger aperture values. Meanwhile, influenced by the random distribution of fracture aperture, the free surface is sharply dropped at local positions. Figure 5.9 shows the flow rates normalized with respect to the mean flow rate in the outlet fractures along the left vertical boundary. Compared with the results from using the constant aperture distribution, change in the flow rates along the left vertical boundary is more abrupt under the correlated aperture-trace length distribution. Figure 5.10 plots the water head contours inside the fracture network for using both the constant aperture and correlated aperture-trace length distributions. It can be observed from Figure 5.10 that the total water head decreases gradually from the upstream to the downstream of the model, which is consistent with the global direction of water flow. This phenomenon is basically in accordance with the seepage flow behavior in continuous media.

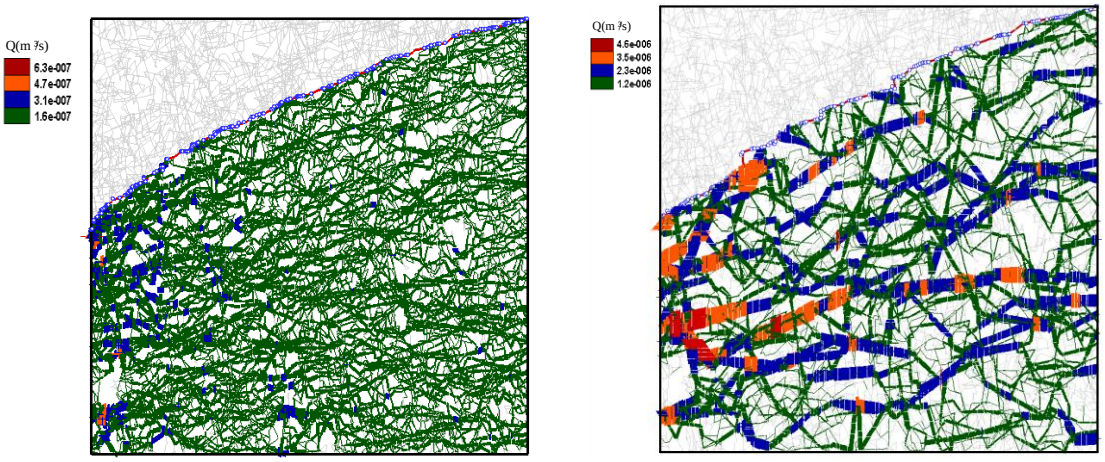

(a) constant apertures of $65um$; (b) correlated aperture-trace length of fractures.

Figure 5.8 Location of free surface and fluid flow rate distribution in the DFN model

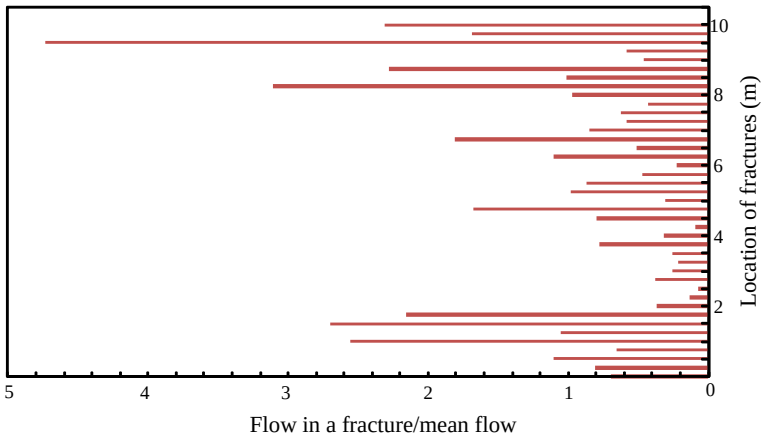

(a) constant apertures of 65μm;

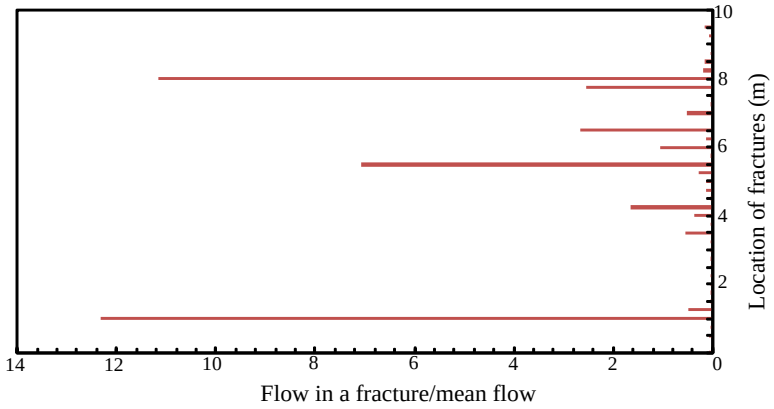

(b) correlated aperture-trace length of fractures. Flow rates are normalized with respect to the mean flow rates (total flow rate divided by the number of fractures) in the boundary.

Figure 5.9 Normalized flow rates in each fracture intersecting the left vertical boundary of the model

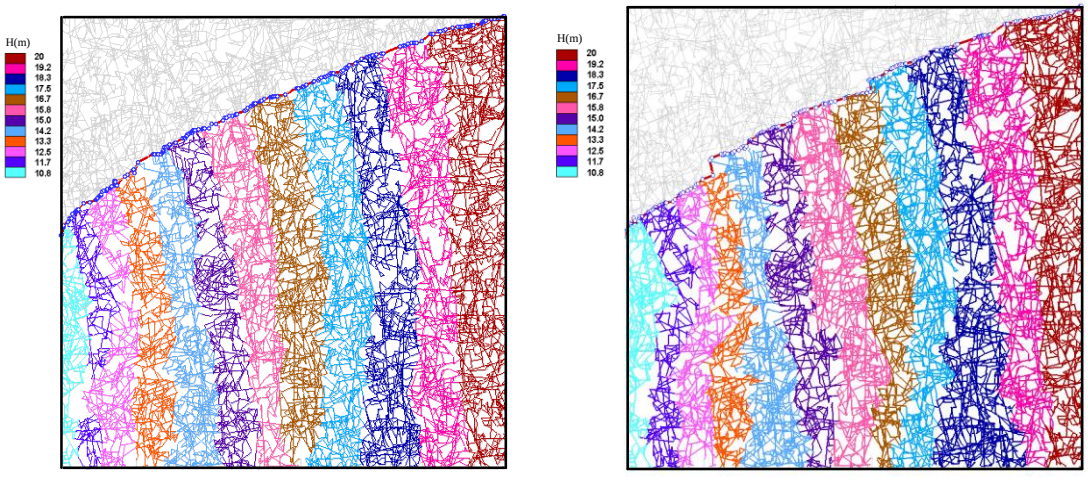

(a) the apertures of all fractures are constant

(b) fracture apertures obey the lognormal distribution and are correlated with fracture trace lengths.

Figure 5.10 The water head contours in the DFN model

5.6.3 A slope of fractured rock

Figure 5.11 shows a rock slope with a height of 202.2 m and a width of 200.0 m. In order to bring down the underground water level in the slope and improve its stability, four layers of drainage tunnels are deployed in the slope. The drainage tunnels have a rectangular section with a height of 3.5m and a width of 3m.

The bedrock of the slope mainly consists of fresh or slightly weathered plagioclase granite. The permeability coefficient of the intact rock is of the magnitude of 10^{-10}cm/s, which can be considered as impermeable compared with the fractures from the practical point of view. Large numbers of fractures of grades IV and V exist in the rock slope and form a fracture network, which controls the groundwater flow in the slope. According to the field geological survey, four sets of fractures are identified and their statistical parameters are listed in Table 5.3 [Zhang, 1999].

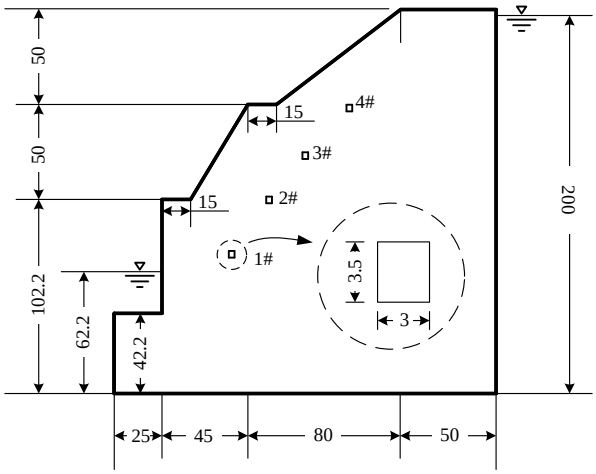

Figure 5.11 Geometry of a rock slope with drainage tunnels.

According to the geometrical parameters and statistic distribution of the fractures given in Table 5.3, the DFN model randomly generated by Monte-Carlo method. The isolated fractures are removed and dead-end fractures are trimmed, which results in a percolating network with 28903 fracture elements and 15851 nodes, as shown in Figure 5.12. The calibration of the DFN model generated by Monte-Carlo method is not considered in this research, since the main focus is to verify the validity of the proposed method and its capability in solving free-surface seepage problems in complicated fracture networks.

Table 5.3 Parameters of fractures and Probability models (Zhang, 1999)

Fracture set	Trace length (m)			Dip (Degree)			Aperture (mm)			Mean Spacing (m)
	Mean Values	Variance	Probability model	Mean Values	Variance	Probability model	Mean Values	Variance	Probability model	
1	25.97	0.52	Normal	74.27	10.00	Normal	0.20	0.10	Lognormal	2.18
2	31.00	0.92	Normal	110.00	15.00	Normal	0.15	0.75	Lognormal	1.30
3	17.52	0.52	Normal	110.43	10.00	Normal	0.20	0.10	Lognormal	3.56
4	11.13	0.92	Normal	65.49	15.00	Normal	0.15	0.75	Lognormal	7.39

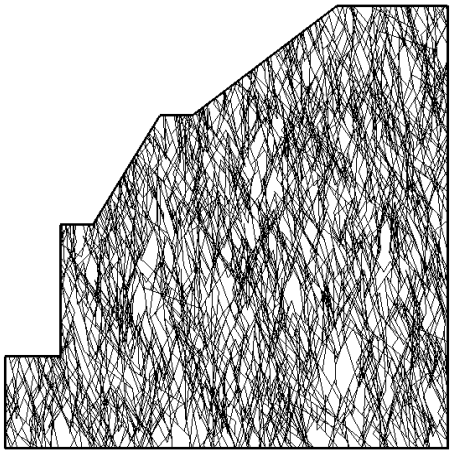

Figure 5.12 Fracture system in the rock slope

Suppose that the water levels of the right and left boundaries of the slope are 200m and 62.2m respectively. The bottom boundary of the model is assumed to be impermeable. The rest boundaries, including the drainage tunnels located in the slope, are taken as the seepage faces satisfying the Signorini's complementary condition.

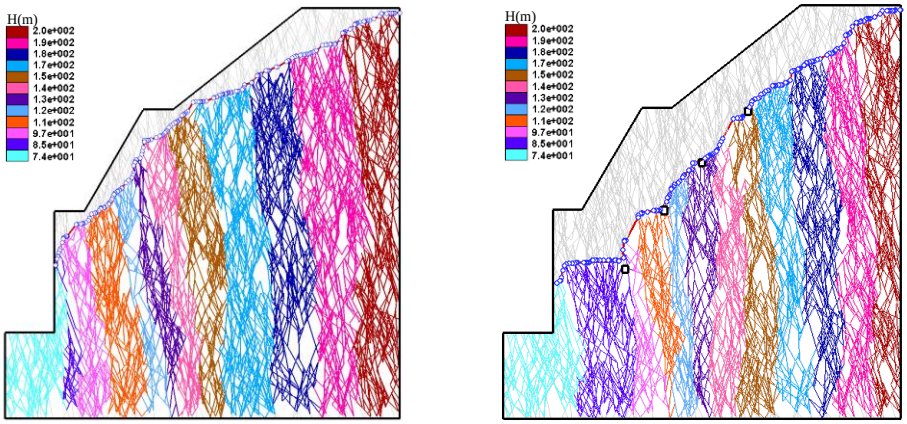

(a) without drainage tunnels (b) with drainage tunnels.

Figure 5.13 Locations of the free surfaces and the water head contours in the rock slope

Figure 5.13a and Figure 5.13b show the locations of the free surfaces and the distributions of water head contours with and without drainage tunnels in the slope, respectively. We can observe from Figure 13 that the water head contours decrease gradually from the right boundary to the left boundary, which accords with the general physical rules. A comparison between Figure 5.13a and Figure 5.13b illustrates that the drainage tunnels have a remarkable impact on the water flow and can obviously lower the free surface, leading to an obvious decrease of seepage pressure on the seepage surface.

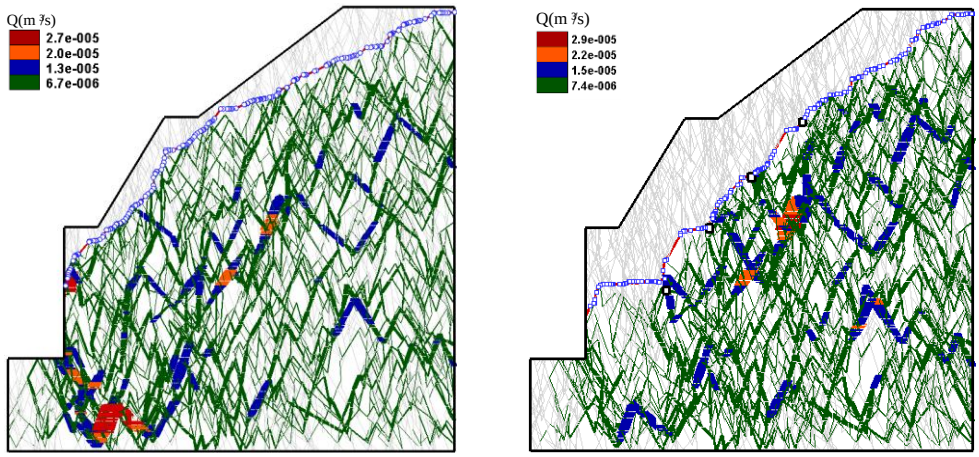

(a) without drainage tunnels (b) with drainage tunnels

Figure 5.14 The flow rate distribution in the slope

Shown in Figure 5.14 are the flow rate distribution inside the slope with and without drainage tunnels. It can be observed from Figure 5.14 that the seepage flow behaviors within the fracture network are heterogeneous. A comparison between Figure 5.14a and Figure 5.14b shows that when the drainage tunnels are deployed, the flow rate distribution in the deeper locations of the slope has no obvious variation, while the flow rates of the fractures on the downstream seepage surface decrease obviously and the flow rates of the fractures near the drainage tunnels increases significantly. The flow rates per unit width through the upstream and downstream surfaces and out of the drainage tunnels are listed in Table 5.4. The total flow rates out of the slope are $7.635\times10^{-5}\,m^3/s$ without the drainage tunnels. After the drainage tunnels are deployed, the total flow rates out of the slope are $10.4\times10^{-5}\,m^3/s$, with the flow rates from the drainage tunnels being $7.565\times10^{-5}\,m^3/s$ and the flow rates at the seepage surface being $2.835\times10^{-5}\,m^3/s$. The total flow rates out of the slope are dramatically increased, while the flow rates at the downstream seepage surface are significantly decreased. Therefore, the drainage tunnels play important functions of drying the slope and lowering the water level of groundwater. It can be further observed from Table 5.4 that the flow rates out of the drainage tunnels are gradually increased from the upstream to downstream. This indicates

that the positions of drainage tunnels have a prominent influence on the effect of the drainage tunnels in drainage, which is very important for design optimization of the drainage system and safety assessment of slope engineering.

Table 5.4 Flow rates per unit width through the upstream and downstream surfaces and out of the drainage tunnels (unit: 10-5 m3/s)

Conditions	Upstream surface	Drainage tunnels				Downstream surface
		1#	2#	3#	4#	
Without drainage tunnels	7.635	-	-	-	-	7.635
With drainage tunnels	10.400	3.066	2.532	1.654	0.313	2.835

5.7 Conclusions

The problem of groundwater seepage through fractured rock is complex due to the existences of free surfaces and seepage surfaces. In this study, the PDEs defined on the whole fracture network are formulated for free-surface seepage problems. A VI formulation equivalent to the PDE formulation is then proposed, and corresponding numerical procedure has been developed. Based on this work, the following main conclusions can be drawn:

1. By specifying the seepage face boundary as a Signorini-type condition, the proposed VI method can effectively eliminate the singularity of seepage points. Based on the VI method, a numerical procedure for unconfined seepage analysis of fracture networks is developed by using line elements in FEM to simulate the fractures. The effectiveness of the procedure is verified by comparison of numerical results and the empirical solutions from a homogeneous rectangular dam.

2. Analysis of the DFN model from the DECOVALEX project indicates that when the aperture variation among fractures is considered, seepage flow becomes more heterogeneous than in the case of constant aperture. This example also exhibits the capability of the proposed model to account for very complicated fracture networks.

3. The proposed model is applied to predict the free-surface seepage behavior through a fractured rock slope with four drainage tunnels. The redistribution of flow rate after the installation of drainage system is accurately modeled, and the effect of each drainage tunnel is precisely analyzed. The simulation in this paper may provide a new insight for performance assessments and design optimization of complex drainage system.

References

[1] Alt, H. W. (1980), Numerical solution of steady-state porous flow free boundary problems, Numer. Math., 31, 73-98.

[2] Andersson, J., and B. Dverstorp (1987), Conditional simulation of fluid flow in three-dimensional networks of discrete fractures, Water Resour. Res., 23(10), 1876-1886.

[3] Baghbanan, A., and L. Jing (2007), Hydraulic properties of fractured rock masses with correlated fracture length and aperture, Int. J. Rock Mech. Min. Sci., 44(5), 704-719.

[4] Bathe, K. J., and M. R. Khoshgoftaar (1979), Finite element free surface seepage analysis without mesh iteration, Int. J. Nume.r Anal. Meth. Geomech. 3, 13-22.

[5] Berkowitz, B. (2002), Characterizing flow and transport in fractured geological media: A review, Adv. Water Resour., 25, 861-884.

[6] Brezis, H., D. Kinderlehrer, and G. Stampacchia (1978), Sur une nouvelle formulation due probleme de l'ecoulement a travers une digue, Comptes Rendus de l'Academie des Sciences Paris Series A, 287, 711-714

[7] Cacas, M. C., E. Ledoux, G. de Marsily, B. Tillie, A. Barbreau, E. Durand, B. Feuga, and P. Peaudecerf (1990), Modeling fracture flow with a stochastic discrete fracture network: calibration and validation 1. The flow model, Water Resour. Res. 26(3), 479-489.

[8] Desai, C. S., and G. C. Li (1983), A residual flow procedure and application for free surface flow in porous media, Adv. Water Resour., 6, 27-35.

[9] Dershowitz, W. S., and H. H. Einstein (1987), Three dimensional flow modeling in jointed rock masses, In: Herget, Vongpaisal, editors. Proceedings of the sixth international congress on rock mechanics, vol. 1., Rotterdam, Balkema, pp. 87-92.

[10] Duiguid, J. O., and P. C. Y. Lee (1977), Flow in fractured porous media, Water Resour. Res., 13(3), 25-28.

[11] Finn, W. D. L. (1967), Finite-element analysis of seepage through dams, J. Soil Mech. Foundat. Div., ASCE, 93(SM6), 41–48.

[12] Hsieh, P. A., and S. P. Neuman (1985), Field determination of the three dimensional hydraulic conductivity tensor of anisotropic media-1. Theory, Water Resour. Res., 21(11), 1655-1665.

[13] Jackson, C. P., A. R. Hoch, and S. Todman (2000), Self-consistency of a heterogeneous continuum porous medium representation of a fractured medium, Water Resour. Res.,

36(1), 189-202.

[14] Jing, L., Y. Ma, and Z. Fang (2001), Modeling of fluid flow and solid deformation for fractured rocks with discontinuous deformation analysis (DDA) method, Int. J. Rock Mech. Min. Sci., 38(3), 343-355.

[15] Kikuchi, N. (1977), An analysis of the variational inequalities of seepage flow by finite-element methods, Quart. Appl. Math., 35, 149-63.

[16] Lacy, S. J., and J. H. Prevost (1987), Flow through porous media: a procedure for locating the free surface. Int. J. Numer. Anal. Meth. Geomech., 11, 585-601.

[17] Long, J. C. S., P. Gilmour, and P. A. Witherspoon (1985), A method for steady fluid flow in random three-dimensional networks of disc-shaped fractures, Water Resour. Res. 21(8), 1105-1115.

[18] Long, J. C. S., J. S. Remer, C. R. Wilson, and P. A. Witherspoon (1982), Porous media equivalents for networks of discontinuous fractures, Water Resour. Res., 18(3), 645-658.

[19] Min, K. B., L. Jing, O. Stephansson (2004), Determining the equivalent permeability tensor for fractured rock masses using a stochastic REV approach: method and application to the field data from Sellafield UK, Hydrogeol. J., 12(5), 497-510.

[20] Neuman, S. P., and P. A. Witherspoon (1970), Finite element method of analyzing steady seepage with a free surface, Water Resour. Res., 6(3), 889-897.

[21] Oda, M. (1985), Permeability tensor for discontinuous rock masses, Geotechnique, 35(4), 483-495.

[22] Oda, M. (1986), An equivalent continuum model for coupled stress and fluid flow analysis in jointed rock masses, Water Resour. Res., 22 (13), 1845-1856.

[23] Oden, J. T., and N. Kikuchi (1980), Recent advances: theory of variational inequalities with applications to problems of flow through porous media, Int. J. Eng. Sci.18, 1173-1284.

[24] Schwartz, F. W., W. L. Smith, and A. S. Crowe (1983), A stochastic analysis of microscopic dispersion in fractured media, Water Resour. Res. 19(5), 1253-1265.

[25] Snow, D. T. (1969), Anisotropic permeability of fractured media, Water Resour. Res., 5(6), 1273-1289.

[26] Streltsova, T. D. (1981), Hydrodynamics of groundwater flow in a fractured formation, Water Resour. Res. 17(4), 21-22.

[27] Taylor, R. L., and C. B. Brown (1967), Darcy flow solutions with a free surface, J. Hydr. Div., ASCE, 93, 25-33.

[28] Westbrook, D. R. (1985), Analysis of inequalities and residual flow procedures and an iterative scheme for free surface seepage, Int. J. Numer. Meth. Eng. 21, 1791-1802.

[29] Wilson, C. R., and P. A. Witherspoon (1974), Steady state flow in rigid networks of fractures, Water Resour. Res., 10(2), 328-335.

[30] Zhang, Y. T., P. Chen, L. Wang (1988), Initial flow method for seepage analysis with free surface, Journal of Hydraulic Engineering, 8(1), 18-26.

[31] Zhang, Y. T. (1999), Water pressure of high rock slope and the permanent shiplock, in *Deformation and stability of high rock slope*, edited by Y. T. Zhang and W. Y. Zhou, pp. 76, China Water Power Press, Beijing.

[32] Zheng, T. S., L. Li, and Q. Y. Xu (1995), An iterative method for the discrete problems of class of elliptical variational inequalities, Applied Mathematics and Mechanics, 16(4), 351-358.

[33] Zheng, H., D. F. Liu, C. F. Lee, L. G. Tham (2005), A new formulation of Signorini's type for seepage problems with free surfaces, Int. J. Numer. Meth. Eng., 64, 1-16.

[34] Zhou, C. B., W. L. Xiong, and Y. G. Liang (1996), A new method for unconfined seepage field, J. Hydrodyn., Ser. A, 11(5), 528-534.

Chapter 6 Seepage flow with free surface in Three dimensional fracture networks

6.1 Introduction

In some large rock engineering projects, such as excavation of high and steep rock slopes, exploitation of oil in fractured reservoirs and repositories of nuclear wastes, underground flow plays a significant role in assessment of performance and security. As a result, seepage problem in fractured rocks has become a vital topic in the field of hydro-geology and rock engineering [1].

Relative to rock matrix, permeability of fractures are very high. Thus, they constitute main channels for underground flow. Due to the uneven distribution of permeability in single fracture and fracture networks, some distinct features are often observed in flow behaviors of fracture networks, i.e. “channeling flow” and “preferential flow”[2,3].

Many numerical models have been put forth to study seepage problems in fractured rocks. These models can be roughly categorized into two groups: equivalent continuum model and discrete fracture network model. Equivalent continuum models are based on the concept of REV (Representative Element Volume) [4,5,6]. A REV is a continuum volume with a permeability equivalent to the fracture network, defined by use of a spatial homogenization technique. With efficiency and capacity in modeling large scale problems, continuum models have been well developed and been widely used in practice. However, for fracture networks that exhibit scaling behavior do not possess any homogenization scale, a representative elementary volume (REV) cannot be defined. This suggests limitation on utility of such continuum models.

In discrete fracture network models, fractures are explicitly simulated. Complex flow behaviors induced by distribution and connectivity of fracture networks can be accurately described in a simple manner. In spite of its computational limitation in dealing with large scale problems, this kind of model has still favored a well development in theoretical studies and practical applications [7,8].

In discrete fracture network model, a fracture is usually modeled as a plane with various shapes and a finite size. To avoid the complex geometry calculation of intersections, many researchers used a channel joining two single fracture centers to represent their intersection relationship [9,10,11]. Although this kind of capillary model has the capacity to

depict “channeling flow” and permeability heterogeneity, spatial characteristics of fracture network is not really taken into account.

To the best of our knowledge, only a few flow models are among those truly considers the complex topology of three dimensional fracture networks, such as a boundary element model proposed by Andersson [12], and a finite volume model firstly proposed by Koudina [13] and then proposed by Khamforoush [14] and Mourzenko [15]. The main focus of these models is to determine the permeability of a fracture system and numerical experiments were carried out under confined condition. Underground flow with a free surface was not mentioned in these researches. Nevertheless, the location of free surface is usually a key factor influencing the stability of some rock engineering, especially of high and steep rock slope in sites with complex hydro-geological conditions. Therefore, it is very needy to develop a numerical model on seepage problem in fracture networks with a free surface.

Seepage problems with free surfaces have been well studied in continuum models and many good methods have been proposed[16,17,18]. In discrete fracture network models, however, only a few studies have been carried out and most of them are on two dimensional problems [19,20,21,22,23]. Among them, the variation inequality method proposed by Jiang[23] is a new advance in research of unconfined seepage problem in fracture network. Rigorous in mathematics, this method successfully solves the singularity problem of seepage points and is very applicable for random fracture networks with complex geometries.

For seepage problem with free surface in real three dimensional fracture networks, to the authors’ knowledge, only Zhang[24] have proposed a numerical model based on the initial flow method. This model replaced the distributed fracture network with a few groups of equivalent penetrated fractures. It greatly reduced the difficulty in preprocessing by avoiding the complexity of topology, but at the same time, lost advantages of DFN model in precise description of flow behaviors.

The very aim of this study is to propose a numerical model on seepage problem with free surface in fractured rocks that can realistically take into account the complex topology of fracture networks. Tracing the thinking of Jiang[23], a generalized Darcy’s Law and the boundary of Signorini’s type are firstly introduced to establish a partial differential equation formulation (PDE) defined on the whole domain. Then, a vibrational inequality formulation equivalent to the PDE formulation is found, making numerical solution much more convenient. Finally, combined with penalized Heaviside function, a discretized finite

element procedure is formulated. Compared to the initial flow method[24], the proposed model is more rigorous in mathematics and with the introduction of the boundary of Signorini's type and the penalized Heaviside function, the singularity of seepage points is eliminated and the robustness of program is stimulated.

The mesh used for numerical analysis is obtained in the following way: Firstly, generate fractures with polygonal shape in three dimensional space using Monte Carlo method according to specific distributions of fracture geometries; Then, search for a connected fracture network by deleting the isolated and single connected fractures with the space block search technology[25,26]; Finally, triangulate the fracture network. An example of the final mesh is illustrated in fig. 6.6.

6.2 Seepage problem with free surface in 3-d fracture network

6.2.1 PDE formulation

For sake of convenience, we take the steady seepage flow through a 2-d fractured rock slope in Figure 6.1 as an example. For the seepage problem with free surface in domain Ω （$\Omega=\Omega_w\cup\Omega_d$）, underground water actually flows only in the wet domain Ω_w below a free surface Γ_f. Suppose that the upstream water level is located at point ***A***, the downstream at point ***D***, ***BC*** is an impermeable boundary, ***E*** is the seepage point, and ***AE*** is the free surface consists of the zero pressure water table in the discrete fractures.

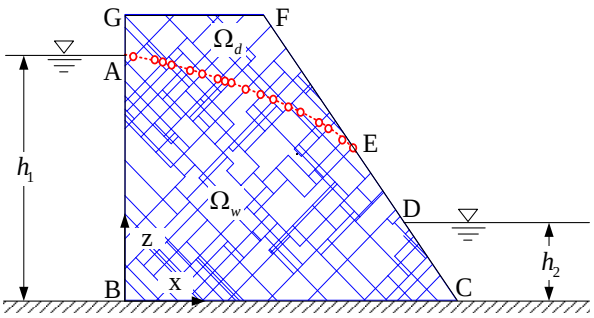

Figure 6.1 Illustration of unconfined seepage problem for fracture network

Assuming that flow only occurs in fractures and two planes are smooth and parallel to each other, according to the cubic law, permeability of a single fracture k can be represented by its hydraulic aperture b as

$$k=\frac{gb^2}{12\upsilon} \tag{6-1}$$

In which，g is the gravity acceleration and υ is the kinematic viscous parameter of water.

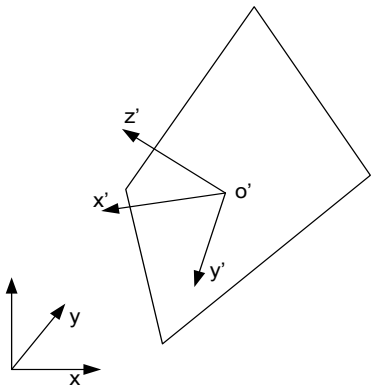

Figure 6.2 Local coordinate system for a single fracture

Flow in 3-d fracture network can be simplified as a 2-d problem on fracture planes. Illustrated in Figure 6.2 is a local coordinate system $x'y'$ defined on a fracture plane. Based on the extended Darcy's law given by Jiang[23], velocity of an arbitrary point defined on the whole domain of fracture network can be expressed as,

$$v = -k_{\varepsilon}\nabla\phi \tag{6-2}$$

In which, ϕ is the total head of the point, k^{ε} is permeability defined on the whole domain of fracture network,

$$k_{\varepsilon} = H_{\varepsilon}(\phi - z)k \tag{6-3}$$

where,

$$H_{\varepsilon}(\phi - z) = \begin{cases} 1 & if\ \ \phi \geq z\ \ (in\ \ \Omega_w) \\ \varepsilon & if\ \ \phi < z\ \ (in\ \ \Omega_d) \end{cases} \tag{6-4}$$

ε is penalized parameter to penalize Heaviside function, when $\varepsilon \to 0$, $H_{\varepsilon}(\phi - z)$ tends to be the original Heaviside function.

According to the conservative condition, the following equation should be satisfied,

$$\nabla v = \frac{\partial^2 \phi}{\partial x'^2} + \frac{\partial^2 \phi}{\partial y'^2} = 0 \tag{6-5}$$

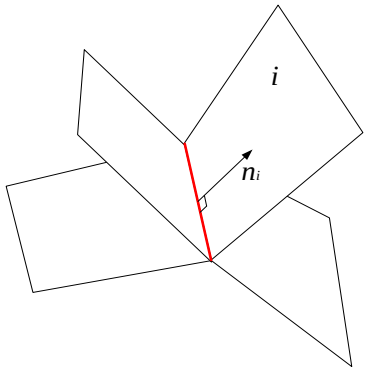

Figure 6.3 Illustration of interaction between fractures

Suppose that an intersection, which is illustrated as a red line in Figure 6.3, is a

common boundary shared by m fracture planes, ignoring its capacity of water storage and considering the condition of mass conservation, the following equation stands for any point on this intersection,

$$\sum_{i=1}^{m} q_{ni} = 0 \qquad (6\text{-}6)$$

Where, q_{ni} is the flow rate into fracture i through this point, expressed as

$$q_{ni} = -b_i k_i \frac{\partial \phi}{\partial n_i} \qquad (6\text{-}7)$$

In which, b_i, k_i are respectively the hydraulic aperture and permeability of the fracture i, n_i is a vector pointing to fracture i, which is proportional to fracture i whilst perpendicular to the intersection, as illustrated in figure 6.3.

Still the following boundary conditions needs to be satisfied:

(1)The condition on the water head boundary

$$\phi = \bar{\phi} \ (\text{on} \ \ \Gamma_\phi = \text{AB} + \text{CD}) \qquad (6\text{-}8)$$

Where, $\bar{\phi}$ is the known water head defined on the boundary Γ_ϕ, equals to h_1 and h_2 respectively on the upstream and downstream boundary.

(2) The condition on the flux boundary

$$q = bv = 0 \ （\text{on} \ \ \Gamma_q = \text{BC}） \qquad (6\text{-}9)$$

Where, Γ_q is an impermeable boundary.

(3) The Condition of complementary boundary of Signorini's type，

$$\begin{cases} \phi \le z, q \le 0 \\ (\phi - z)q = 0 \end{cases}, （\text{on} \ \ \Gamma_s = \text{AGFD}） \qquad (6\text{-}10)$$

So far, we have established a PDE formulation for the boundary value problem defined on the whole fracture network. The solution of this problem is to find a function ϕ, which satisfies the controlling equations (6-5) and (6-6), and the boundary conditions (6-8), (6-9) and (6-10) at the same time.

6.2.2 Equivalent variational inequality formulation

Due to the presence of internal free boundary and the potential seepage surface, when solving the PDE formulation defined on the whole domain, it is difficult to find a proper trial function. However, a VI formulation equivalent to the PDE formulation does not have such disadvantages. By transforming internal free boundary and the complementary boundary into a natural boundary, the VI formulation can effectively reduce numerical

difficulty and improve numerical stability and convergence.

Given a trial function set Φ_{VI},

$$\Phi_{VI} = \left\{ \varphi \mid \varphi = \bar{\phi}, \text{ on } \Gamma_{\phi}; \varphi \le z, \text{ on } \Gamma_s \right\} \tag{6-11}$$

The VI formulation equivalent to the PDE formulation can be represented as: find a function ϕ in Φ_{VI}, so that for $\forall \psi \in \Phi_{VI}$, there holds

$$a(\phi, \psi - \phi) \ge 0 \tag{6-12}$$

In which, $$a(\phi, \psi - \phi) = \sum_{\Omega} \iint_i \nabla (\psi - \phi) b_i H_{\varepsilon} k_i \nabla \phi dx\, dy' \tag{6-13}$$

To prove the equivalence between the PDE formulation and the VI formulation, firstly we need to use Green's formula to expand equation (6-13):

$$\begin{aligned} & a(\phi, \psi - \phi) \\ & = -\sum_{\Omega} \iint_i \nabla (\psi - \phi) b_i v dx' dy' \\ & = \sum_{\Omega} \left(-\oint_i (\psi - \phi) q_n ds + \iint_i (\psi - \phi) b_i \nabla v dx' dy' \right) \\ & = \sum_{i=1}^{N} \sum_{j=1}^{m_i} \int_{l_i} (\psi - \phi) q_{nj} dl_i + \sum_{i=1}^{M} \iint_i (\psi - \phi) b_i \nabla v dx' dy' \end{aligned} \tag{6-14}$$

Where, N denotes the total number of intersections, m_i denotes the number of fracture planes connecting to the intersection i, M is the total number of fracture planes. The remaining proof is almost the same as Jiang[23], thus not repeated here.

6.3 Finite element formulation

6.3.1 Adaptive penalized Heaviside function

To avoid numerical oscillations induced by the discontinuity of Heaviside function, a penalized Heaviside function[23] is used, which is continuous and expressed as

$$H_{\varepsilon}^{\lambda}(\phi - z) = \begin{cases} \varepsilon & if \quad \phi - z \le -\lambda \\ \frac{(1+\varepsilon)\lambda + (1-\varepsilon)(\phi - z)}{2\lambda} & if \quad -\lambda < \phi - z < \lambda \\ 1 & if \quad \phi - z \ge \lambda \end{cases} \tag{6-15}$$

Where, λ is a characteristic length of a finite element.

6.3.2 Finite element formulation

In this study, triangle is used as the basic element type. By using linear interpolation,

the hydraulic potential function on any element can be represented by total heads of the three vertices[27], such that

$$\phi = N_i\phi_i + N_j\phi_j + N_m\phi_m \tag{6-16}$$

Where, *i, j, k* are indexes of the vertices, N_i, N_j, N_k are shape functions.

Adopting finite element approximation to Equation (6-12), the discrete form of the VI is stated as follows: seek a water head vector $\boldsymbol{\phi}^{r+1} \in \Phi_{VI}^h$,

$$\Phi_{VI}^{\phi} = \{\varphi \mid \varphi \in R^n; \varphi_i = \bar{\phi}_i, i \in \Gamma_{\phi}; \varphi_i \le z_i, i \in \Gamma_s\} \tag{6-17}$$

for $\forall \boldsymbol{\psi} \in \Phi_{VI}^h$, there always holds,

$$(\boldsymbol{\psi} - \boldsymbol{\phi}^{r+1})^{\mathrm{T}} \boldsymbol{K}^r \boldsymbol{\phi}^{r+1} \ge 0, \quad r = 1, 2\cdots \tag{6-18}$$

in which,

$$\boldsymbol{K}^r = \sum_{\Omega} \boldsymbol{K}_e^r \tag{6-19}$$

$$\boldsymbol{K}_e^r = \iint_e \boldsymbol{H}_{\varepsilon}(\phi^r - \boldsymbol{z})\boldsymbol{B}^{\mathrm{T}} b_e k_e \boldsymbol{B} dx' dy' \tag{6-20}$$

$$\boldsymbol{B} = \begin{bmatrix} \dfrac{\partial N_i}{\partial x'} & \dfrac{\partial N_j}{\partial x'} & \dfrac{\partial N_m}{\partial x'} \\ \dfrac{\partial N_i}{\partial y'} & \dfrac{\partial N_j}{\partial y'} & \dfrac{\partial N_m}{\partial y'} \end{bmatrix} \tag{6-21}$$

Where, r denotes iteration step. There are many algorithms for such VI formulation, in this paper, an algorithm proposed by Zheng[17] is adopted.

6.4 Examples

6.4.1 Case 1：A homogeneous rectangular dam

In this example, we use three groups of evenly distributed orthogonal fractures to model a homogeneous rectangular dam. Illustrated in Figure 6.4 are these fractures after triangulation. The size of this model is 10m×4m×12m. The spacing for the two groups which are perpendicular to the plane of *x*-*z* is 0.2m, for the one parallel is 1m. The plane on which x=0*m* and x=10*m* are respectively upstream boundary and downstream boundary, and with water head 10*m* and 2*m*. Hydraulic aperture is set to be 1*e*-4*m*for all fractures. Pressure contours analyzed by the proposed model are interpreted in Figure 6.4.

Fractures perpendicular to the plane of x-z are very dense. As a result, permeability parallel to this plane is relatively very high. In the direction parallel to the plane x-z，this numerical model can be considered as a homogeneous media. For this case，the analytical

solution is expressed as[18]

$$z = (100 - 8x)^{1/2} \tag{6-23}$$

Comparison of free surface location between numerical simulation and analytical solution is shown in Figure 6.5. A good agreement between them can be observed and the seepage points almost coincide with each other, demonstrating that the proposed model can accurately locate the free surface in fracture networks.

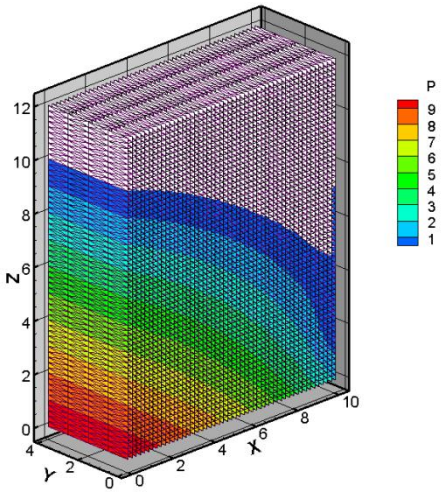

Figure 6.4 Mesh and pressure contour of a homogeneous rectangular dam

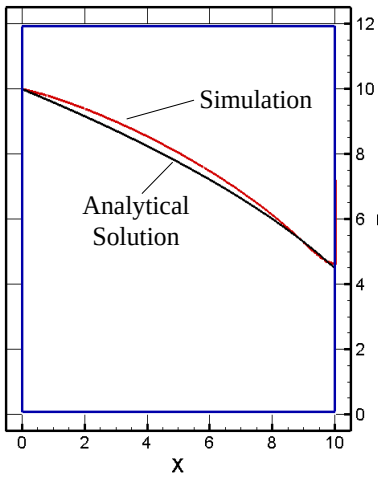

Figure 6.5 Comparison of free surface location between numerical simulation and analytical solution

6.4.2 Case 2: fracture network with complex geometries

A few sets of fractures are randomly distributed in a hexahedron with a size of $100m \times 100m \times 150m$. Geometric parameters and distribution parameters for these fractures

are listed in table 1, mesh of the fracture network after triangulation is illustrated in Figure 6.6. The two planes x=0 and x=150 are respectively the upstream boundary and the downstream boundary, corresponding water level of which are 100m and 50m. No variance of hydraulic aperture is considered here and is all set as 1e-4m.

Table 6.1 Parameters of fractures and probability models for example 2

Set	Orientation (Deg)			Dips (Deg)			Trace length (m)			Spacing (m)		
	Mean	Var.	Dis.	Mean	Var.	Dis.	mean	Var.	Dis.	mean	Var.	Dis.
1	90	40	Normal	75	10	Normal	40	40	Ne. Exp.	5	5	Ne. Exp.
2	120	20	Normal	60	20	Normal	30	30	Ne. Exp.	5	5	Ne. Exp.
3	140	10	Normal	20	12.5	Normal	60	40	Ne. Exp.	5	6	Ne. Exp.
4	240	40	Normal	45	30	Normal	40	30	Ne. Exp.	5	8	Ne. Exp.

Illustrated in Figure 6.7a and Figure 6.7b are graphs of pressure contours observed from different perspectives. For sake of a clear demonstration, fractures above the free surface are not shown. Viewed from the right side (Figure 6.7a), there exists large voids in the fracture network, and some local fracture planes are in poor connectivity; Viewed from a certain angle from the space (Figure 6.7b), in the vicinity of the free surface, fractures intersects with each other in a very disorganized manner, showing that spatial structures are very complex in geometry. Overall, however, the water pressure gradually increases from top to bottom, the transition is smooth, and there are no significant mutations. These are consistent with the general observation, demonstrating the applicability of the proposed model to the fracture network with complex spatial geometry.

Illustrated in Figure 6.8a and Figure 6.8b are respectively graphs of flow rate distribution on the upstream boundary and downstream boundary, in which, black line represents traces cut by fractures on the boundary. As are shown, water flows in and out all through fractures. Flow rate, however, varies a lot on different fractures and even the same fracture segments. Larger flow rate often occurs at the intersection between fractures, in line with the previous observations [2,3]. Calculation results of this example well depicts the uneven distribution of flow rate and “preferential flow”due to the structure of fracture network, which are often encountered in practice.

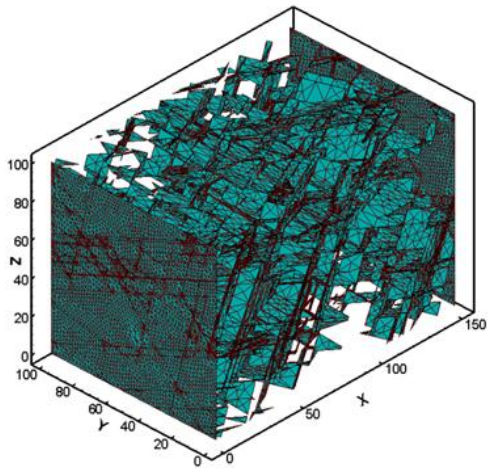

Figure 6.6　Fracture network of case 2 after triangulation

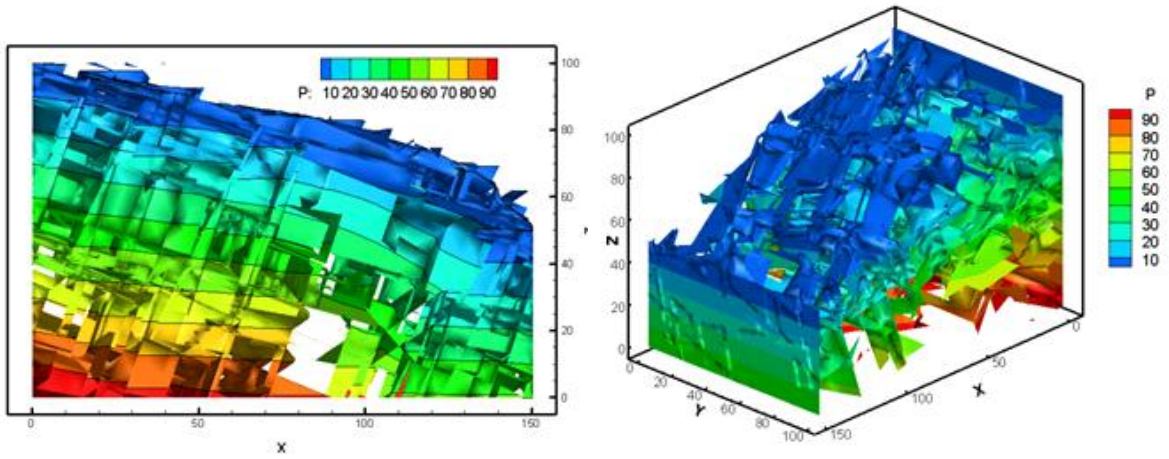

（a）Pressure contours obtained from *y* direction　（b）Pressure contours obtained from some spatial orientation

Figure 6.7　Pressure contours for case 2

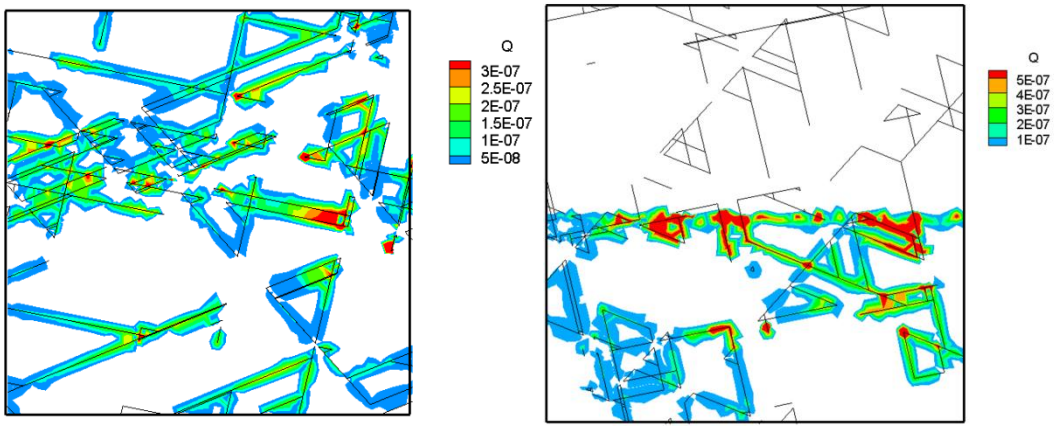

(a) Flow rate distribution on flowing-in surface　(b) Flow rate distribution on flowing-out surface

Figure 6.8　Flow rate distribution on upstream and downstream boundary surfaces (unit：m^3/s)

6.5 Conclusion

In this study, the vibrational inequality based initial flow method for unconfined seepage problem in fracture network has been extended from 2-d problem to 3-d problem, the finite element procedure is established and the corresponding program is developed. Some basic conclusions can be drawn:

(1) Through introduction of the generalized Darcy's law and the boundary of Signorini's type, a PDE formulation defined on the whole domain is established. To solve this problem, a VI formulation equivalent to the PDE formulation is adopted and the finite element procedure is developed with a combination of the adaptive penalized Heaviside function.

(2) Using three sets of evenly distributed orthogonal fractures to model a homogeneous rectangular dam, a typical example in unconfined seepage problem is analyzed. The location of free surface and seepage point are both in good agreement with the empirical formula, verifying the validity of the proposed model.

(3) Analysis of unconfined seepage problem is carried out on a complex random fracture network. Results show that water pressure gradually decreases from top to down with a smooth transition. Although all hydraulic apertures are set to the same, a strong inhomogeneity of flow rate, due to fracture distribution and connectivity, is still observed on the upstream and downstream boundary, and the phenomenon of "preferential flow" is easily captured.

References

[1] Berkowitz B. Characterizing flow and transport in fractured geological media: a review[J]. Adv Water Resour, 2002, 25(8):3861–84.

[2] Neretnieks I, Eriksen T, Tahtinen P. Tracer movement in a singlefissure in granitic rock: some experimental results and theirinterpretation[J]. Water Resour Res 1982;18(4):849–58.

[3] Neretnieks I. Solute transport in fracture rock—Applications toradionuclide waste repositories. In: Bear J, Tsang CF, de MarsilyG, editors. Flow and contaminant transport in fractured rock.San Diego: Academic Press, Inc; 1993. p. 39–127.

[4] Oda, M. (1985), Permeability tensor for discontinuous rock masses, Geotechnique, 35(4), 483-495.

[5] Oda, M. (1986), An equivalent continuum model for coupled stress and fluid flow

analysis in jointed rock masses, Water Resour. Res., 22 (13), 1845-1856.

[6] Neuman, S. P. (1973), Saturated-unsaturated seepage by finite elements. Journal of the Hydraulics Division, 99(12), 2233–2250.

[7] Sahimi M. Flow and transport in porous media and fracturedrock: from classical methods to modern approaches. Weinheim,Germany: VCH; 1995.

[8] Adler PM, Thovert JF. Fractures and fracture networks. Netherlands:Kluwer Academic Publishers; 1999.

[9] M. C. Cacas, E. Ledoux, G. de Marsily, A. Barbreau, P. Calmels, B. Gaillard, and R. Margritta, "Modeling fracture flow with a stochastic discrete fracture network: Calibration and validation: 2. The transport model", Water Resources Research, vol 26, no 3, pp 491–500, 1990.

[10] W. Nordqvist, Y. W. Tsang, C. F. Tsang, B. Dverstorp, and J. Andersson, "A variable aperture fracture network model for flow and transport in fractured rocks", Water Resources Research, vol 28, no 6, pp 1703–1713, 1992.

[11] Rouleau and J. E. Gale, "Stochastic discrete fracture simulation of groundwater flow into an underground excavation in granite", International Journal of Rock Mechanics and Mining Sciences &Geomechanics Abstracts, vol 24, no 2, pp 99–112, 1987.

[12] J. Andersson and B. Dverstorp, "Conditional simulations of fluid flow in three-dimensional networks of discrete fractures", Water Resources Research, vol 23, no 10, pp 1876–1886, 1987.

[13] N. Koudina, R. Gonzalez Garcia, J.-F. Thovert, and P. M. Adler, "Permeability of three-dimensional fracture networks", Phys. Rev. E, vol 57, no 4, pp 4466–4479, 1998.

[14] M. Khamforoush, K. Shams, J.-F. Thovert, and P. M. Adler, "Permeability and percolation of anisotropic three-dimensional fracture networks", Phys. Rev. E, vol 77, no 5, p 056307, 2008.

[15] V. V. Mourzenko, J.-F. Thovert, and P. M. Adler, "Permeability of isotropic and anisotropic fracture networks, from the percolation threshold to very large densities", Phys. Rev. E, vol 84, no 3, p 036307, 2011.

[16] ZHANG Youtian ,CHEN Ping ,WANG Lei. Initial flow method for seepage analysis with free surface [J] . Journal of Hydraulic Engineering ,1988 ,8 (1) :18～26. (in Chinese)

[17] H. Zheng et al. A new formulation of Signorini's type for seepage problems with free surfaces. International journal for numerical methods in engineering 64, no. 1 (2005): 1-16.

[18] Y. Chen, C. Zhou, and H. Zheng. A numerical solution to seepage problems with complex drainage systems. Computers and Geotechnics 35, no. 3 (2008): 383-393.

[19] WANG Enzhi . Seepage calculation method in fissure networks on vertical section . Hydrogeology & Engineering Geology , 20, no. 4 (1993): 27-29. (in Chinese)

[20] CHAI Junrui, WUYanqing . The method for determination of the position of free surface in fractured rock masses.Geotechnical Investigation &Surveying , no. 1 (2000): 23-24. (in Chinese)

[21] Yao Chi, Jiang Qinghui, Ye Zuyangetc..Thevariationalinequality based initial flow method for unconfined seepage problems of fracture networks[J]. Rock and Soil Mechanics, 2012,33(6):1896-1903.(in Chinese)

[22] Jiang, Q., C. Yao, Z. Ye, and C. Zhou. Seepage flow with free surface in fracture networks. Water Resour. Res., (in press, accepted 12 November 2012)

[23] Q. Jiang, Z. Ye, C. Yao, and C. Zhou, A new variational inequality formulation for unconfined seepage flow through fracture networks, Sci. China Technol. Sci., vol 55, no 11, pp 3090–3101, Nov 2012.

[24] Liu Zhong, Zhang Youtian.Analysis of free surface seepage problems inthree dimensional network of fracture[J]. ShuiliXuebao. 1996, 6: 34-38.(in Chinese)

[25] Zhang Qihua, Wu Aiqing. Three-dimensional arbitrary fracture network seepage model and its solution[J]. Chinese Journal Rock Mechanics and Engineering, 2010,29(4): 720-730 (in Chinese)

[26] Zhang Qihua, Wu Aiqing. General methodology of spatial block topological identification with stochastic discontinuities cutting[J]. Chinese Journal Rock Mechanics and Engineering, 2007, 26(10): 2044-2048 (in Chinese)

[27] MAO Changxi. Seepage Computation Analysis &Control . Beijing: China WaterPowerPress , 2003. (in Chinese)

Chapter 7 Hydro-mechanical Coupling and Solute Transport in Densely Fractured Rock Mass

7.1 Introduction

Due to the practical demand on environmental safety and energy extraction in recent years, some major geotechnical engineering projects were constructed, such as the deep mining, the geological disposal of nuclear waste, and the exploitation of fractured reservoirs, making the characteristics of hydro-mechanical coupling gradually become a hot topic in the field of rock mechanics [1].

In terms of performance assessment of the geological disposal of nuclear waste, nuclide transport through fractured geological body is a major concern. Apart from advection, adsorption of fracture surface, matrix diffusion, chemical reaction with minerals and decay et al all have impacts on transport process of nuclides to varying degrees. Many sites of potential disposal are located in deep fractured crystalline rocks[2], such as granite. Compared to fractures, permeability of rock matrix is negligible, so the flow field is controlled by the fracture network. The conductivity of a fracture is determined by its hydraulic aperture. Larger hydraulic aperture results in larger conductivity. By tension, compression and dilation, stress can significantly change the hydraulic aperture and conductivity of fractures, and then the flow field. The flow field affects the stress and deformation with water pressure on fracture surfaces. Solute transport is mainly affected by flow field. Therefore, hydro-mechanical coupling has a great influence on nuclide transport in fractured geological media.

Due to the technical difficulty in realizing fracture networks in the laboratory, research on hydro-mechanical coupling are now mainly focused on mathematical and numerical models. Based on their assumption, these methods can be roughly divided into two groups: continuum model and discrete element model. The discrete element models explicitly simulates the deformation and flow in rock masses and can easily depict flow anisotropy and heterogeneity due to the random distribution of fractures and their hydraulic apertures. Thus, this kind of models have been well developed in recent years[3~7]. However, examples shown in some studies[3,4] are either regular in block shape or small in fracture amounts, which cannot represent fracture distribution in real situation. Min[5], Baghbanan[6] and Zhao[7] used a random fracture network generated based on statistics

data from site investigation to study effects of stress on flow and transport, but they did not really take into account effects of water pressure on deformation.

Many studies on solute transport have been carried out in a single fracture or complex fracture networks since the 70s, last century[8,9]. Neretnieks[10] presented a fast method for simulation of radionuclide chain migration in dual porosity fracture rocks, which can be easily applied to solute transport problem in complex fracture network.

The rigid block spring method (RBSM) first proposed by Kawai[11] is a kind of discrete element method, which is very suitable for static and small deformation problems. Since fractures are explicitly in this method, it has been widely used in geotechnical engineering[12,13,14]. Combining the rigid block spring method, the discrete fracture network model and the particle tracking method, a numerical model is established for simulation of hydro-mechanical coupling and solute transport in fracture networks. The simplified Barton-Bandis model is employed as constitutive model of fractures, which effectively captures the non-linear normal stress deformation relationship and dilation effects. Coupling between stress and flow are realized by a cross iteration procedure. Finally, the proposed model is applied to a typical fracture network from the Decovalex[18] project. Good agreement between present results and which of previous work made by Zhao[7] is observed.

7.2 Deformation analysis of rock mass: rigid block spring method

7.2.1 Basic theory

Compared to rock fractures, the deformability of rock matrix is negligible. Suppose that rock blocks formed by fracture intersections are rigid, and normal springs and shear springs are uniformly distributed along common interfaces between neighboring blocks, on which all internal energy is restored. There are three degrees of freedom for each block, i.e. displacement of the centroid in x and y direction, respectively u_{cx} and u_{cy}, and a rotation angle θ_c. Assuming that only small rotation occurs, based on the principle of coordinate transformation, displacement of any point $\{u\}$ on interface can be expressed by DOFs of the block's centroid as,

$$\{u\}=[B][N]\{u_c\} \qquad (7\text{-}1)$$

In which，$\{u\}^T=\{u_n\ u_s\}$，denotes normal displacement and shear displacement, $\{u_c\}^T=\{u_{cx}\ u_{cy}\ \theta_c\}$，$[B]$、$[N]$ are respectively coordinate transformation matrix and displacement transformation matrix[19].

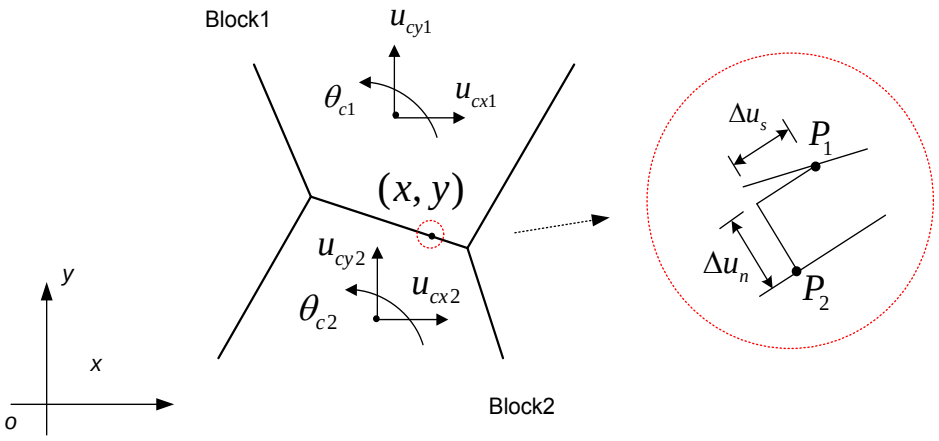

Figure 7.1 Illustration of deformation of interface between two neighboring rigid block

As shown in Figure 7.1 Illustration of deformation of interface between two neighboring rigid blockFigure 7.1, relative displacement of one point on interface can be depicted by displacements of two neighboring blocks as,

$$\{\Delta u\} = [B]([N]_1\{u_c\}_1 - [N]_2\{u_c\}_2)$$
$$= [B][N]_{12}\{u_c\}_{12} \quad (7\text{-}2)$$

In which, $\{\Delta u\}^T = \{\Delta u_n \ \Delta u_s\}$, Δu_n、Δu_s are respectively relative normal and shear displacement.

Stress on interface is expressed by relative displacement as,

$$\{\sigma\} = [D]\{\Delta u\} \quad (7\text{-}3)$$

In which, $\{\sigma\}^T = \{\sigma_n \quad \tau_s\}$, σ_n and τ_s are normal stress and shear stress, $[D] = \begin{bmatrix} k_n & 0 \\ 0 & k_s \end{bmatrix}$, k_n and k_s are normal stiffness and shear stiffness.

Based on the virtual work theorem, there stands[12]

$$\sum_e \left(\int_{l_0^e} \{\delta(\Delta u)\}^T \{\sigma\} dl + \int_{l_\sigma^e} \{\delta u\}^T \{p\} dl + \iint_{s^e} \{\delta u\}^T \{f\} ds \right) = 0 \quad (7\text{-}4)$$

In which, l_0^e、l_σ^e、s^e are respectively interface boundary, force boundary and block domain, $\{\delta u\}$ denotes virtual displacement, $\{\sigma\}$, $\{\delta(\Delta u)\}$ are interface stress and interface virtual relative displacement, $\{p\}$ denotes loading stress, $\{f\}$ is body force.

Substituting equation (7-1), (7-2) and (7-3) to equation (7-4),

$$-\{\delta U\}^T \left(\sum_e \left(\int_{l_0^e} [N]_{12}^T [B]^T [D][B][N]_{12} dl \right) \right) \{U\}$$
$$= \{\delta U\}^T \sum_e \left(\int_{l_\sigma^e} [N]^T [B]^T \{p\} dl \right) \quad (7\text{-}6)$$

In which, $\{\delta U\}$ is global virtual displacement vector, $\{U\}$ is global block displacement vector, eliminating $\{\delta U\}$, the global equilibrium equations can be obtained,

$$[K]\{U\}=\{Q\} \tag{7-7}$$

in which, $[K]=-\left(\sum_e\left(\int_{l_0^e}[N]_{12}^T[B]^T[D][B][N]_{12}dl\right)\right)$,

$$\{Q\}=\sum_e\left(\int_{l_\sigma^e}[N]^T[B]^T\{p\}dl\right)$$

Procedure proposed by Wang[19] is adopted to treat boundary conditions.

7.2.2 Non-linear constitutive model for rock fractures

In traditional RBSM methods, linear constitutive models of fractures are often employed[11～14]. This kind of models cannot reflect nonlinear relationship between normal stress and displacement, thus are not suitable for HM coupling analysis which is sensitive to hydraulic aperture. To precisely describe fracture deformation under stress, a simplified Barton-Bandis model[5] is adopted, this model comprises of three parts: a step linear relation between normal stress and normal deformation (Figure 7.2a), a perfect elasto plastic relation between shear stress and shear deformation (Figure 7.2b), and dilation effect (Figure 7.2c).

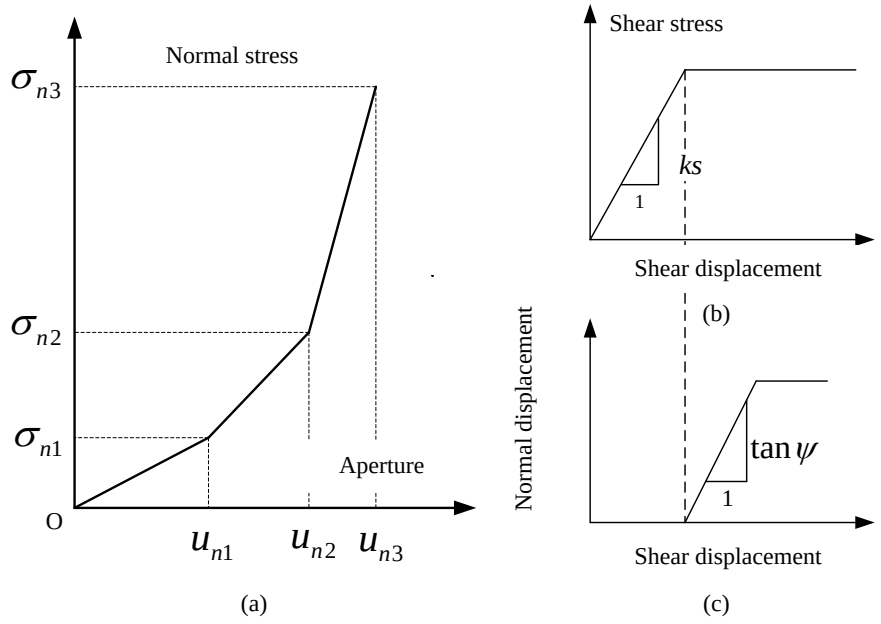

Figure 7.2 Simplified Barton Bandis Model

This model can be interpreted in a framework similar to classic elasto-plastic theory. Here, tangential and normal deformation of fractures are divided into elastic and plastic

deformation, expressed as,

$$\{\Delta u\} = \{\Delta u\}^e + \{\Delta u\}^p \quad (7\text{-}8)$$

in which, $\{\Delta u\} = \{\Delta u_n \quad \Delta u_s\}^T$, $\{\Delta u\}^e = \{\Delta u_n^e \quad \Delta u_s^e\}^T$, $\{\Delta u\}^p = \{\Delta u_n^p \quad \Delta u_s^p\}^T$. $\{\Delta u\}^e$ is elastic deformation, denoting the part of relative normal and tangential displacement which contribute to normal stress and shear stress, $\{\Delta u\}^p$ denotes relative normal displacement induced by dilation and relative tangential displacement caused by sliding.

There requires four conditions to solve an elastic- perfect plastic problem, i.e. incremental stress-strain relationship, flow rule, yield conditions and the consistency condition. Similar to this, the simplified Barton Bandis model can be described as,

(1) Incremental stress-deformation relationship（Figure 7.2a，b）

$$\left\{\Delta\sigma\right\} = \left[D\right]\left\{\Delta u^e\right\} \quad (7\text{-}9)$$

in which,[*D*] is the step linear stiffness coefficient matrix. The step linear stiffness coefficient is divided into three values in terms of the normal elastic deformation，each of which is determined by σ_{n1}, σ_{n2}, σ_{n3}, u_{n1}, u_{n2} and u_{n3}, as shown in Figure 7.2(a).

(2) Non-associated flow rule

Dilation occurs as sliding takes place, the effect of which is expressed as

$$\Delta u_n^p = \mid \Delta u_s^p \mid \cdot \tan\psi \quad (7\text{-}10)$$

In which, ψ is the dilation angle. The relation above can be expressed in terms of the classical non-associated flow rule as

$$\left\{\Delta u^p\right\} = \lambda \begin{Bmatrix} \tan\psi \\ \pm 1 \end{Bmatrix} \quad (7\text{-}11)$$

In which, λ is a ratio coefficient, $\pm$ is derived from the absolute notation in equation (7-10).

（3）Yield condition

Mohr-Column criterion is employed as the sliding yield condition here,

$$F(\sigma) = \mid \tau_s \mid + \sigma_n \tan\phi - C = 0 \quad (7\text{-}12)$$

In which, σ_n and τ_s are respectively normal stress and shear stress, ϕ and C are respectively internal frictional angle and cohesion of fractures.

Suppose the tensile strength of fracture is zero, the tensile yield condition is set as

$$F(\sigma) = \sigma_n = 0 \quad (7\text{-}13)$$

（4）The consistent condition

Suppose at the time step *t.*, the stress state is $\left\{\sigma\right\}$, which is on yield surface

$F(\sigma)=0$; at the time step $t+dt$, incremental stress $\{\Delta\sigma\}$ pointing outwards from the yield surface is exerted and the stress state becomes $\{\sigma\}+\{\Delta\sigma\}$. Since stress state cannot be out of yield surface, $\{\sigma\}+\{\Delta\sigma\}$ must still satisfy the yield condition,

$$F\left(\sigma+\Delta\sigma\right)=0 \tag{7-14}$$

Using Taylor series to expand the above equation and omitting higher order terms, we obtain the following consistent condition

$$\left\{\frac{\partial F}{\partial\sigma}\right\}^{T}\{\Delta\sigma\}=0 \tag{7-15}$$

The yield condition for tensile failure is expressed in the equation (7-13). When tensile failure occurs, the stress is completely relaxed and energy is fully released[12]. The yield condition for sliding failure is expressed in the equation (7-12). When sliding occurs, according to the increment method in the framework of classical elastic-plastic theory[26], the plastic matrix $[D]_p$ can be solved by the following equation,

$$[D]_p=\frac{[D]\left\{\frac{\partial Q}{\partial\sigma}\right\}\left\{\frac{\partial F}{\partial\sigma}\right\}^{T}[D]}{\left\{\frac{\partial F}{\partial\sigma}\right\}^{T}[D]\left\{\frac{\partial Q}{\partial\sigma}\right\}} \tag{7-16}$$

With the non-associated flow rule, i.e. the equation (11), there stands,

$$\left\{\frac{\partial Q}{\partial\sigma}\right\}=\{\tan\psi\ \pm 1\}^{T}$$

then，

$$[D]_p=\frac{1}{k_n\tan\varphi\cdot\tan\psi+k_s}\begin{bmatrix}k_n^2\tan\varphi\cdot\tan\psi & \pm k_nk_stg\psi\\ \pm k_nk_stg\varphi & k_s^2\end{bmatrix} \tag{7-17}$$

During the iteration process, stress state of the next step is unknown a prior. Since k_n is a nonlinear coefficient and is correlated with the stress state, when sliding failure occurs, $[D]_p$ cannot be easily determined by the equation (7-17). In thought of the relationship between stress and elastic deformation, the consistent condition (7-15) can be transferred to

$$\left\{\frac{\partial F}{\partial u^e}\right\}^{T}\left\{\Delta\mathrm{u}^e\right\}=0 \tag{7-18}$$

So, when solving the increment elastic-plastic deformation during iteration process, analysis can be conducted in the space of elastic deformation. Substituting the equation (7-9) into (7-12), the yield function in terms of the elastic deformation can be expressed as,

$$F(u^e)=|k_su_s^e|+\int_0^{u_n^e}k_n du\tan\phi-C=0 \tag{7-19}$$

The red lines illustrated in figure 7.3 are the yield surface in the space of elastic deformation. Probable stress state must be within this surface. Suppose at time step t, accumulated elastic deformation of the Gauss point G is located at A. At time step $t+dt$, through elastic trial calculation, the accumulated elastic deformation is at point C, outside of the yield surface. According to the yield condition and the consistent condition, elastic deformation must be within the yield surface. Separating $\overrightarrow{AC}$ into two parts,

$$\overrightarrow{AC} = \overrightarrow{AB} + \overrightarrow{BC}$$

in which, $\overrightarrow{AC} = \left(\Delta u_n, \Delta u_s\right)$ is the total increment deformation, $\overrightarrow{AB} = \left\{\Delta u_n{}^e \quad \Delta u_s{}^e\right\}^T$ is the elastic increment deformation, and $\overrightarrow{BC} = \left\{\Delta u_n{}^p \quad \Delta u_s{}^p\right\}^T$ is the plastic increment deformation.

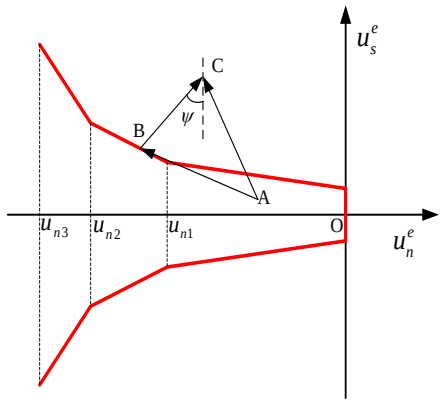

Figure 7.3 Yield surface in the space of elastic deformation

Concerning the consistent condition, i.e. equation (7-18), the accumulated elastic deformation must be positioned on the yield surface, such that the point B must be located on the red line shown in Figure 7.3. According to the dilation condition, i.e. the non-associated flow rule（11），the point B can be located in the following way: as shown in fig 7.3, from point C, draw a line with an angle of ψ with respect to the axis y, which intersects the yield surface at the point B. The coordinate of the point B is the accumulated elastic deformation.

7.3 Flow simulation: discrete fracture network model

The discrete fracture network model is used for flow simulation. This model is based on three assumptions: (1) water is incompressible; (2) the rock matrix is impermeable; (3) flow obeys the cubic law.

Flow rate in single fracture is expressed as，

$$q_{ij} = \frac{gb^3}{12\upsilon}\frac{h_i - h_j}{l_{ij}} \quad (7\text{-}20)$$

in which, ν is the kinematic viscosity of water, b is the fracture aperture, h_i and h_j are respectively water heads for the two ends of this fracture segment, and l_{ij} is the length. Assembling all conservative equations at intersections, one can obtain the global equilibrium equations for flow simulation.

Fracture aperture under stress is calculated by the following expression,

$$b = b_0 + \Delta u_n \quad (7\text{-}21)$$

in which, b_0 is the initial aperture, Δu_n is the normal deformation induced by stress.

It needs to be noted here that after deformation, apertures of the two ends of a fracture may not be equal to each other. In this case, the cubic law is not appropriate any more since the two fracture planes are not parallel to each other. Confronted with this problem, Jing[3] carried out an equivalent hydraulic aperture b_e based on Iwai's work[22,23],

$$b_e = b_m\left[16\frac{r^2}{(1+r)^4}\right]^{\frac{1}{3}} \quad (7\text{-}22)$$

in which, $r = b_1 / b_2$, $b_m = (b_1 + b_2)/2$, b_1 and b_2 are respectively the apertures of the two ends.

7.4 Solute transport in fracture network

7.4.1 Particle tracking method

When a particle carried by water arrives at a node which is intersected by two or more fractures, it may exit through any fracture that with outward flow velocity. Suppose that solutes from different inward fractures completely mix in the intersection, the probability that a particle exits through the outward fracture with a flow rate of Q_1 equals the ratio between Q_1 and the total outward flow rate.

$$p(Q_1) = \frac{Q_1}{\sum_{i=1}^{N_{exit}} Q_i} \quad (7\text{-}23)$$

Where, N_{exit} denotes the total number of fractures intersected in the node with an outward flow direction.

At each node, a particle chooses an outward fracture according to its flow rate. It is a random process. It's probable that particles entering in the same inlet node will end up in

different exit points or at least through different flow paths. This way, we can trace up every fracture a particle pass through from entering the fracture network to exiting. These fractures consists a flow path. The residence time of water in flow path p t_w^j is denoted by the sum of water residence time in every fracture

$$t_w^p = \sum_i^{N_p} t_{w,i} = \sum_i^{N_p} \frac{V_i}{Q_i} \qquad (7\text{-}24)$$

Where, $t_{w,i}$ is the water residence time of the ith fracture, N_p is the total number of fractures on path p, V_i is the volume of the ith fracture, Q_i is the flow rate of the ith fracture.

7.4.2 Residence time distribution of solutes considering matrix diffusion

Considering that a particle can interact with fracture surfaces and can be withdrawn from water under some mechanism (like surface sorption, and matrix diffusion), the more area water touch with fracture surfaces, the more probable that particles will exit from the water into the matrix. So it is intuitively supposed that the value of the touching area between water and fracture surfaces divided by the flow rate of the fracture is a vital factor reflecting the interaction effects, denoted by A_q / Q. As for the path p, the sum value of A_q / Q along the path can be denoted by,

$$(A_q / Q)^p = \sum_i^{N_p} \frac{A_i}{Q_i} \qquad (7\text{-}25)$$

When the penetration depth into rock matrix is smaller than the distance between fractures and the diffusion and dispersion along the flow path is negligible, the residence time distribution can be described by a simple equation, which indicates the relation between the effluent concentration c and the time when the inlet boundary is suddenly exposed to a solution with a concentration c_0. Neglecting sorption of the fracture surface, but considering matrix diffusion, the relationship between the effluent concentration c and the time t for path p can be described as[10],

$$\frac{c}{c_0} = Erfc\left(\frac{1}{2} (\frac{A_q}{Q})^p \frac{MPG}{(t - t_w^p)^{1/2}} \right) \qquad (7\text{-}26)$$

Where, $Erfc(x)$ takes the form $Erfc(x) = \frac{2}{\sqrt{\pi}} \int_x^{\infty} e^{-t^2} dt$, $(\frac{A_q}{Q})^p$ can be obtained by equation (7-25), t_w^p denotes the water residence time of path p; MPG is short for material properties group, and is described by pore diffusivity D ,sorption coefficient K and matrix porosity ε as

$$MPG = \varepsilon\sqrt{D(1+\frac{(1-\varepsilon)K}{\varepsilon}} \quad (7\text{-}27)$$

If only advection is taken into account, the residence time of a particle in any path equals the water residence time of which. If matrix diffusion is also considered, the residence time of a particle in path *p* can be calculated through the procedure given below, which is derived from equation (7-26)

(1) Generate a random number $[R]_0^1$ which obeys uniform distribution within [0,1],

$$[R]_0^1 = Erfc\left(\frac{1}{2}\left(\frac{A_q}{Q}\right)^p \frac{MPG}{\left(t^p - t_w^p\right)^{1/2}}\right) \quad (7\text{-}28)$$

(2) Solve equation (7-28), residence time t^p in path *p* can be obtained

$$t^p = t_w^p + \left(\frac{MPG}{2Erfc^{-1}([R]_0^1)}\left(\frac{A_q}{Q}\right)^p\right)^2 \quad (7\text{-}29)$$

7.4.3 Numerical simulation of nuclide transport

After the steady flow field is obtained, solute transport simulation can be conducted. The procedure of transport simulation in discrete fracture network is listed below.

Step 1 Calculate the total water head of every node in the discrete fracture network.

Step 2 Calculate the flow rate Q_i, water residence time $t_{w,i}$ and $(A_q/Q)_i$ of every single fracture.

Step 3 Particle tracking. Select a large number of particles, like 100000 or more. Track the path of every particle using equation (7-23) from the inlet boundary to the outlet boundary and calculate the accumulated water residence time t_w^p and accumulated $(A_q/Q)_i$ of every path using equation (7-24) and equation (7-25).

Step 4 Calculate the residence time of every particle. If matrix diffusion is not accounted for, the residence time of a particle equals the water residence time of the path it passed through. If matrix diffusion is considered, the residence time of a particle is calculated by equation (7-29).

Because of the monotony of the function of $Erfc(x)$, The bisection method is adopted here to solve equation (7-28). With great flexibility of adding more Gauss points when specific accuracy are required, the Gauss-Chebyshev integration method is used to calculate the integral of $Erfc(x)$. Through comparison, it is found that our numerical method can solve this equation with almost the same precision as the

commercial software Maple and Matlab.

7.5 Numerical Procedure for coupling process

Hydro-mechanical coupling is realized by a cross iteration procedure. After blocks and the connected fracture network are found, the flow simulation is firstly conducted, water pressure distribution obtained from which is then used as force boundary for stress and deformation simulation. New hydraulic apertures got from mechanical analysis are used for new flow simulation. This iteration procedure ends till convergence conditions for both deformation and flow are satisfied. The flowchart of this procedure is illustrated in Figure 7.4.

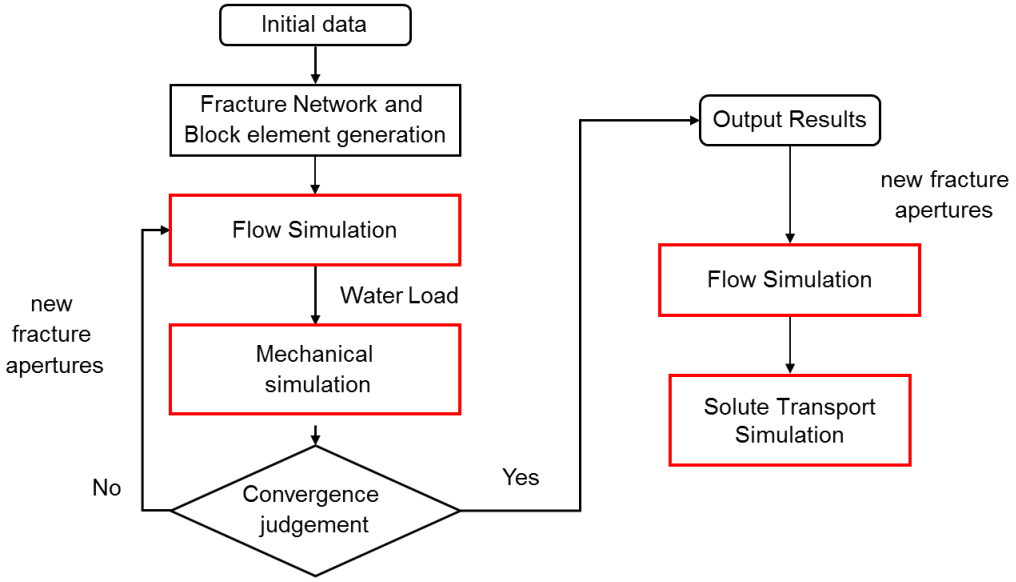

Figure 7.4 Flow chart of simulation of hydro-mechanical-transport coupling process

7.6 Case study

DECOVALEX[18] is an international cooperative research project on nuclear waste disposal, the main aims of which are theoretical and experimental studies of coupled thermal, hydrological and mechanical processes in hard rocks and their effects on nuclide transport. The Task C, DECOVALEX-2011 contains a 2D BMT model, which comprises of 7797 fractures in a square region with side length of 20 meters, as is shown in Figure 7.5(a). The geometric parameters for generating fracture network realizations are based on the field mapping results of a site characterization at the Sell afield area, Cambria, England [25]. To reduce computational efforts and without losing generality, a network of $5\text{m}\times5\text{m}$ is cut from the center of the original model, in which 2659 intersections and 2044 irregular blocks are contained, as is shown in Figure 7.5(b). Effects of stress on solute

transport in this fracture network have also been studied by Zhao[7].

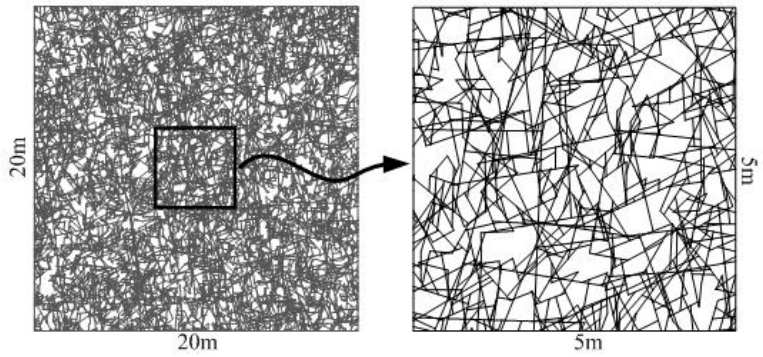

(a) (b)

Figure 7.5 Fracture network for study of hydro mechanical transport process in rock masses

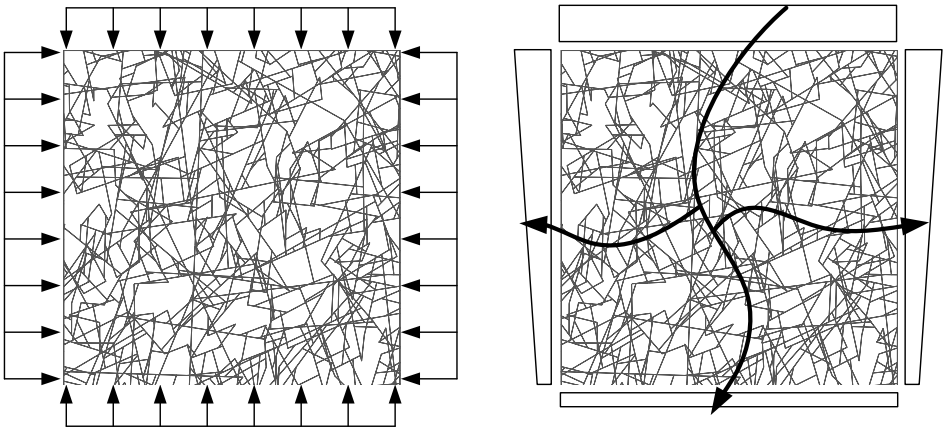

(a) Stress boundary (b) Hydraulic Boundary

Figure 7.6 Hydraulic boundary and mechanical boundary

Stress boundary and hydraulic boundary are illustrated in Figure 7.6(a) and Figure 7.6(b). For convenience when quoting the stress boundary, a ratio is defined as $K =$ horizontal boundary stress: vertical boundary stress. To study effects of different stress boundaries on flow field and solute transport, eight values of are employed, i.e. 0:0, 5:5, 5:10, 10:5, 5:15, 15:5, 5:20 and 20:5, the unit of which is MPa. The hydraulic gradient is set as 1m/m. Mechanical parameters of fractures are listed in Table 7.1, and all initial hydraulic apertures are set as 30 μm.

Flow rate distributions under different stress boundaries (i.e. different values of *K*) are illustrated in Figure 7.7. The value of flow rate is represented by the thickness and color of the line. Flow rate in a fracture increases as the corresponding line becomes thicker and the color of which turns from yellow to blue, orange and red. For fractures with very small flow rate, their existence is not shown. So many voids can be seen in some cases, such as *K*=15：5. For *K*=5:5, *K*=10:5 and *K*=5:10, as can be observed from Figure 7.7, flow rate

generally decreases as stress increases. When the difference between horizontal stress and vertical stress becomes larger, such as *K*=15：5, *K*=5：15, *K*=5：20 and *K*=20：5, as stress increases, larger flow rate is observed in fractures which are nearly parallel to direction of the principal stress. Compared to the case of *K*=0：0, these cases show obvious anisotropy in flow field.

The reason for this phenomenon is stated as follows. When the difference between horizontal stress and vertical stress is not enough to cause dilation, it is the normal deformation behavior that controls the conductivity of fractures. In such cases, as stress increases, the hydraulic aperture decreases, so does the conductivity. However, when the difference between horizontal stress and vertical stress is large enough to cause dilation, sliding usually firstly occurs in some large fractures with an orientation nearly parallel to the principal stress, the dilation effects along with which results in significant rise in hydraulic aperture. That is why some large flow rate is observed in the cases of K=5:15, K=5:20 and K=20:5. In such cases, dilation effects become the dominant mechanism of permeability evolution of the global fracture network system.

Table 7.1 Mechanical parameters for fractures

Parameters		value
Normal constitutive parameters	$u_{n1}(\mu m)$..	15
	$\sigma_{n1}(MPa)$	4
	$u_{n2}(\mu m)$	20
	$\sigma_{n2}(MPa)$	10
	$u_{n3}(\mu m)$	25
	$\sigma_{n3}(MPa)$	30
Shear stiffness, $k_s(GPa/m)$		434
Internal frictional angle, $\phi(^\circ)$		24.9
Dilation angle, $\psi(^\circ)$		5
Cohesion, $c(MPa)$		0
Initial aperture, $a_0(\mu m)$		30
Minimum aperture, $a_{res}(\mu m)$		5
Maximum aperture, $a_{\max}(\mu m)$		50

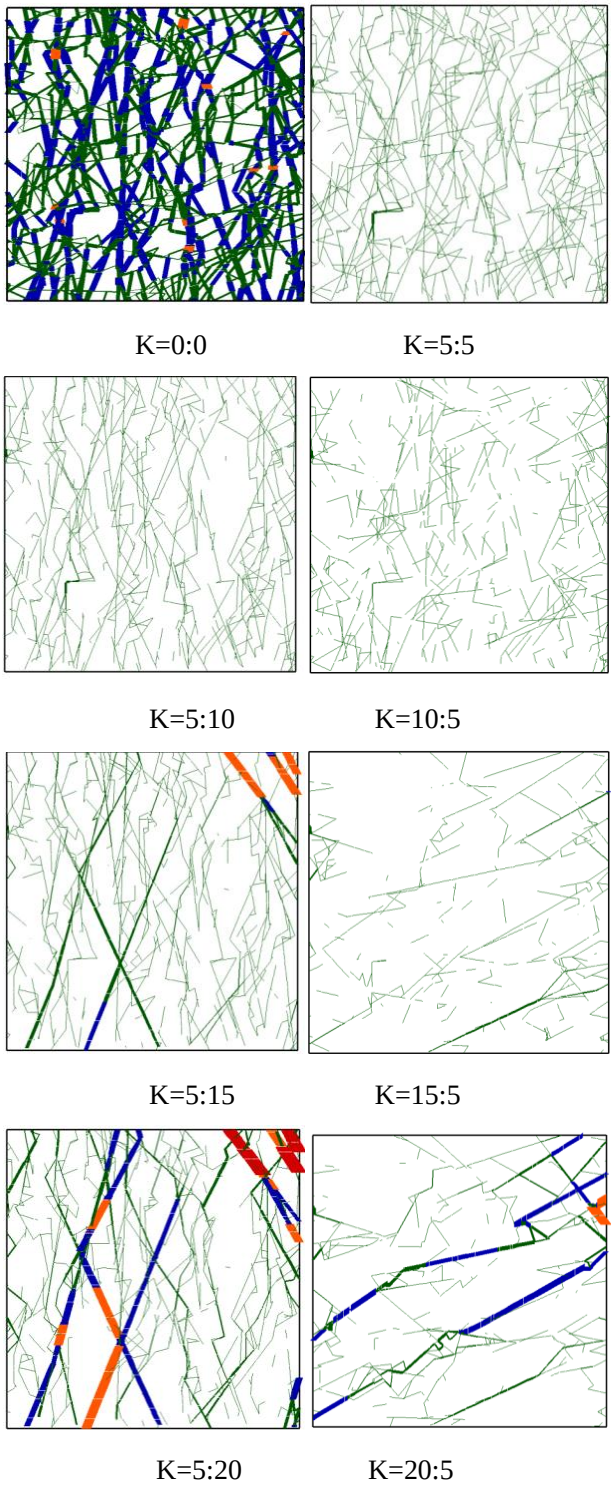

Figure 7.7 Flow rate distribution under different stress conditions

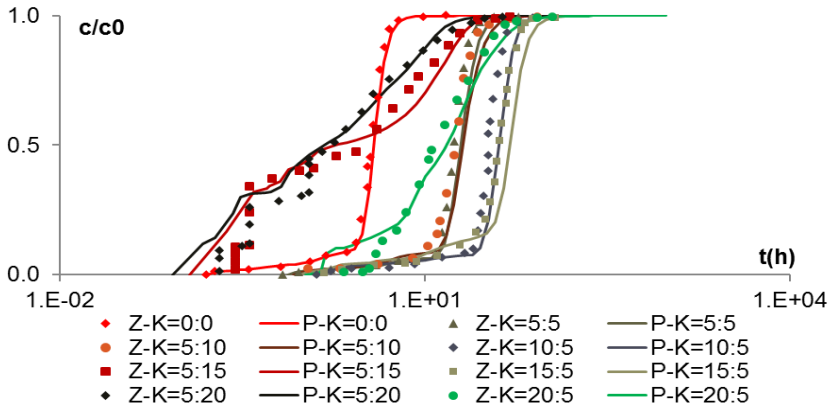

Figure 7.8 Breakthrough curves under different stress ratio with only advection considered

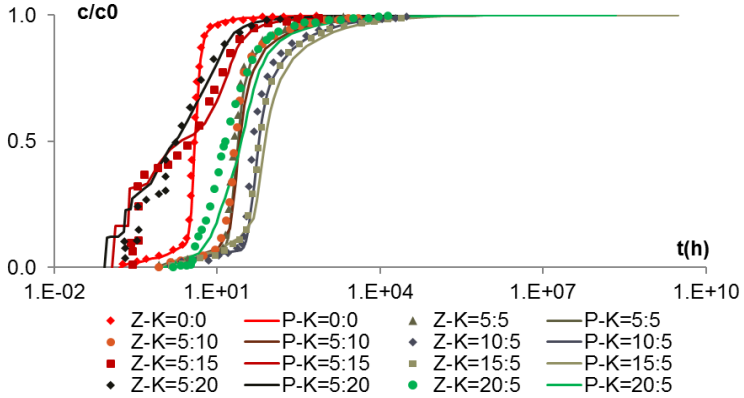

Figure 7.9 Breakthrough curves under different stress ratio considering matrix diffusion

Shown in Figure 7.8 are breakthrough curves of solutes under different stress conditions with only advection considered. In this figure, *Z* represents Zhao's results[7], *P* represents results of the present study. For cases of *K*=5:5, *K*=10:5, *K*=5:10 and *K*=15:5, as stress increases, the breakthrough curve turns to the right side gradually; but for cases of *K*=20:5, *K*=5:15 and *K*=5:20, the move of the breakthrough curve shows an inverse trend, it turns to the left side as stress increases.

Since solute transport is controlled by the flow field, difference between breakthrough curves under different stress conditions can be explained as follows. From Figure 7.7, it can be seen that for cases of *K*=5:5 and *K*=10:5, as stress increases, flow rate in fractures drops drastically and the breakthrough curve shows an obvious trends towards the right side; for the case of *K*=5:10, compared to *K*=5:5, though the vertical stress has increased, no obvious rise in flow rate can be observed, making the breakthrough curve almost coincide with which of *K*=5:5; for the case of *K*=15:5, compared to *K*=10:5, though larger flow rate is shown in some fractures due to dilation, flow rate in the vertical direction generally decreases, making the breakthrough curve turn right but with a little margin; for cases of

K=20:5 , *K*=5:15 and *K*=5:20, dilation effects become the dominant mechanism controlling the permeability evolution, and significant increase in flow rate is observed in some large fractures with orientation almost parallel to the principal stress, making the breakthrough curve turn to the right side in a large margin. It can be observed in the figure that results of the present study agree well Zhao's results, indicating the validity of our model from the side. Shown in Figure 7.9 are breakthrough curves considering both advection and matrix diffusion. Apart from a greater magnitude in the residual time, the basic trends of these curves are in line with which illustrated in figure 7.8. The reason for this phenomenon is similar to what mentioned above, thus not repeated here. It needs to be noted here that coupling effects are considered in the present study through a cross iteration procedure, but in Zhao's work, flow field's effects on deformation was not taken into account. Therefore, results of the present study are more reasonable in theory.

For solute transport simulation, the total number of solutes is chosen as 10000. Illustrated in figure 7.10~7.12 are respectively solute distribution for different cases of K=0:0, K=20:5 and K=5:20 at different time with only advection considered. Compared to K=20：5 (Figure 7.11) and K=5:20 (Figure 7.12), solutes are distributed more evenly for the case of K=0:0. For the case of K=20:5, solute seems to prefer to move in fractures with horizontal orientation. For the case of K=5:20, two large vertical fractures constitute the main channels for solute movement. This phenomenon can also be explained by Figure 7.7. For cases of K=5:20 and K=20:5, hydraulic apertures of a few vertical long fractures and horizontal long fractures increase drastically due to dilation. These fractures form the main channels for water flow, which are preferred when solute chooses its successive path (equation (25)). The existence of this kind of preferential channel increase the time span of migration time, making the breakthrough curve of K=5:20 and K=20:5 have greater slope than which of K=0:0 (Figure 7.8).

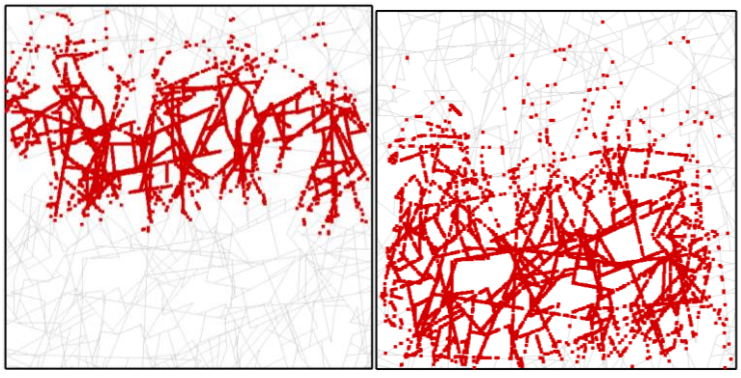

（a）t=5000s　　（b）t=10000s

Figure 7.10　particles distribution at different time with K=0:0

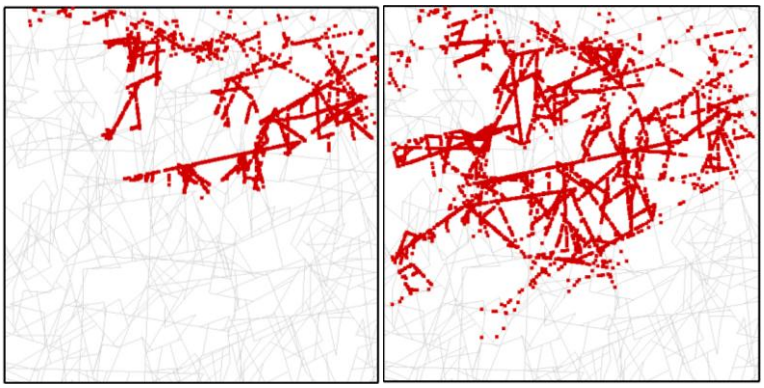

（a）t=25000s （b）t=50000s

Figure 7.11 particles distribution at different time with K=20:5

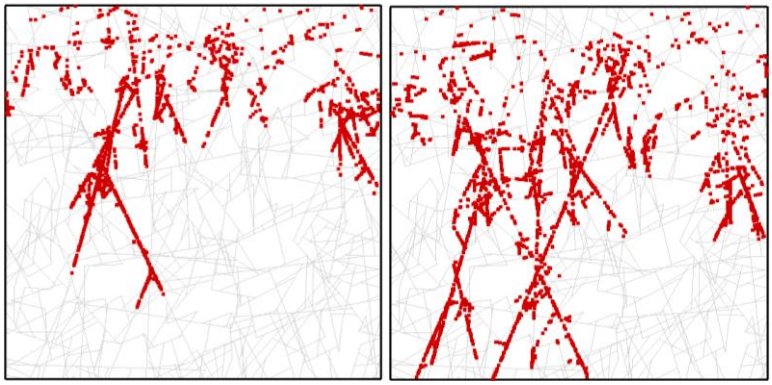

（a）t=5000s （b）t=10000s

Figure 7.12 particles distribution at different time with K=5:20

7.7 Discussion

7.7.1 The necessity to consider hydro-mechanical coupling

The main focus of analysis above is on stress effects on flow and transport in fracture network. The hydraulic gradient is set constant, the upstream head and the downstream head are respectively 6*m* and 1*m*. Compared to the boundary stress, hydraulic pressure is relatively small and can be negligible. However, in some situation, such as hydropower reservoir, water head may exceed 100m and water pressure has the same magnitude as the stress state. In such cases, effects of water pressure on deformation cannot be neglected and hydro mechanical coupling must be considered.

The fracture network in figure 7.5(b) and the boundary condition in figure 7.6 are still used. The hydraulic gradient is set as 1m/m and the stress boundary is set as *K*=5:5. To consider water pressure effects, four different groups of values for the upstream and downstream water head are chosen, i.e. 6m/1m, 105m/100m, 205m/200m and 305m/300m.

Breakthrough curves for these four groups are illustrated in figure 7.13 and figure 7.14. Illustrated in figure 13 are breakthrough curves considering only advection, and in Figure 7.14 are breakthrough curves considering both advection and matrix diffusion. The breakthrough curve of the case 6m/1m almost coincides with which of the case without considering coupling effects. And as water head increases, breakthrough curves show a trend towards the left side, approaching which of the case with no stress boundary applied. This trend is consistent with the common sense: when the boundary stress is constant, the higher the water pressure is, the lower the effective stress in the fracture is. Lower effective stress results in relatively large aperture and large conductivity. This group of simulation indicates that when the boundary water head is large in amount, hydro-mechanical coupling plays a significant role in influencing solute transport, so the coupling effects must be considered.

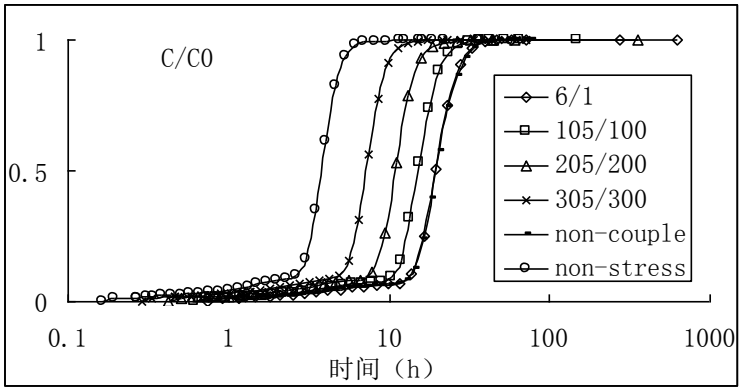

Figure 7.13 Breakthrough curves under different water heads with only advection considered

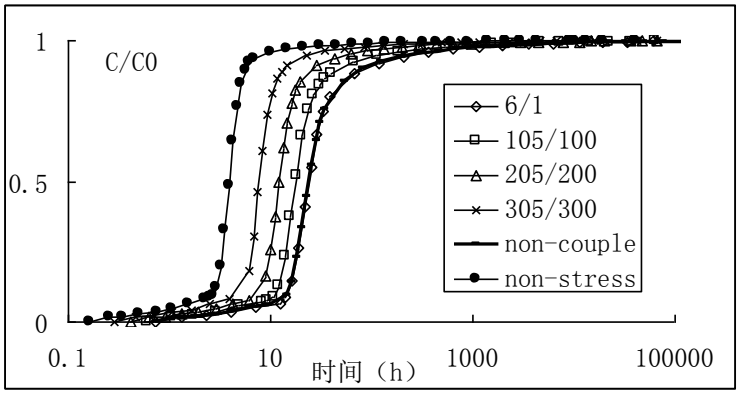

Figure 7.14 Breakthrough curves under different water heads considering matrix diffusion

7.7.2 Effects of hydraulic gradients

With the proposed model, this challenging example with complex fracture network shown in Figure 7.5(a) is used here to analyze the effects of different hydraulic gradients on

solute transport in highly fractured rocks. The hydraulic boundary of this example is shown in Figure 7.15. Water flows from the right to the left, with the top and bottom boundary impermeable. Three sets of hydraulic gradients are deployed here: (1) 1m/m; (2) 0.001m/m; (3) 0.0001m/m. Through many tests, 10000 is chosen as the total number of the particles, as more particles can only obtain similar results as 10000 particles. As the number of particles is very great, the ratio between the number of particles obtained in the outlet boundary N and the total number of particles N_0, denoted by N/N_0, is considered to equal the ratio of the effluent concentration c to the original concentration c_0, denoted by c/c_0.

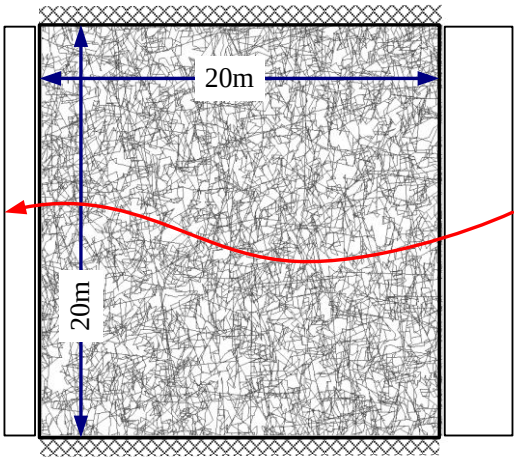

Figure 7.15 The discrete fracture network of Task C, DECOVALEX-2011 and the hydraulic boundary condition

Under the hydraulic gradient of 1m/m, the flow rate distribution is obtained, which is shown in Figure 7.16. We can see from this figure that flow rate is not uniformly distributed and most flow rate takes place in the well-connected fractures with long traces and wide apertures, which form the main channels. Shown in Figure 7.17 are the distributions of nuclides in fracture network at different time. Comparing Figure 7.17 with Figure 7.16, it is clear that most nuclides gather in fractures with greater flow rate. Due to the non-uniformity of fracture distribution and flow rate distribution, nuclides entering the network at the same time follow different pathways and exit from the network at different time. From Figure 7.17(c)~(e), it can be seen that the residence time of most nuclides is between 2000s and 10000s.

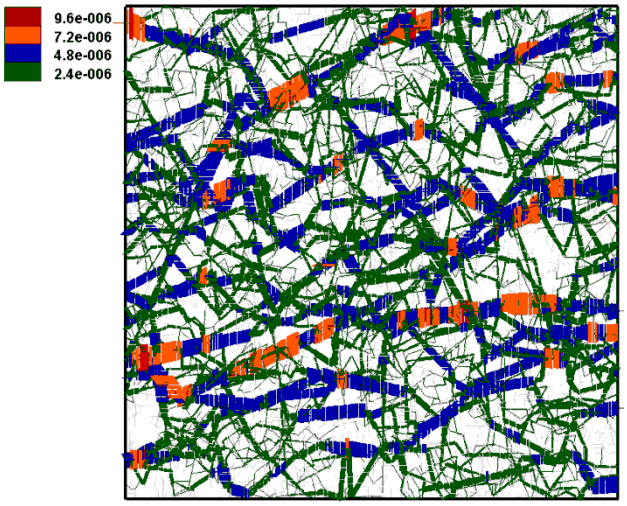

Figure 7.16 Flow rate distribution in fracture network under hydraulic gradient of 1m/m

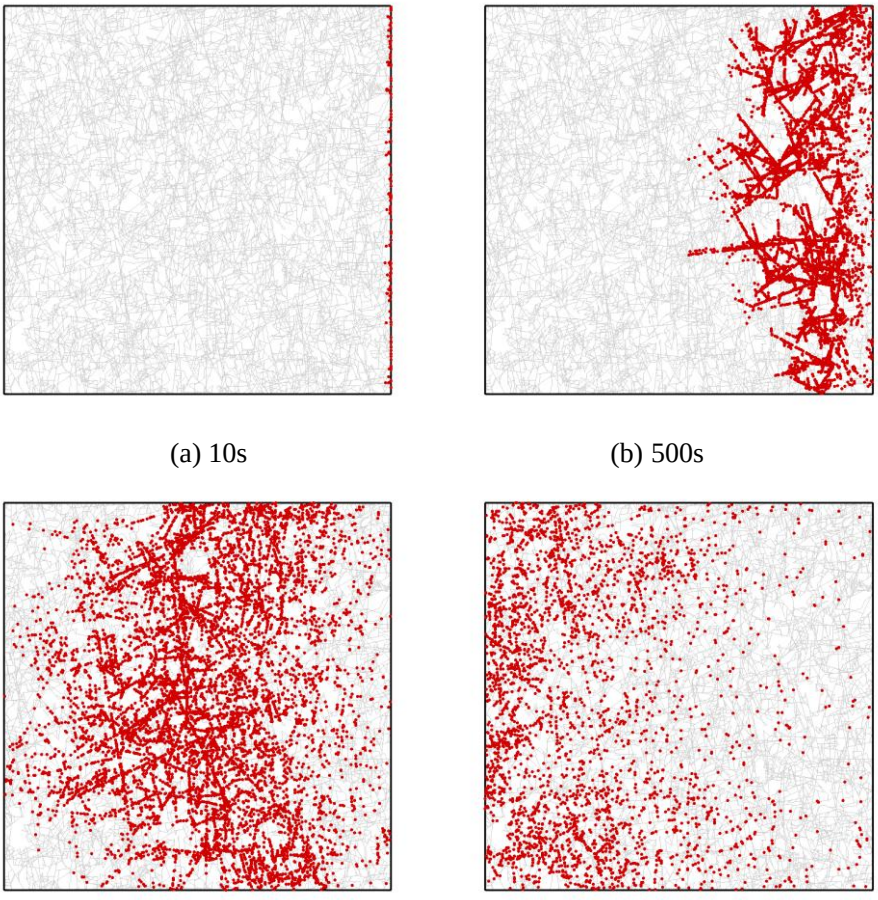

(a) 10s (b) 500s

(c) 2000s (d) 5000s

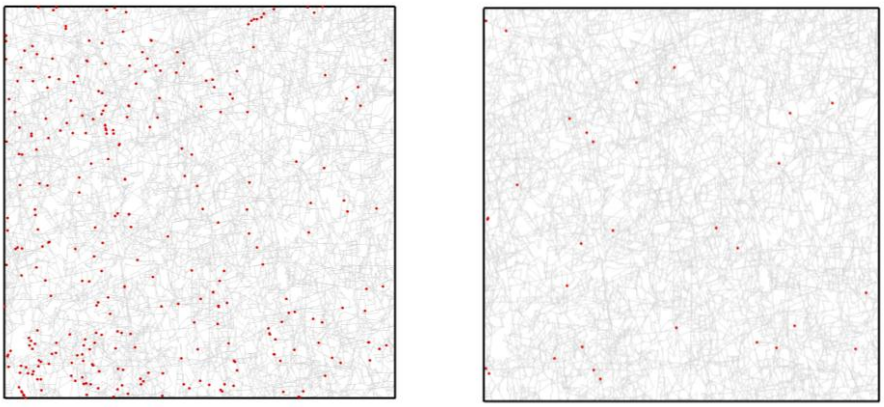

(e) 10000s (f) 20000s

Figure 7.17 Distribution of nuclides in fracture network at different time

The breakthrough curves are shown in Figure 7.18, in which, the horizontal axis represents time while the vertical axis represents the ratio of the effluent concentration c to the original concentration c_0. It is obvious that, as the hydraulic gradient becomes lower, the breakthrough curves tends to move right, which means most particles tend to stay longer in the rocks under lower hydraulic gradients. Meanwhile, when the hydraulic gradient is high (1m/m), the breakthrough curves considering only advection and which considering also matrix diffusion almost overlap with each other. With the hydraulic gradient becoming lower to 0.001m/m and 0.0001m/m, the two curves considerably differ from each other, indicating that under lower hydraulic gradients, most particles tend to be retarded for a much longer time due to matrix diffusion.

The physical mechanism of this phenomenon can be interpreted as follows. Water residence time is inverse to the flow rate in the fracture (equation (7-24)), which is proportional to the hydraulic gradient (equation (7-20)). As a result, when the hydraulic gradient grows lower, the water residence time gets larger, showing as breakthrough curves moving right. If matrix diffusion is also considered, we can see from equation (7-29) that residence time of particles due to matrix diffusion is proportional to the square of $(A_q/Q)^p$. Considering that the flow rate is proportional to the hydraulic gradient (equation (7-20)), the residence time deduced by matrix diffusion is inverse to the square of the hydraulic gradient. So when the hydraulic gradient becomes lower, residence time of particles due to matrix diffusion becomes larger, and the breakthrough curves considering matrix diffusion show apparent difference from the breakthrough curve which only accounts for advection.

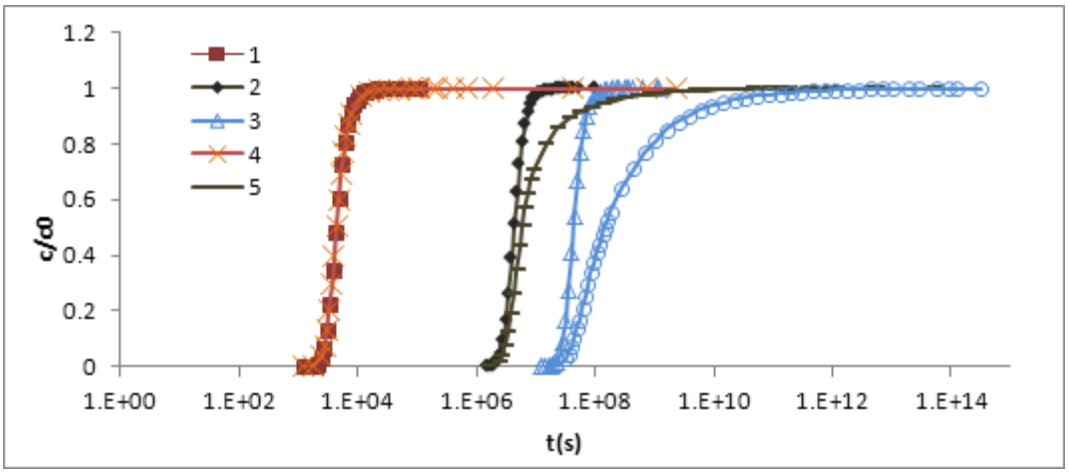

Figure 7.18 Breakthrough curves for nuclide transport under different hydraulic gradients. Specifically, curve 1, 2, 3 are for simulation taking only advection into consideration under the hydraulic gradient of 1m/m, 0.001m/m and 0.0001m/m, respectively, while curve 4, 5, 6 are for simulation accounting for both advection and matrix diffusion under the hydraulic gradient of 1m/m, 0.001m/m and 0.0001m/m, respectively.

7.8 Conclusion

Through combining rigid body spring method, discrete fracture network model and particle tracking method, a numerical model is established for simulation of hydro-mechanical coupling and solute transport in complex fracture network. The simplified Barton-Bandis model is employed as constitutive model of fractures, which effectively captures the non-linear normal stress deformation relationship and dilation effects. Under different stress conditions, a typical fracture network from Decovalex project is analyzed to study effects of stress on flow and transport. Results of the proposed model agree well with which of Zhao's work. Some conclusions can be drawn from the case study:

(1) When the stress ratio is not large enough to cause dilation, nonlinear normal stress deformation behavior is dominant in characterizing permeability and transport process. Conductivity of the whole system decreases as the stress increases.

(2) When the stress ratio is large enough to cause dilation, it is dilation that controls the stress induced permeability anisotropy and behavior change of transport. In the direction of principal stress, significant increase in hydraulic aperture takes place in some long fractures due to the dilation effects, constituting the preferential path for both flow and transport.

The necessity of considering hydro-mechanical coupling effects is discussed by a group of numerical tests. Analysis results show that water pressure has a great impact on

fracture deformation and permeability when they are comparable to the boundary stress. In such cases, hydro-mechanical coupling effects must be considered.

The hydraulic gradient has a significant influence on the residence time of solutes. Generally, the lower the hydraulic gradient is, the more time a solute would stay in the fracture network. And matrix diffusion plays a more important role in retarding the solutes when the hydraulic gradient is low. If a disposal site is chosen at a very dry zone, where the hydraulic gradient is expected to be very low, matrix diffusion will play a predominant role in nuclide transportation.

References

[1] Neretnieks. Diffusion in the rock matrix: an important factor in radionuclide retardation?[J]. J Geophys Res, 1980,85 (B8):4379–4397.

[2] Witherspoon PA. Introduction to second world wide review of geological problems in radioactive waste isolation, Geological Problems in Radioactive Waste Isolation[R]. 1996, LBNL-38915, UC-814: 1–4

[3] L. Jing, Y. Ma, and Z. Fang, Modeling of fluid flow and solid deformation for fractured rocks with discontinuous deformation analysis (DDA) method[J]. International Journal of Rock Mechanics and Mining Sciences, 2001, 38(3): 343-355.

[4] X Zhang, DJ Sanderson. Effects of stress on the 2-D permeability tensor of natural fracture networks[J]. Geophys J Int, 1996, 125: 912–924

[5] K.-B. Min, J. Rutqvist, C.-F. Tsang, et al. Stress-dependent permeability of fractured rock masses: a numerical study[J]. International Journal of Rock Mechanics and Mining Sciences, 2004, 41(7): 1191–1210.

[6] Baghbanan and L. Jing. Stress effects on permeability in a fractured rock mass with correlated fracture length and aperture[J]. International Journal of Rock Mechanics and Mining Sciences, 2008, 45(8):1320–1334.

[7] Z. Zhao, L. Jing, I. Neretnieks, and L. Moreno. Numerical modeling of stress effects on solute transport in fractured rocks[J]. Computers and Geotechnics, 2011, 38(2):113–126.

[8] Berkowitz B. Characterizing flow and transport in fractured geological media: a review[J]. Adv Water Resour, 2002, 25(8):3861–84.

[9] Neuman SP. Trends, prospects and challenges in quantifying flow and transport through fractured rocks[J]. Hydrogeol J, 2005, 13(1):124–47.

[10] Neretnieks I. Fast method for simulation of radionuclide chain migration in dual

porosity fracture rocks[J]. Journal of Contaminant Hydrology, 2006, 88: 269-288.

[11] Kawai. A new element in discrete analysis of plane strain problems[J]. Seisan Kenkyu, 1977，29（4）：204-207

[12] Zhuo JiaShou, Zhao Ning. Piecewise Rigid Body Interface Spring Method for Problems of Discontinuous Medium[J]. Journal of Hohai University, 1993, 21(5):34-43(in Chinese)

[13] Chen Shenghong. A general formulation of elastic-viscoplastic block theory of rock masses[J]. Journal of Hydraulic Engineering, 1996,1:78-84 (in Chinese)

[14] Qian Lingxi, Zhang Xiong. Rigid Body Finite Element Method in Structural Analysis[J]. Computational Structural Mechanics and Applications, 1991,8(1):1-14 (in Chinese)

[15] L. Moreno and I. Neretnieks. Fluid flow and solute transport in a network of channels[J]. Journal of Contaminant Hydrology, 1993,14(3–4): 163–192,.

[16] M. C. Cacas, E. Ledoux, G. de Marsily, et al. Modeling fracture flow with a stochastic discrete fracture network: Calibration and validation: 2. The transport model[J]. Water Resources Research, 1990, 26(3) : 491–500.

[17] R. YAMASHITA and H. KIMURA. Particle-tracking technique for nuclide decay chain transport in fractured porous media[J]. Journal of Nuclear Science and Technology, 1990, 27(11): 1041-1049.

[18] L. Jing, C.-F. Tsang, and O. Stephansson. DECOVALEX— An international co-operative research project on mathematical models of coupled THM processes for safety analysis of radioactive waste repositories[J].International Journal of Rock Mechanics and Mining Sciences & Geomechanics Abstracts, 1995, 32(5): 389-398.

[19] Baolin Wang, Vinod K. Garga. A numerical method for modelling large displacements of jointed rocks. I. Fundamentals[J]. Canadian Geotechnical Journal, 1993, 30(1): 96-108.

[20] Yao Chi, Jiang Qinghui, Ye Zuyang etc.Initial flow method for unconfined seepage problems of fracture networks[J]. Rock and Soil Mechanics, 2012,33(6):1896-1903.(in Chinese)

[21] Yao Chi，Jiang Qinghui，Chen Yifeng，Zhou Chuangbing. Numerical Simulation of Nuclide Transport in Complex Fracture Network[J]. Disaster Advances. 2012, 5(4):197-201

[22] Iwai K. Fluid flow in simulated fractures[J]. Am Inst Chem Eng J 1976, 2:259–263.

[23] Iwai K. Fundamental studies of fluid flow through a single fracture. [Ph.D. thesis][D].

USA: Univ. of California, Berkeley, 1976.

[24] T. Belytschko, M. Plesha, C. H Dowding, A computer method for stability analysis of caverns in jointed rock[J]. International journal for numerical and analytical methods in geomechanics, 1984, 8(5): 473-492.

[25] Nirex. Data summary sheets in support of gross geotechnical predictions[R]. Nirex report SA/97/052, Harwell, UK; 1997a.

[26] Zhu Bofang. The finite element theory and applications. Beijing: China Water & Power Press, 1998

Chapter 8 Conclusions and Further Developments

8.1 Conclusions

In this thesis, a unified numerical framework based on the improved rigid body spring method and discrete fracture network model is proposed to simulate the hydro-mechanical coupling in fractured rock masses. Two distinct situations are considered separately based on whether the deformation and fracturing of the rock matrix is taken into account.

For coarsely fractured or intact rock where behaviors of rock matrix cannot be neglected, the rock matrix is represented by a collection of convex polygons connecting with each other by cohesive interfaces. The improved rigid body spring method is used to model the response of the rock matrix under different loading path. A simple fracturing law combining Mohr-Coulomb criterion and tension strength is used for accounting for both Mode I (tensile) and Mode II (shear) fracturing events. The meso-scopic mechanical model is applied to simulate the behaviors of Vienne rock and Tournemire Shale and reasonable match between numerical results and experimental results is observed both quantitatively and qualitatively. A dual porosity model based on the discrete element model is established. Combining with the improved RBSM, this model is used to investigate the variation of permeability in rock failure. It is observed that the significant increase in conductivity occurs in the softening and residual phase, during which the global rock failure takes place and the percolation threshold is attained. The main failure surfaces constitute the main channels for water flow.

For densely fractured rock masses, the deformability and permeability of rock matrix is ignored. The rock mass is cut into an assemblage of rigid blocks by the presence of densely distributed fractures. Seepage flow mainly occurs in the connected fracture network. A variational inequality based initial method is proposed to study the unconfined seepage problem in 2D and 3D fracture networks. Several illustrative examples are analyzed to show the capability of the model in locating the free surface in complex fracture networks and its applicability for design and optimization of drainage systems in rock slopes. Through introduction of a relatively realistic constitutive model for fracture, the hydro-mechanical coupling process of the densely fractured rock mass is investigated by the improved RBSM and the DFN model. A particle tracking method is also incorporated to simulate the solute transport process. Stress effects on flow and solute transport is studied

and it is found that the controlling mechanism of flow and transport behaviors is varied from non-linear normal behavior to dilation effects with the increase of stress difference.

8.2 Further developments

The methods presented in this thesis, i.e. the improved RBSM and the DFN model can be grouped into the discrete element method. In light of their utilities demonstrated in this work, they are very promising numerical tools for charactering hydro-mechanical responses in rock engineering practice. Since they are relatively young methods, further developments are needed to improve the theoretical basis and numerical efficiency.

(1) The methods still need to be thoroughly tested before real engineering studies should be considered. Especially for the study of coupling between permeability and damage in Chapter 4, validation against experiments still remains to be a problem.

(2) The calibration between micro and macro failure parameters is still an open issue. Current calibration is much based on the trial and error procedure. More theoretically rigorous and efficient calibration procedure is needed.

(3) To solve real engineering problems, the models must be extended to three-dimensional algorithms. To solve large scale problems, high-performance computing techniques must be adopted. Specifically, the development of parallel algorithms will be considered in the future study.

Published Papers

[1] Chi Yao, Qinghui Jiang, etc. “Numerical Simulation of Nuclide Transport in Complex Fracture Network”. Disaster Advances, 2012,5(4):491-495 (SCI)

[2] C. Yao, Q, Jiang, W. Wei, C. Zhou. “The variational inequality formulation for unconfined seepage through three-dimensional dense fracture networks”, Sci, China Technol. Sci., 2013. (in press) (SCI)

[3] C. Yao, Q, Jiang, J. Shao, C. Zhou. “Numerical simulation of rock failure process using improved Rigid Body Spring Method”, Powders and Grains, 2013, Sydney, Australia. (in press) (SCI)

[4] Q. Jiang, C. Yao, Z. Ye, and C. Zhou. “Seepage flow with free surface in fracture networks”, Water Resources Research, vol 49, no 1, pp 176–186, 2013. (SCI)

[5] 姚池,姜清辉，叶祖洋，等. 裂隙网络无压渗流分析的初流量法[J]. 岩土力学, 2012,33(6): 1896-1903 (Yao C., Jiang, Q, Ye, Z, Zhou, C, “ Initial flow method for unconfined seepage problems of fracture networks”, Yantu Lixue/Rock and Soil Mechanics, v 33, n 6, p 1896-1903, 2012.) (in Chinese) (EI)

[6] 姚池，姜清辉，邵建富，周创兵. 一种模拟岩石破裂的细观数值计算模型[J]. 岩石力学与工程学报, 2013. (Yao C., Jiang Q., Shao JF., Zhou C.. A mesoscopic numerical model for simulation of rock fracturing. Chinese Journal of Rock Mechanics and Rock Engineering, 2013) (in press) (EI) (in Chinese)

[7] 姚池，姜清辉，位伟，周创兵. 复杂裂隙岩体水-力耦合模型及溶质运移模拟[J]. 岩石力学与工程学报, 2013. (Yao C., Jiang Q., Wei W., Zhou C.. Numerical Simulation Of Hydro-mechanical Coupling And Solute Transport In Complex Fractured Rock Masses. Chinese Journal of Rock Mechanics and Rock Engineering, 2013) (in press) (EI) (in Chinese)

[8] 姚池，张萍， 向广文. “二维岩体裂隙网络有压渗流数值模拟分析”，水电能源科学，2009，27(4): 50–53. (Yao C., Zhang P., Xiang G.. “Numerical Simulation Analysis for Under-pressured Seepage in 2-dimensional Fracture Network of Rock Mass”. Water Resources and Power, vol 27, no 4, pp 50–53, 2009) (in Chinese)

[9] Q. Jiang, Z. Ye, C. Yao, and C. Zhou. “A new variational inequality formulation for unconfined seepage flow through fracture networks”, Sci. China Technol. Sci., vol 55, no 11, pp 3090－3101, Nov 2012. (SCI)

[10] Q. Jiang, C. Zhou, W. Wei, and Y. Chi. “A Visualization Analysis System for

Three-Dimensional Stability Assessment of Landslides and Its Application", Advanced Science Letters, vol 4, no 8–10, pp 3082–3087, 2011. (SCI)

[11] B. Wang, Q. Jiang, C. Yao, and T. Xie. "Numerical analysis on failure mechanism of intermittent joints", in 2011 International Conference on Civil Engineering and Building Materials, CEBM 2011, July 29, 2011 - July 31, 2011, 2011, vol 255–260, pp 113–117. (EI)

[12] W. Wei, Q. Jiang, C. Yao, and T. Xie. "Reinforcement analysis of Wanjiakouzi arch dam using 3D nonlinear finite element method", in 2011 International Conference on Civil Engineering and Building Materials, CEBM 2011, July 29, 2011 - July 31, 2011, 2011, vol 255–260, pp 3472–3477. (EI)

[13] Q. H. Jiang, W. Wei, C. Yao, and C. B. Zhou. "Failure mode analysis of jointed rock masses around underground opening under excavation unloading", Materials Research Innovations, vol 15, pp S609–S612, Feb 2011. (SCI)